UCLouvain

École polytechnique de Louvain

Gait Parameters Influence on Flapping Flight Power Curves

Author: **Biagio PRINCIPE**
Supervisor: **Renaud RONSSE**
Readers: **Phillipe CHATELAIN, Gianmarco DUCCI, Gauthier LIMPENS**
Academic year 2019–2020
Master [120] in Electro-mechanical Engineering

Contents

Abstract

The purpose of this thesis is to investigate the possible correlations between the aerodynamic power and the flight kinematic of birds using their power curves. This study is conducted in conjunction with the UCLouvain RevealFlight project and adopts the White Ibis articulated lifting line developed within this research network. By coupling the articulated lifting line with a particle swarm optimizer and using a specific cost function, the thesis trims the kinematic of the bird and retrieves its power curve. The resulting optimized kinematic and the aerodynamic power are comparable with literature findings and suggest a predominance, during flight, of two distinct flight kinematic parameters (i.e. flapping amplitude and stroke-plane angle). Additional outcomes of this work strongly indicate a negligible dependency of the aerodynamic power from the flight kinematic of the bird. The limitations of the proposed coupled model are addressed and a potential extension of the articulated lifting line is proposed. Further studies are needed to establish the role of each of the flight kinematic parameters and to better understand their correlations with the total power consumption of birds.

Keywords: aerodynamics, avian flight, power curves, flight kinematic, optimization, White Ibis.

Nomenclature

Principal Variables and Constants

β	Bird body inclination
η	Phase angle
γ	Stroke-plane angle
ω	Angular speed
ϕ	Flapping amplitude
ψ	Wing sweeping motion
ρ	Air density
τ	Downstroke ratio
θ	Wing pitching motion
b	Bird wingspan
c	Wing chord length
C_{D_b}	Body drag coefficient
$C_{D_{pro}}$	Profile drag coefficient
COT	Bird cost of transport
D	Aerodynamic drag
D_{par}	Parasitic drag
D_{pro}	Profile drag
f	Flapping frequency
f_p	Feathering parameter
Fr_t	Bird trunk fineness ratio
g	Gravity constant
k	Correction/compensating factor
L	Aerodynamic lift
m	Bird mass
P	Bird aerodynamic power
P_{ind}	Induced power
P_{mc}	Minimum flight cost of transport
P_{mp}	Minimum flight power
P_{par}	Parasitic power
P_{pro}	Profile power
$R^{'}$	Size reduction factor
Re	Reynolds Number
S	Wing area
S_b	Body frontal area
S_d	Swept area/Actuator disk area
T	Bird thrust or Flapping cycle period($=\frac{1}{f}$)

v_i Induced speed

V_∞ Bird flight speed/Airflow speed/Horizontal speed

V_{mc} Minimum cost of transport flight speed

V_{mp} Minimum power flight speed

W Bird weight

Articulated Lifting Line (ALL)

α_{eff} Effective angle of attack

$\bar{F}_x$ Lateral force over a flapping cycle

$\bar{F}_y$ Lift over a flapping cycle

$\bar{F}_z$ Drag over a flapping cycle

Γ Bound circulation

$\vec{v}_{kin}$ Kinematic velocity

$\vec{w}$ Kinematic angular speed

i Spatial indexing

j Temporal indexing

m Number of temporal steps

n Number of spatial steps

Particle Swarm Optimization (PSO)

λ_{kin} Wing kinematic

$\vec{v}$ Particle speed

$\vec{x}$ Particle position

ζ Penalizing factor

$c1$ Local acceleration factor

$c2$ Global acceleration factor

J Cost function

k Number of particles

k_{cost} Minimum change in cost

k_{pos} Minimum change in position

$r1$ Local random vector

$r2$ Global random vector

t Number of iterations

$Trim$ Trim condition variable

w Inertia factor

Acknowledgements

Je souhaite remercier premièrement mon promoteur R. Ronsse, professeur à l'EPL à l'UCLouvain, pour m'avoir accepté en tant que mémorant et pour m'avoir suivi tout au long de cette expérience inoubliable et enrichissante. Il a su m'aiguiller lors d'impasses et sa sagesse m'a permis de grandir en tant que personne. De plus sa patience et sa nature calme ont eu un effet bénéfique sur mon humeur et ont agi en tant que remontant lors des moments plus difficiles. J'espère sincèrement pouvoir travailler encore avec vous en future. A presto e grazie di tutto[1].

Successivamente, mi sento in dovere di ringraziare Gianmarco Ducci, PhD student a UCLouvain e membro del progetto RevealFlight, per la sua assistenza tempestiva e continua. Grazie al tuo supporto non mi sono mai dato per vinto. I tuoi consigli sono stati fondamentali per comprendere al meglio gli argomenti trattati e per porre dei limiti a questa ricerca. La tua presenza è stata primordiale per la stesura di questa tesi e la tua simpatia e vicinanza linguistica/culturale mi hanno permesso d'affrontare il tutto con più leggerezza. Grazie infinite.

Ensuite, je voudrais exprimer ma gratitude envers deux membres du project RevealFlight: Gennaro Vitucci et Victor Colognesi. Ils ont tous les deux pris le temps de me suggérer des clefs de lecture pour surmonter certains problèmes rencontrés lors de cette étude. De plus une partie de leurs conseils a été fondamentale pour la finalisation de ce mémoire. Vi ringrazio tantissimo per il supporto.

Infine, vorrei ringraziare la mia famiglia e i miei amici per avermi supportato moralmente durante tutto questo periodo. L'amore che mi avete dato è incommensurabile, senza la vostra presenza non sarei mai riuscito a completare questo percorso. Ringrazio mio padre per la rilettura del testo e per le minute correzioni apportate. Ringrazio mia madre per la sua solarità e per la sua grande pazienza. Entrambi hanno contribuito al mio benessere e per questo ne sono immensamente grato.

In conclusion, it seems fair to say that this thesis has allowed me to mature and to develop a critical aspect of my persona that I did not master before. Furthermore, the topics addressed in this work have opened up new perspectives in my way of thinking and I can affirm that I am currently passionate about this field of research.

[1] A bientot et merci pour tout

«Con le ali e con la coda l'uccello fa nell'aria la stessa cosa che fa nell'acqua il nuotatore con le braccia e con le gambe»

Codice sul volo e sugli uccelli, Leonardo Da Vinci, 1505.

1 Introduction

Birds have always been a centre of interest for mankind. Flying was already a dream for Leonardo da Vinci **(1)**, Sir George Cayley **(2)**, Orville and Wilbur Wright **(3)** and many others.
We see flying animals every day and flying seems normal and obvious to us. Birds flight is far to be simple, each motions from take-off to landing is a sum of complex manoeuvres. The common pigeons that invade our cities are in reality a masterpiece of nature.

The goal of this thesis is to provide a paramount view of the principles of birds flight. My work, in particular, will analyse the bird kinematic parameters (i.e. gait parameters) that affect the flight performance of birds.

My research is part of the UCLouvain project **Reveal Flight (4)**, which aims is *"to provide an improved comprehensive understanding of bird flocks flight by capturing the interplay between the physics, the bio-engineering disciplines, and the problematic of control and self-organization"*.

My thesis analyses the performances of one agent (i.e. a single bird) through the study of its power curve (i.e. U-shape curve). The agent selected is the reference bird of the RevealFlight project i.e. the White Ibis, which is a migratory bird that flies in flock (i.e. V formation).

Power curves are usually used in the aircraft domain **(5)** to capture the power consumption of an aircraft at different flight speed.
These curves are obtained by supposing steady flight conditions (trimmed flight), meaning that the aircraft aerodynamic forces (lift, thrust, drag and weight) all cancel out and the aircraft is left to fly at a constant speed.

Figure 1.1 shows this condition ($Lift = Weight$ and $Drag = Thrust$) for a White Ibis.

We are particularly interested in the following two specific points of the power curve (Figure 1.2):

- (P_{mp},V_{mp}): minimum power and minimum power speed/maximum endurance speed
- (P_{mc},V_{mc}): minimum cost of transport ($COT = \frac{P}{mgV_\infty}$) power/speed or maximal range power/speed

These two points are interesting in the context of the thesis because birds seem to select them during flight. For instance, the minimal speed is selected for short to medium flights whereas maximal range speed is rather selected for long distance/migration flights **(6)**.

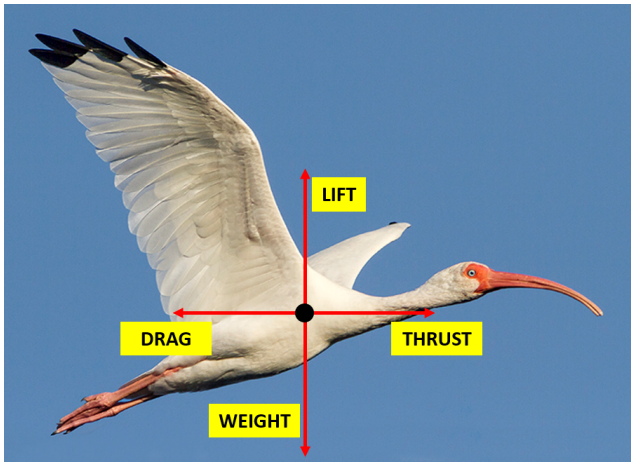

Figure 1.1: Trim conditions for a White Ibis

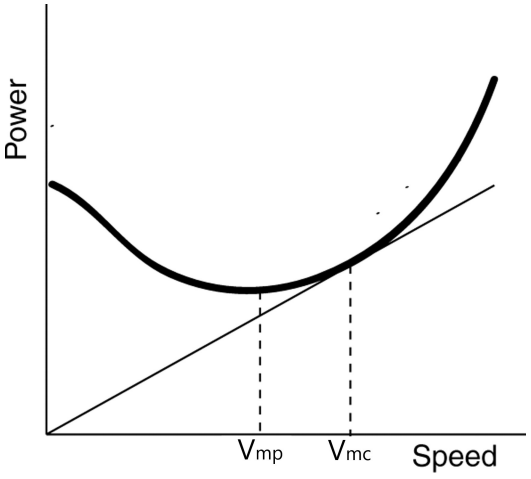

Figure 1.2: Power Curve/Points of interest **(7)**

Following the research of the RevealFlight team, this thesis will be focused particularly on fast forward flight birds, typically migratory birds. Transient manoeuvres such as taking off and landing or transient between two different flight regimes will not be addressed in this work.

The research begins by introducing the supporting background theory followed by a breakdown of the power curves literature. After reaching the current state of art, the nature of flapping flight is explained and the articulated lifting line (ALL) of the RevealFlight team is presented.

Next, I describe my contribution and the coupling with the ALL model. Finally, the results of both literature and ALL power curves are presented and commented.

The overall results of this thesis are then summarised and a possible extension of the articulated lifting line is suggested in the final chapter.

Before proceeding, for better clarity and to facilitate the reader, the most relevant bird kinematic parameters, used throughout this thesis, are listed hereafter:

1. ($\boldsymbol{\phi}$) Wing flapping amplitude: defined as the half stroke.

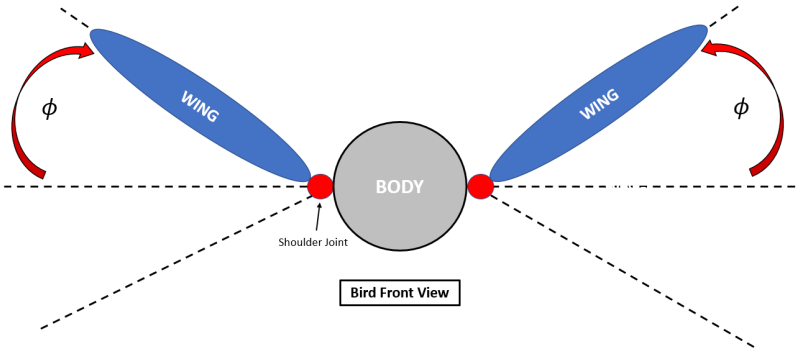

Figure 1.3: Flapping amplitude visualization

2. ($\boldsymbol{\theta}$) Wing pitching: defined as the airfoil rotation along its control point.

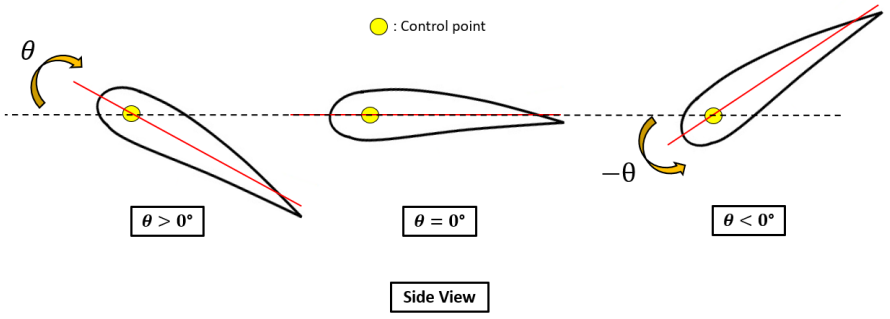

Figure 1.4: Wing pitching visualization

3. ($\boldsymbol{\gamma}$) Wing stroke-plane angle: an imaginary angle defined by the wing motion path, in this work the angle is equal to 0° when parallel to the incoming flow V_∞.

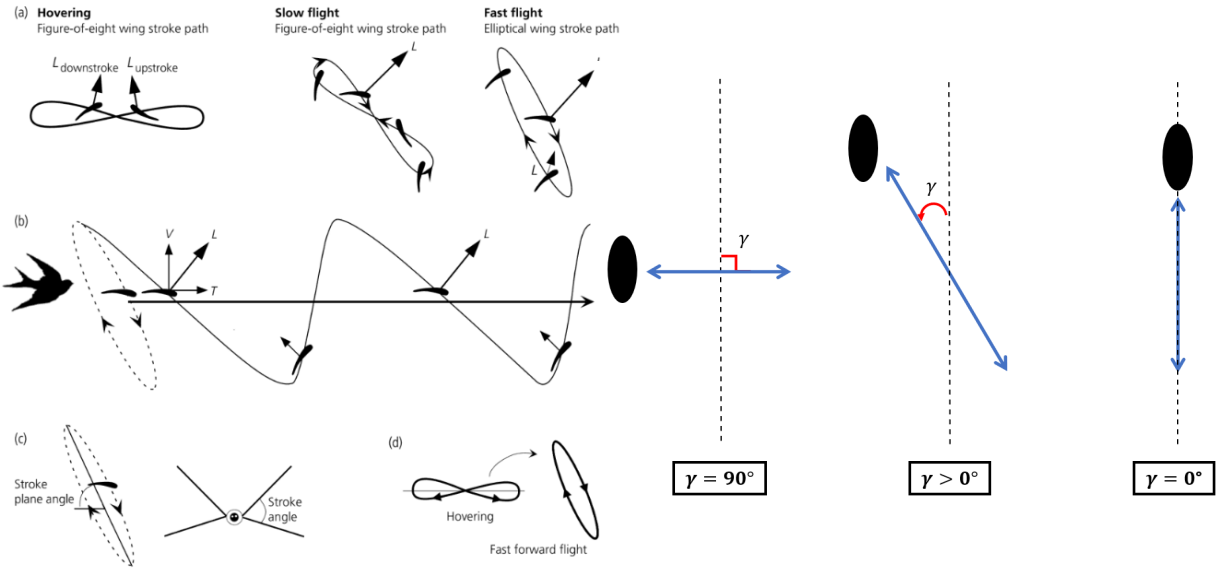

Figure 1.5: Stroke-plane angle visualization **(8)**

1.1 Scope and Limitations

The present work studies straight level flapping flight. Hovering and very slow flight are the limitation of this work. The agent is always considered to fly at a constant speed. The flight kinematic parameters are not constrained by physical limitations (i.e. bones maximal torque). The wings are considered weightless and the bird tailless. Inertial power is not included in the analysis.

1.2 Aim and Objectives

The main goal of this thesis is to provide a numerical framework capable to trim the aerodynamic forces of a bird, leveraging on the in-house articulated lifting line (ALL) model.
In addition, my work retrieves and optimizes the aerodynamic power of the reference bird, tries to understand the effects of each flight kinematic parameter on the reference bird power curve and evaluates the trend of these parameters with respect to bird flight speed.
In the end, my thesis suggests possible directions for future researches.

2 Background Theory and Literature Review

2.1 What is a Gait?

In terrestrial locomotion, gait defines the pattern of movements executed by the limbs of animals. *"Gait is conventionally defined by temporal footfall patterns (...), the footfall sequence is the primary identifier of gait"* **(9)**. Human locomotion can be described by two gaits: walking and running. The transition between these two gaits is very abrupt and occur quickly. Figure 2.1 shows the major difference between walking and running; these two gaits are identified by distinct footfall patterns and speed. The gait selection is often based on speed and/or energy optimization.

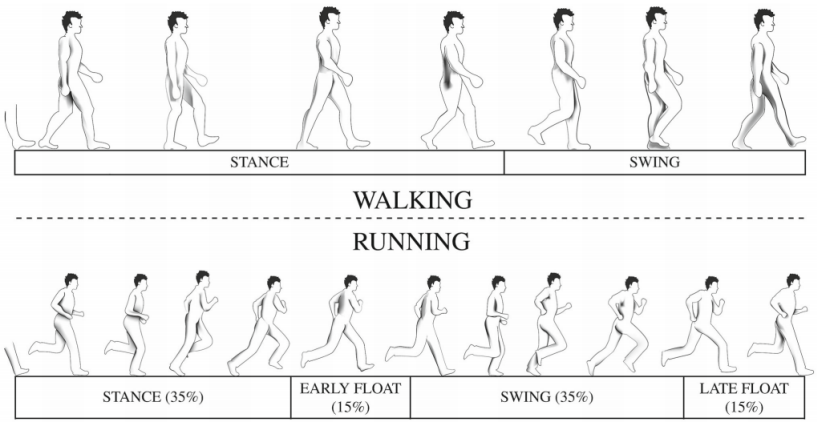

Figure 2.1: Human Gaits **(10)**

Terrestrial animals leave traces over a solid substrate: footprints. Through footprints is possible to estimate the footfall pattern of an animal and consequently its gait.

Flying animals do not leave concrete or visible footprints. The "footprints" of a bird are found in its wake.

The wake can be considered as the air impression of the bird wings motion. Having a clear and quantitative vision of these "footprints" is not an easy task.

Around 1980, Spedding et al. **(11)** analysed the wake of pigeon (*Columba Livia*) using Particle Image Velocimetry (PIV). Results showed that at low speed (i.e. $V_\infty = 2.4$ [m/s]) the wake of the pigeon was composed of discrete vortex rings. In this scenario, the upstroke seemed to be inactive. At higher speed (i.e. $V_\infty = 7$ [m/s]) the wake appeared completely different **(12)**; downstroke and upstroke wake elements were similar in term of circulation. This type of wake was then called: "constant circulation/continuous-vortex" wake. These wake distinctions lead to the notion of gaits in avian flight. In Figure 2.2 these two gaits are depicted.

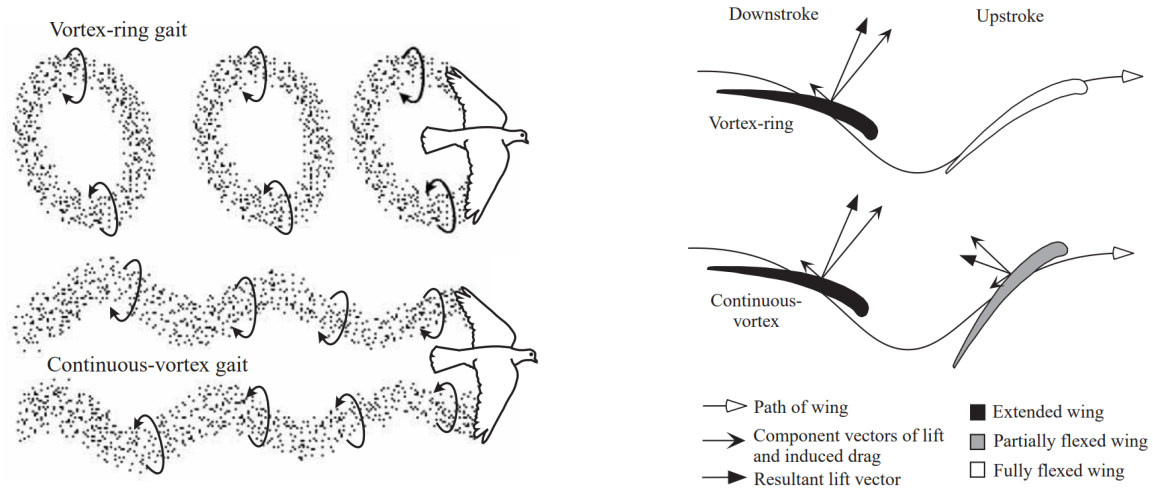

Figure 2.2: Two gait avian flight **(13)**,**(14)**

Despite this conclusion, the two gaits theory had two majors limitations. First, using PIV was impossible to demonstrate an abrupt transition between the two gaits; some early results even suggested a smooth transition rather than an abrupt one. Second, the so called "momentum deficit paradox", linked to the wake results of Spedding et al. **(11)**, did not have a clear explanation. The name "momentum deficit paradox" comes from the following observation: after a quantitative evaluation of the wake, the vortex rings generated by the pigeon contained only 1/2 of the momentum needed to support the bird. This paradox remained unsolved until the beginning of the 21st century.

In 2003, the technological advancements, redefined the PIV introducing the Digital Particle Image Velocimetry (DPIV) **(15)**,**(16)** that with its enhance resolution solved the "momentum deficit paradox".

The wake results, obtained through the DPIV, showed that upstroke was not inactive during slow flight; this was the missing piece. We will report the conclusion of **(16)**

"It appeared that the wake gradually transforms from discrete loops at slow speeds into a cc-like wake at typical cruising speeds. This transformation from a discrete loop to the cc-wake is probably achieved by the addition of an upstroke loop, end to end with the main downstroke loop, and as speed increases the upstroke wake structure is increased in strength to elongation until the downstroke and upstroke wake components form a continuous trailing wake of streamwise vortices with low amplitude cross-stream vortices"

and display the wake structure (cc = constant circulation, blue = downstroke, red = upstroke) in Figure 2.3.

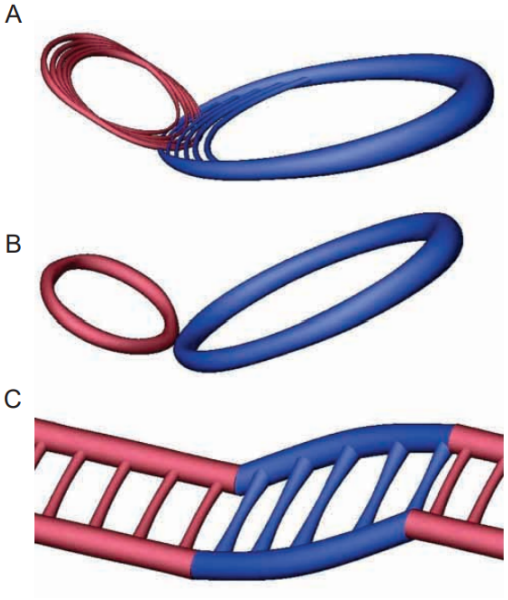

Figure 2.3: Bird wake structure at different speed: (A) = low (B) = medium (C) = high **(15)**

Ironically, the title of this thesis is outdated, the term gait should be replaced by the term flight kinematics. For the moment, there is no evidence of an abrupt change of these parameters during flight. Thus, avian locomotion can be described as continuous kinematic evolution.

Tobalske in his article **(13)**, illustrates the lateral view of a pigeon flying at steady speed (Figure 2.4). In this view is possible to appreciate, in qualitative manner, the evolution of the flight kinematic for various flight speed V_∞. The wingtips and wrist paths are highlighted in Figure 2.4.

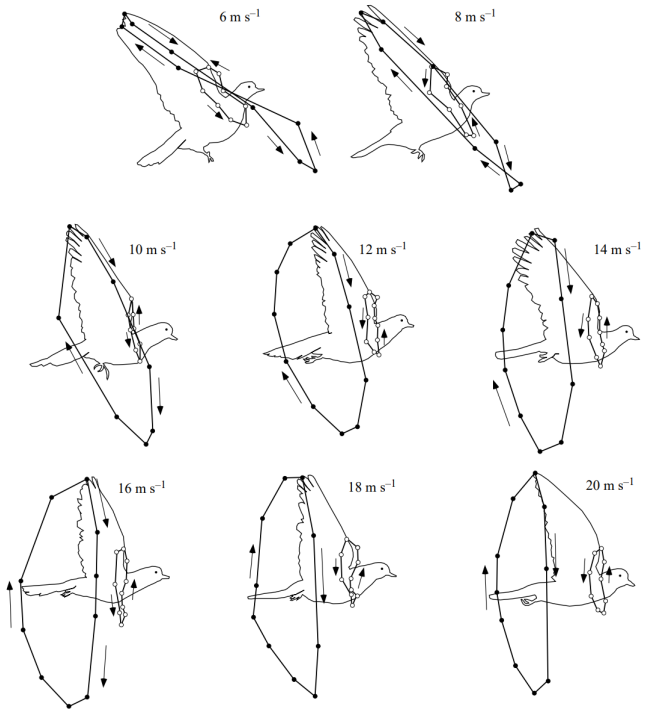

Figure 2.4: Lateral view of a pigeon flight kinematic in steady-speed flight conditions **(13)**

2.2 Allometric Equations

"Allometry, also called biological scaling, in biology, is the change in organisms in relation to proportional changes in body size. Scaling is often considered to be one of the few laws in biology" **(17)**. Allometric equations take the general form:

$$Y = am^b \tag{2.1}$$

where Y is some biological variable, m is the mass or the body size, a is a scaling constant and b is a scaling exponent.

These equations are often presented in a logarithmic form. In this work the allometric equations are used as tools to generalize, as much as possible, the analysed problem and to obtain an overview of the birds characteristics. Through these simplifications, the analysed model will depend only on the mass m of the bird. Most of the equations[2] of this chapter are adopted from the *chapter 13* of the book of Pennycuick **(19)**.

Pennycuick's book is a pillar for avian flight research, it regroups the lifetime work of Pennycuick **(20)**.

All the data of this section are derived from indoor or outdoor experimental observations.

First, we define the physical dimensions of the bird: wingspan b and wing surface/area S. The wingspan b is roughly proportional to $m^{1/3}$ and can be approximate by:

$$b = 1.165m^{0.394} \quad [\text{m}] \tag{2.2}$$

The wing surface/area S can be written as:

$$S = 0.1576m^{0.722} \quad [\text{m}^2] \tag{2.3}$$

In Figure 2.5 these two physical characteristics are depicted in a log-log plot:

[2]For a more broad view of the subject see (18)

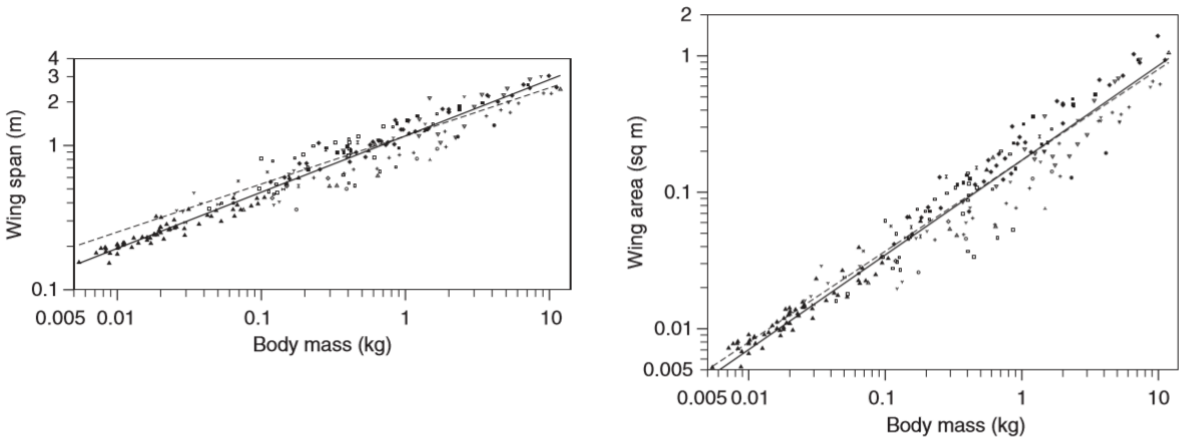

Figure 2.5: Wingspan and Wing area Allometric Plot **(19)**

Another important physical dimension that will be used to evaluate the parasitic drag, is the body frontal area S_b of the bird. This value defines the bird trunk area seen by the incoming airflow. The trunk of the bird is considered parallel to the flow in this scenario (flat plate analogy). The frontal area can be approximated by:

$$S_b = 0.00813m^{2/3} \quad [\mathrm{m}^2] \tag{2.4}$$

In section 5.1, the trunk fineness ratio FR_t will be fundamental for the calculation of the body drag coefficient C_{D_b}. The trunk fineness is defined as the length L_t of the bird trunk divided by the radius of the body frontal area R_f **(21)**:

$$FR_t = \frac{L_t}{R_f} = 6.08m^{0.1523} \quad [-] \tag{2.5}$$

Pennycuick defines also an allometric formula to describe the typical cruising flight flapping frequency f_{ref} of a bird:

$$f_{ref} = m^{3/8}g^{1/2}b^{-23/24}S^{-1/3}\rho^{-3/8} \quad [\mathrm{Hz}] \tag{2.6}$$

It would be interesting to validate a generic power curve model by comparing it to experimental fitted data. Norberg **(22)**[3] defines allometric equations describing the point of interest of a power curve; these equations will assert the validity of our model:

$$V_{mp} = 8.96m^{0.21} \quad [\mathrm{m/s}] \tag{2.7}$$

$$V_{mc} = 11.8m^{0.21} \quad [\mathrm{m/s}] \tag{2.8}$$

$$P_{mp} = 10.9m^{1.19} \quad [\mathrm{W}] \tag{2.9}$$

$$P_{mc} = 15m^{1.16} \quad [\mathrm{W}] \tag{2.10}$$

$$COT_{min} = 0.105m^{-0.036} \quad [-] \tag{2.11}$$

Alerstam et al.**(24)** give a better estimation of the minimum cost of transport speed V_{mc}; here 138 bird species of six main monophyletic groups are considered for the fit.

$$V_{mc} = 15.9m^{0.13} \quad [\mathrm{m/s}] \tag{2.12}$$

Having a rough estimation of the flapping amplitude ϕ of our reference bird, could also help us to validate a model. Ellington **(25)**, in 1991, derives an allometric equation describing the flapping amplitude ϕ during cruise flight:

$$2\phi = 67b^{-0.24} \quad [^\circ] \tag{2.13}$$

[3]These equations are obtained mixing experimental data with theoretical results **(23)**

Finally, we could set some boundaries to our model; C. M. Bishop **(26)** computes the maximum power output available continuously from bird wings muscles P_{max_M}. The fit considers 15 migratory birds with a body drag coefficient C_{D_b} ranging from 0.25 to 0.4 and mass m ranging from 0.01 kg to 10 kg.

$$P_{max_M} = 24.9m^{0.956} \quad [\text{W}] \tag{2.14}$$

Before introducing limitations to the power curve (minimum V_{min} and maximal V_{max} flight speed), the maximal wings muscular power P_{max_M} must be converted into maximal aerodynamic power P_{max_A}. The wings muscular power is given by:

$$P_{max_M} = P_{max_A} + P_{max_I} \tag{2.15}$$

where P_{max_I} is the maximal inertial power. This value is given the article of Van Den Berg et al.**(27)**; the fit is based on 29 different birds species (bird mass m ranging from 0.01 kg to 2.2 kg):

$$P_{max_I} = 7.75m^{0.799} \quad [\text{W}] \tag{2.16}$$

Finally the maximal aerodynamic power of a bird is given by:

$$P_{max_A} = 24.9m^{0.956} - 7.75m^{0.799} \quad [\text{W}] \tag{2.17}$$

2.3 Experimental Data

Around 1968, in his article **(28)**, Pennycuick conducted experiments on pigeons to understand their flight kinematic. A pigeon was trained to fly in a wind-tunnel and three cameras were used to capture wings motion. Additional information was obtained from a video sample taken on the roof laboratory of Bristol University. The relevant kinematic features obtained by Pennycuick can be find in the Figure 2.6. These data were extracted from the paper and set in accordance with our kinematic notation.

The graphs in Figure 2.6 depict respectively the flapping frequency f and the stroke-plane angle γ, of the pigeon analysed, respect to its flight speed V_∞. The flapping frequency seems to increase at low speed, reaches a minimum around the minimum power speed V_{mp}[4] and then slightly increases at high speed.

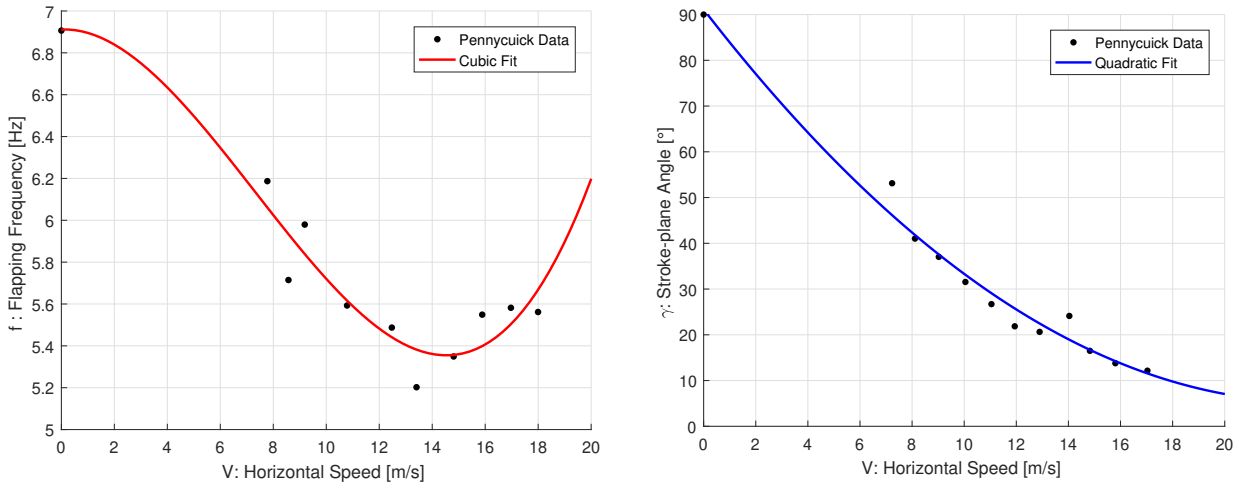

Figure 2.6: Flapping frequency f and Stroke-plane angle γ **(28)**

We could speculate that every bird has an optimal operating flapping frequency f_{opt} and this specific frequency minimizes the aerodynamic power P of that bird.

To reach higher speed V_∞, the bird has to increase its flapping frequency f consuming more power. Of course, the same approach applies for lower speed. Selecting flight conditions other than the optimal operating flapping frequency f_{opt} condition leads inexorably to an increase in aerodynamic power. This

[4]Based on Ben Parlsew**(32)**,**(36)**, V_{mp} ranges between 12-14 m/s

approach is too simplistic and in reality, the minimum power P_{mp} is defined by a multitude of flight kinematic parameters.

In general, the flapping frequency plays an important role during take-off and low speed flight. In these conditions, in fact, the bird has to rapidly generate lift and sustain itself without the support of the incoming airflow.

During cruising and high speed flight, f is fairly constant and oscillates around the reference frequency f_{ref} of the bird **(29)**.

Pennycuick, in **(30)**, studied the flapping frequency of a teal and a thrush nightingale. The two birds were trained to fly in a wind-tunnel and thus the frequency was evaluated over a vast range of flight speed. After his analysis, Pennycuick concluded that for the two birds the minimum aerodynamic power occurred in correspondence with the minimal frequency.

Experimental data led to the following expression describing the evolution of the flapping frequency with respect to the flight speed V_∞:

$$f(V_\infty) = A + \frac{B}{V_\infty} + CV_\infty^3 \tag{2.18}$$

where A, B and C are constants.

The concordance between minimal power and minimal frequency is not always true.
Conversely to what stated by Pennycuick, B. W. Tobalske et al. **(31)** showed that frequency in "*cockatiels reached a well-defined minimum at* 9 *[m/s], a speed* 80% *higher than their minimum power speed, whereas wing-beat frequency in doves showed a broad minimum from* 7 *to* 13 *[m/s]*".

Consequently, we are in the impossibility to understand the proper trend of the flapping frequency during flight.

Following the recent progress in the field **(32)**,**(33)**, the flapping frequency f in numerical analysis is often considered as a constant and this approach is adopted in this thesis.

The stroke-plane angle γ, using the notation of this thesis, is inversely proportional to the flight speed V_∞ of the bird. To understand this trend we will use as support Figure 2.7 where a helicopter is depicted in hovering and in forward flight conditions.

Of course, helicopters might differ from birds in term of flight mechanics but similarly to bird, they generate lift and thrust through a single apparatus[5].

In hovering condition, using the stroke plane analogy, the helicopter blades are in a parallel plane to the incoming flow V_∞ ($\gamma = 90°$); lift is produced (thrust is also generated but is considerably small compared to lift).

In forward flight condition, the helicopter tilts its blades, decreasing γ so that thrust and lift are produced. For obvious reasons, the blades tilt cannot reach the amplitudes achieved by birds.

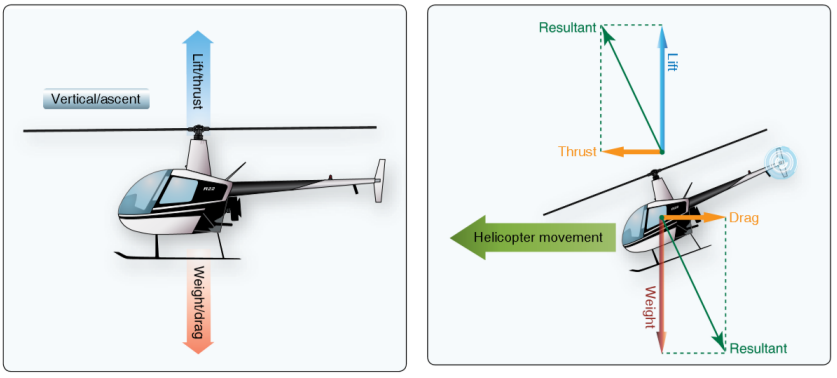

Figure 2.7: Stroke-plane angle γ helicopter analogy **(34)**

[5]The blades for the helicopter and the wings for the bird

Few birds can sustain hovering flight for long period of time[6], thus a stroke plane angle of $\gamma = 90°$ is rarely a reality.

During take-off, birds produce simultaneously lift and thrust, consequently the stroke plane angle γ is less than 90°.

Figure 2.8: Take-off stroke plane angle γ **(35)**

To reach higher speed, a higher horizontal propulsion is needed therefore, a smaller stroke-plane angle is selected by the bird. Decreasing γ at high speed is beneficial for the bird; the overall wing direction is closer to the airflow direction, reducing consistently drag resistance.

As shown in different numerical models **(32)**,**(33)**,**(36)**, the stroke plane angle γ tends to 0° without never reaching this value.

This behaviour can be explained, again, using the helicopter analogy; if the blades of the helicopter are perpendicular to the incoming flow[7] ($\gamma = 0°$) no lift can be produced consequently this condition is unrealistic.

Figure 2.9: Mid to high speed stroke plane angle γ **(35)**

However, it shall be pointed out that experimental data obtained by Tobalske et al. **(13)** shows that the stroke-plane angle γ of pigeons at really high speeds can reach 0°.

Therefore, at really high speed, the analogy birds with helicopters fails because in avian flight the stroke-plane angle is defined by an imaginary angle (average wing motion path) and in helicopter flight by a physical angle (the blades tilt).

Here we conclude the analysis of these two flight kinematic parameters. The trend of the others kinematic parameters will be discussed in the next chapters.

2.4 Power Curves Models

In this section, we review the most relevant articles that deal with avian power curves.

Before going into details, we start by summarising few basic concepts of the power curve theory. In the aircraft domain, the aerodynamic power is derived using the following equations:

$$L = \frac{1}{2}\rho S V_\infty^2 C_L \tag{2.19}$$

[6]Hummingbirds are an exception, insect-like flight characteristics

[7]This situation is not realistic a part for daredevil helicopter pilots

$$D = \frac{1}{2}\rho S V_\infty^2 C_D \tag{2.20}$$

$$C_D = C_{D_0} + \frac{1}{\pi \xi A} C_L^2 \tag{2.21}$$

Equations 2.19 and 2.20 are, respectively, the lift and the drag forces generated by the aircraft. In the equations ρ is the air density ($\rho = 1.225\ [kg/m^3]$), S the wings area, V_∞ the flight speed of the aircraft and C_L and C_D are the coefficients of lift/drag.

Equation 2.21 describes the airfoil polar. In this equation C_{D_0} comprises the friction and profile drag coefficient of the wings, A is the aspect ratio and ξ is the Musk span coefficient that is normally slightly less than 1.

By inserting first equation 2.19 in equation 2.21, then equation 2.21 in equation 2.20 and using $A = \frac{b^2}{S}$ with b as the wingspan of the aircraft, the subsequent relation is obtained:

$$D = \frac{L^2}{2\pi\epsilon\rho b^2 V_\infty^2} + \frac{1}{2}\rho S V_\infty^2 C_{D_0} \tag{2.22}$$

Finally, the power generated by the aircraft is simply given by the drag force multiplied by its flight speed, where the lift can be replaced by the weight of the aircraft (i.e. trim conditions $L = W = mg$):

$$P = \frac{m^2 g^2}{2\pi\epsilon\rho b^2 V_\infty} + \frac{1}{2}\rho S V_\infty^3 C_{D_0} \tag{2.23}$$

Equation 2.23 is composed of a first part inversely proportional to the flight speed ($\propto \frac{1}{V}$) and a second part proportional to the cube of the flight speed ($\propto V^3$). The first part corresponds to the induced power P_{ind} whereas the second one corresponds to the power required to overcome the air resistance[8] P_{drag}.

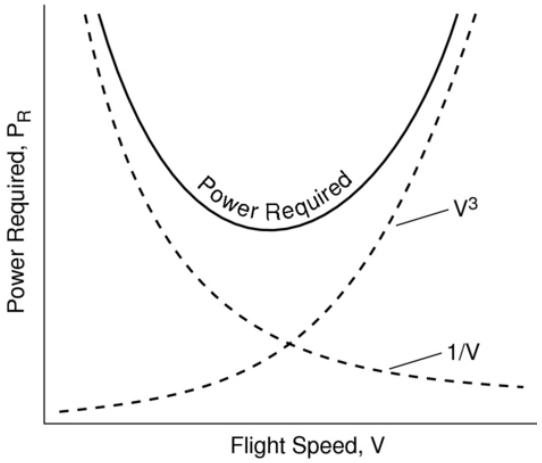

Figure 2.10: Power curve different contributions **(7)**

Going further, P_{drag} can be decomposed in the power needed to overcome the fuselage drag P_{par} (parasitic power) and wings profile drag P_{pro} (profile power). For a bird, all those power contributions are transposed as follow:

1. **Induced Power P_{ind}** → power generated by the flapping wings to sustain bird weight
2. **Parasitic Power P_{par}** → power needed to overcome bird body drag
3. **Profile Power P_{pro}** → power needed to overcome bird wings profile drag

Following this discussion each model present in literature suggests a specific expression for each of these power contributions.

Pennycuick, back in 1968, was the first to try to quantify the aerodynamic power of a bird. The innovative approach of his article **(28)** was to apply the actuator disk/momentum theory, often used to model helicopter or wind turbine, to model the induced power P_{ind} generated by a bird.

[8] Viscous effects and pressure distribution

The actuator disk theory or momentum theory, developed by Rankine **(37)** and Froude **(38)**, describes the effect of a rotor exerting a force on a fluid. The rotation of the blades generates a disk that is capable to sustain a pressure difference and accelerating the flow.

We suppose that this motion creates a stream tube axially symmetric as shown in Figure 2.11. The induced speed v_i of this actuator disk is derived through the conservation laws of mass, momentum and energy on a section of this stream tube. This speed v_i is then used to calculate the induced power of the actuator disk.

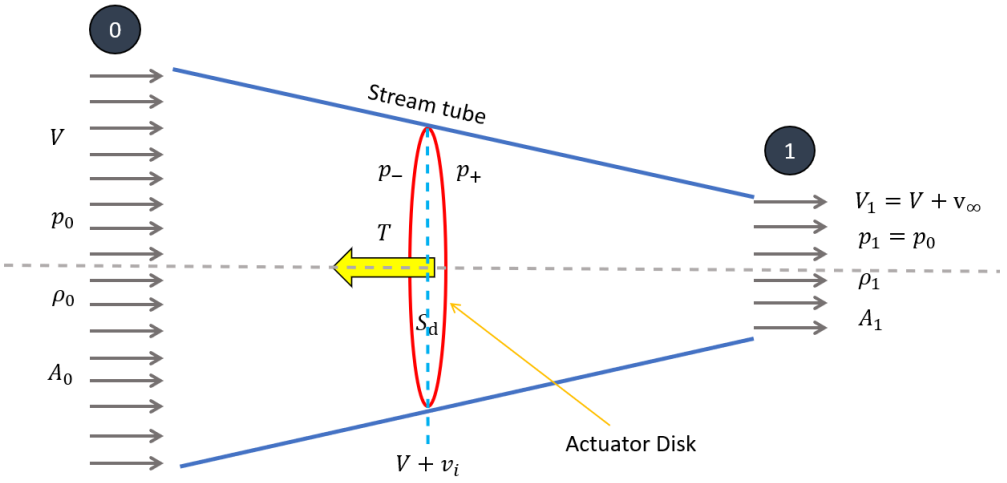

Figure 2.11: Momentum theory reference case

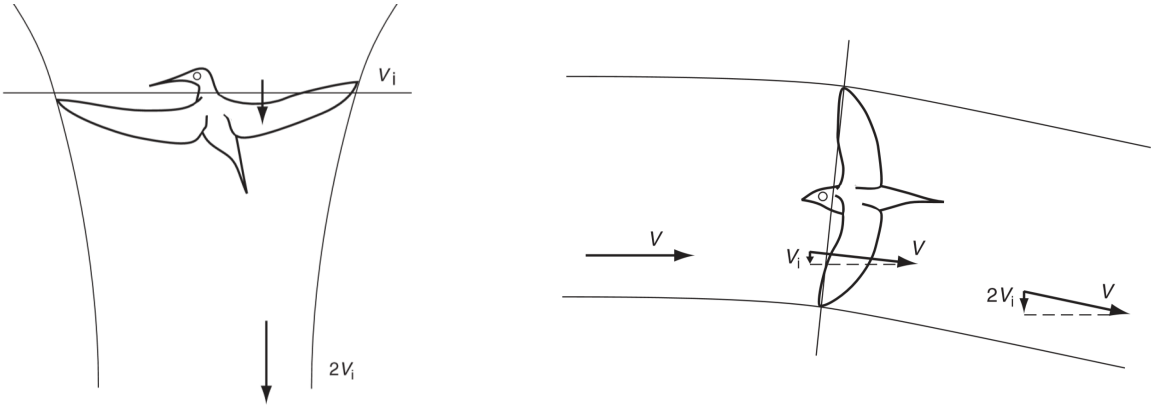

Figure 2.12: Momentum theory: hovering (left) and forward (right) flight **(19)**

The disk used in the model of Pennycuick is equivalent to the area swept by the wings of the bird (i.e circle of surface $S_d = \pi\frac{b}{4}$). The disk has to produce a lift L to sustain the weight $W = mg$ of the bird.

The following procedure is applied to retrieve the induced power P_{ind}: from the actuator disk theory we first derive the induced speed v_{i_h} (h = hovering) for hovering flight condition (i.e. flight speed $V_\infty = 0$), afterward, we conciliate the hovering and forward flight models (i.e. flight speed $V_\infty \neq 0$). Additional details are available in the book: "*Principles of Helicopter Performance*" **(39)**.

The air displaced by the bird is considered incompressible[9], consequently the Bernoulli theorem is applicable.

$$\frac{v^2}{2} + gz + \frac{p}{\rho} = constant \tag{2.24}$$

We suppose no variation in the flight altitude (level flight $\Delta z = 0$). With these assumptions the induced speed in hovering v_{i_h} condition and the induced force T can be written as:

$$T = W = mg = \rho S_d v_{i_h} v_\infty \tag{2.25}$$

[9]Other hypothesis: Unidirectional irrational fluid, friction is neglected

$$v_\infty = 2v_{i_h} \tag{2.26}$$

$$v_{i_h} = \sqrt{\frac{T}{2\rho S_d}} \tag{2.27}$$

The induced power P_{ind} is simply obtained by multiplying the induced force $T = W$ by the induced velocity:

$$P_{ind} = W v_{i_h} = \sqrt{\frac{W^{\frac{3}{2}}}{2\rho S_d}} \tag{2.28}$$

This is the power needed to sustain stationary/hovering flight. Using the same approach we can evaluate the induced power in forward flight condition.
For this condition, the induced force is equivalent to ($\mathbf{f}$ = forward):

$$T = W = 2\rho S_d (V_\infty + v_{i_f}) v_{i_f} \tag{2.29}$$

After solving this equation and by taking only the positive solution, the induced forward v_{i_f} speed can be written as a function of V_∞ and v_{i_h}:

$$v_{i_f} = -\frac{V_\infty}{2} + \sqrt{\frac{V_\infty^2}{4} + v_{i_h}^2} \tag{2.30}$$

The overall induced power model is summarised in the following formula:

$$P_{ind} = W v_{i_f} \tag{2.31}$$

The induced power, suggested by Pennycuick, respects the behaviour depicted in Figure 2.10; the more the bird flight speed V_∞ increases the more the induced power decreases.
At high speed, P_{ind} tends to zero. In his book **(19)**, Pennycuick points out that the above estimated power is too low compared to experimental data. Consequently, he suggested to add a correction factor to his model. He set this correction factor to a value of $k = 1.2$, the induced power is then given by:

$$P_{ind} = kW v_{i_f} \tag{2.32}$$

The correction factor must be considered as an approximation and might vary depending on the bird studied. One shall adjust this value to obtain results closer to the experimental data.

The actuator disk model has the benefit to be simple but does not reflect the reality of bird flight. In fact birds cannot continuously move their wings to generate a consistent stream tube. The actuator disk configuration of Figure 2.11 is more representative for insect flight than bird flight.

In his article **(28)**, Pennycuick calculates the profile power P_{pro} of his reference pigeon specifically using its wing. Unfortunately, this approach cannot be generalize. Therefore, in his book **(19)**, Pennycuick suggests using the following classical aerodynamics formula to retrieve the profile power of any bird, imposing the profile drag coefficient equal to $C_{D_{pro}} = 0.02 - 0.03$:

$$P_{pro} = \frac{1}{2}\rho S C_{D_{pro}} V^3 \tag{2.33}$$

The profile drag coefficient $C_{D_{pro}}$ is often calculated from frozen birds, therefore, it might be overestimated. In addition, this coefficient should vary depending on the specie and on the flight speed. The second parameter S, in the above equation, is the wing area of the bird and is expressed by the allometric relationship 2.3.

We shall also say that the flight speed V_∞ is only the mean speed seen by the overall wing structure. The reality is that each segment of the wing perceives a local speed different from V_∞. A proper way of evaluating P_{pro}, would be to compute the profile contribution of each wings segment and averaging the results over a flapping cycle. It is worth mentioning, that birds often fold their wings in upstroke reducing the overall profile power P_{pro}.

To complete the power curve model, we need to introduce the last power contribution: the parasitic power P_{par}. The parasitic power, as proposed by Pennycuick can be modelled similarly to the profile power:

$$P_{par} = \frac{1}{2}\rho S_b C_{D_b} V^3 \tag{2.34}$$

The bird body drag coefficient $C_{D_b} = 0.2-0.4$ was evaluated by Pennycucik using first frozen **(40)** and then living birds **(30)**. The frontal area of the bird S_b will change depending on the inclination of its body β.

Figure 2.13: Body angle β at low (left) and medium speed (right)

This dependency is due to the fact that when β increases a wider part of the bird body is exposed to the flow, generating more drag. The body angle β as shown in Figure 2.13 decreases with respect to the flight speed V_∞.

In forward flight we can assume that β is close to zero **(13)**. The factor β has a negative impact during take-off (high drag) and positive impact while landing (drag used to brake).

The second factor, the body drag coefficient C_{D_b}, varies depending on the flight speed **(21)**,**(40)**. Birds try to reduce their impact on the flow by changing their body morphology as the flight speed increases, thus reducing the value of C_{D_b}.

Pennycuick, before concluding his article **(28)**, carried out a discussion around the general performance limitations of birds. In this qualitative analysis, Pennycuick assumes that the power available P_{am} by a bird scale up as $m^{\frac{2}{3}}$ and that the power required P_r to fly scales up as $m^{\frac{7}{6}}$. These two quantities intersect around a value of $m = 12kg$, meaning that based on this qualitative analysis, birds heavier than this mass limit cannot fly.

Pennycuick goes further and look at the limitations in bird aerodynamic power setting two constraints: the maximum power available P_{am} and the maximum power continuously available P_{ac}.
Through this analysis, based on power curves[10], Pennycuick shows why some bird can hover and other cannot. He studied 4 birds and qualitatively highlights what part of the curve is exploited by the bird.

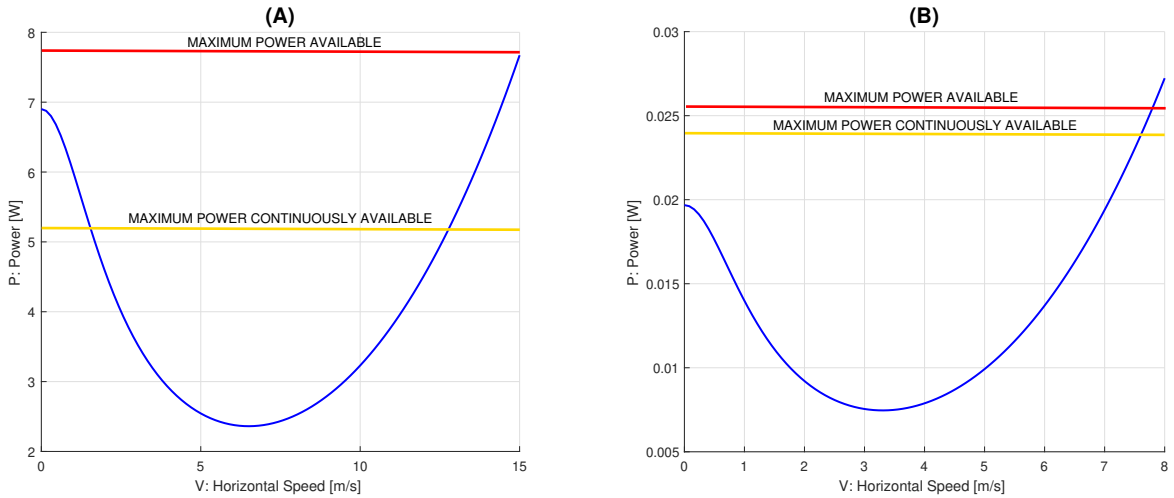

[10]All the power curves of Figure 2.14 are obtain using the above described model.

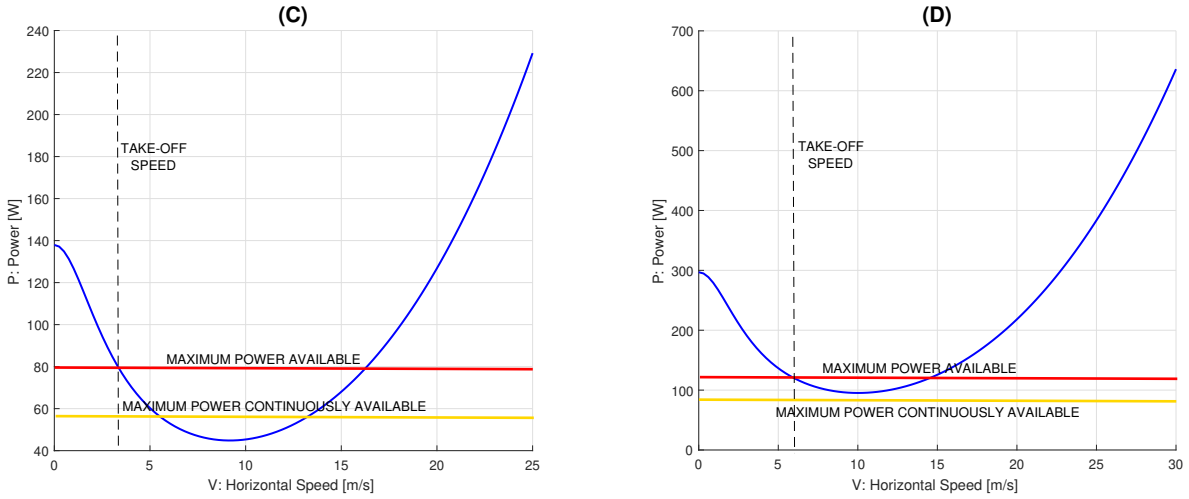

Figure 2.14: Reproduction of Pennycuick's analysis **(28)**

(a): Pigeon [$m = 0.4$ kg]

(b): Hummingbird (closer to insect flight) [$m = 0.02{-}0.2$ g]

(c): White-backed vulture [$m = 5{-}7$ kg]

(d): California condor [$m = 12$ kg]

In Figure 2.14 the upper horizontal lines represent P_{am} and the lower one P_{ac}, the vertical lines represent the take-off speed. From these diagrams we can state that pigeons are capable to sustain hovering flight for brief moments but cannot fly continuously at flight speed lower than approximately 2 m/s. Flying continuously at really high speeds seems impractical too.

On the other hand, hummingbirds ($m = 2{-}20$ [g]) are capable to continuously sustain hovering flight and any other types of flight.

Vultures ($m = 5{-}7$ [kg]) are not capable to hover but can fly continuously, as stated by Pennycuick, for roughly 5 min.

Finally, the California condors ($m = 12$ [kg]) are not capable to hover nor to sustain continuous horizontal flight. California condors might rely only on soaring and occasionally on flapping flight for take-off or evasion. Yet birds of this mass, for example the swan *Cygnus Olor*, are capable to migrate without soaring. This approach has to be consider as a simplistic tool that gives us a broad understanding on the typology of flyers. Here Pennnycuick concluded his study.

Only at the end of the seventies a novel approach describing avian power curves emerged.

In 1978, Rayner published the 2 parts article *"A vortex theory of animal flight"* **(41)**,**(42)**. In both parts, Rayner uses vortex theory to estimate the induced power P_{ind} of the bird considering bird flight as a vortex-ring gait.

In part 1 he focuses his study on hovering flight of insect and bird while, in the part 2 he introduces a new model to study birds steady forward flight.

We will first review part 1 and then discuss part 2.

Rayner's power curve models in contrast with Pennycuick's model takes into account the flight kinematic parameters of the bird studied. The following kinematic parameters are considered in Rayner's models:

- ϕ: Flapping amplitude
- γ: Stroke-plane angle
- $T = \frac{1}{f}$: Flapping cycle period
- β: Body angle
- τ: Downstroke ratio

The downstroke describes the depression phase of the flapping cycle, the upstroke defines the rest of the cycle: the elevation phase. The downstroke ratio is defined as the time spent in the depression phase divided by the flapping cycle period T. The upstroke in Rayner's models is considered as aerodynamically inactive.

The downstroke ratio τ is often equal to $\frac{1}{2}$ but can decrease/increase for different flight speeds.

In any case, it is irrelevant at very low speed but in fast forward flight a large τ can be beneficial for lift generation.
Increasing the downstroke ratio τ during fast flight has two advantages: first, the bird spends more time in downstroke therefore producing more lift over a flapping cycle, second less time is spent in upstroke consequently reducing the overall drag.

The flapping amplitude ϕ, in bird, generally ranges from 40° to 60° and can reach higher values (i.e. 90°) near hovering conditions; is high at very low speeds to rapidly generate lift and to lower the lift coefficient required to fly.

In part 1, Rayner evaluates hovering flight by estimating the vorticity present in the wake generated by an insect or a bird.

Rayner's model addresses the limitations and assumptions of Pennycuick's actuator disk (i.e. in momentum theory no vorticity is present in the wake, the wake has a well-defined boundaries where conservation laws can be applied) by developing a vortex model consisting of a chain of horizontal circular vortex rings stacked one above the others (Figure 2.15).

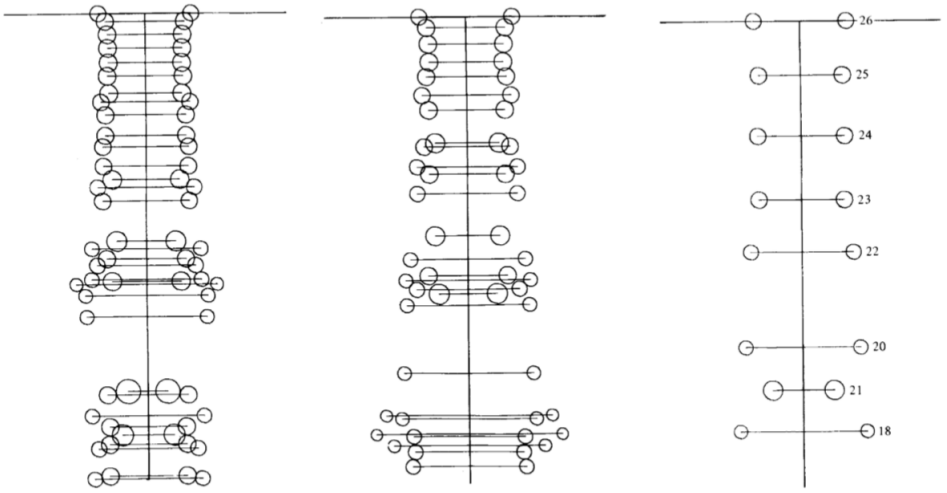

Figure 2.15: Wake of different flyers **(41)**: insect (left), small bird (centre), large bird (right)

The stream tube is discretized by the vortex rings generated at each wing stroke (thus not continuously). These rings have a proper kinetic energy (self-energy E_s) and can interact together (mutual energy E_m). The flapping amplitude ϕ of each stroke determines the area of the vortex sheet; smaller the amplitude smaller the area of the vortex.

In hovering flight conditions, we can suppose that the profile P_{pro} and parasitic P_{par} power are low compared to the induced power P_{ind}.

The induced power P_{ind} in this model is computed by taking the induced power $P_{ind_{AC}}$ derived from actuator disk theory and applying to it a correction factor σ. This correction factor considers the flight kinematic parameters of the bird, the morphology of the bird and the interaction of the vortex rings in the wake. Just to recall, in actuator disk theory the induced power, for hovering flight, is equal to:

$$P_{ind_{AC}} = \sqrt{\frac{W^{\frac{3}{2}}}{2\rho S_d}} \tag{2.35}$$

We introduce an adimensional parameter, called by Rayner feathering parameter f_p, that summarizes the physical morphology and flight kinematic of the bird. The feathering parameter is defined as the square of the ratio between the ideal induced velocity v_i of the actuator disk and the mean wingtip

velocity v_t. The tip velocity v_t is defined as the semi-circumference of the actuator disk divided by the stroke period $T_w = T$.

$$v_i = \sqrt{\frac{W}{2\rho S_d}} \tag{2.36}$$

$$v_t = \frac{\pi b}{2T_w} \tag{2.37}$$

$$f_p = \frac{u_i^2}{u_t^2} = \frac{mgT_w^2}{2\pi\rho S_d^2} \tag{2.38}$$

The correction factor σ is given by the ratio between the actual rate of energy increment in the wake $\frac{\Delta E}{T_w}$ and the rate of energy increment as derived by momentum theory $P_{ind_{AC}}$:

$$\sigma = \frac{\Delta E/T_w}{P_{ind_{AC}}} = f_p^{\frac{1}{2}} R'^{-3}(\bar{E}_s + \sum_{i=1}^{n} \bar{E}_m) \tag{2.39}$$

with E_s as the self energy, E_m mutual energy and R' as the vortex size reduction factor.

The factor adimensional R' is the ratio between the actuator disk of radius $\frac{b}{2}$ and the actual radius of the vortex ring. This factor is directly proportional to the flapping amplitude ϕ and is strongly related to the wing chord distribution $c(\xi)$.

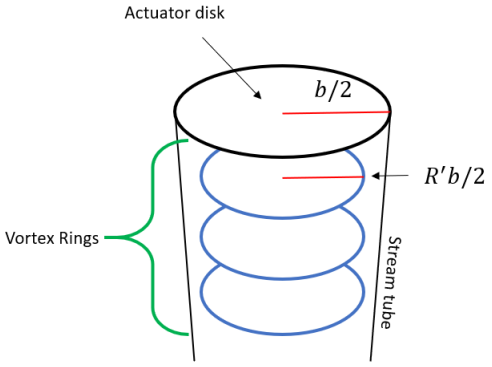

Figure 2.16: Vortex rings radius reduction

For small value of $f_p R'^{-4}$, the flyers wake is similar to the stream tube generated by an actuator disk of area $S'_d = \pi R'^2 \frac{b^2}{4}$. In this case, σ can be approximated by $\frac{1}{R'}$, thus $P_{ind} = \frac{P_{ind_{AC}}}{R'}$. This approximation is typically used to describe the flight of insects or really small birds (i.e. hummingbird = insect-like flight).
For larger birds this approximation is not appropriate and underestimates the induced power P_{ind}. Therefore, for large birds the correction factor σ can be approximated by:

$$\sigma = \frac{0.95}{R'} + \frac{1.2}{R'^5} f_p \tag{2.40}$$

$$P_{ind} = \sigma P_{ind_{AC}} \tag{2.41}$$

This conclude part 1 of Rayner's article; part 2 starts by introducing the following frame of reference:

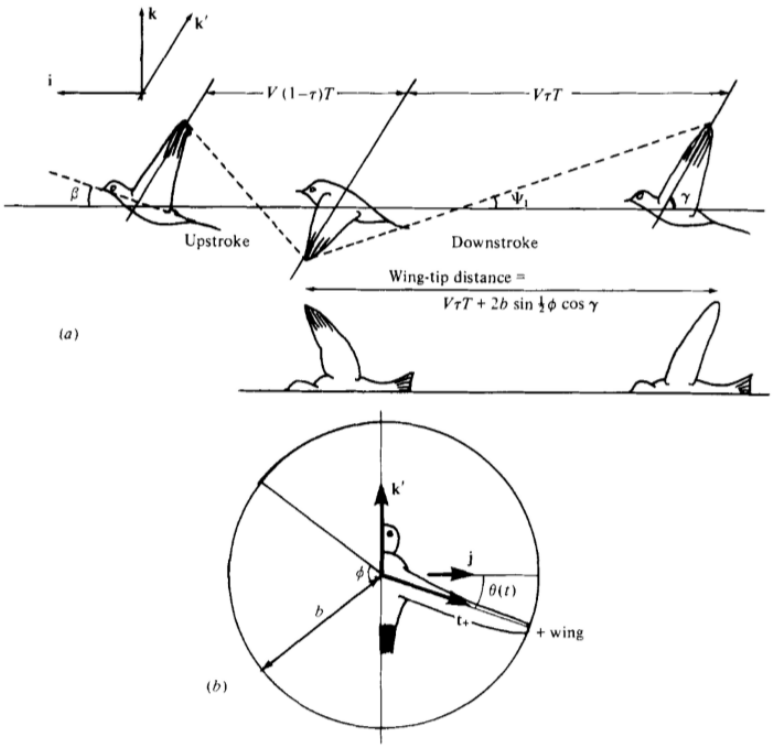

Figure 2.17: Reference frame: (a) Side view (b) Front view in the stroke-plane **(42)**

In Figure 2.17, the flapping amplitude ϕ, the wingspan b and the stroke-plane angle γ have a different definition respect to the rest of the thesis, in fact, ϕ is defined as a full stroke, b as the semi-wingspan and γ is equal to 90° when parallel to the airflow. Thus, all the equations related to part 2 of Rayner's article will follow these definitions.

The value of γ is not an input but the unknown of the model. The model is functional when the value of the stroke-plane angle is found.

In Figure 2.17 the depicted axes are:

- **i**: flight speed/thrust of the bird
- **k**: vertical speed/lift of the bird
- **j**: wingspan direction (positive for the right wing and negative for the left wing)
- **k'**: stroke plane angle direction (the angle between the plane and the horizontal $\mathbf{k'} = -\mathbf{i}\cos\gamma + \mathbf{j}\sin\gamma$)

In part 2, Rayner first introduces new models to evaluate the parasitic power P_{par} and the profile power P_{pro} and then explains the novel model to estimate the induced power P_{ind} of the bird. Our analysis will follow the same approach.

One of the criticism of Pennycuick parasitic power model P_{par} was the absence of the body inclination angle β in the equation. Rayner introduces this factor in his model. Here the body frontal area S_b and the body drag coefficient C_{D_b} are coupled in a single variable called equivalent flat plate area $A_{f_p} = S_b C_{D_b}$ expressed as follow [11]:

$$\boldsymbol{A_{b_p}} = -\boldsymbol{i}(A_b \cos^3\beta + A_a \sin^3\beta) + \boldsymbol{k}(A_b \sin\beta - A_a \cos\beta)\sin\beta\cos\beta \tag{2.42}$$

The two new areas A_f and A_a are described by two allometric formulas:

$$A_b = 0.00334 m^{\frac{2}{3}} \tag{2.43}$$

$$A_a = 0.045 m^{\frac{2}{3}} \tag{2.44}$$

[11] A_b is taken from Tucker **(43)**

The term A_b represents the frontal area of the bird at $\beta = 0$ whereas A_a considers the additional area (bird torso area) when $\beta \neq 0$. Rayner also suggested to set a relationship between the stoke plane angle γ and the body inclination β. The more γ increases the more β decreases. This relationship is represented by the following formula:

$$\beta = max(\beta_1 - \gamma, 0) \tag{2.45}$$

The value of β_1 lies between 35° and 80°. Rayner's parasitic model is synthesize in the equations below:

$$\boldsymbol{D_{par}} = \frac{1}{2}\rho \boldsymbol{A_{f_p}(\beta(\gamma))} V_\infty^2 \tag{2.46}$$

$$P_{par} = -\boldsymbol{D_{par}} V_\infty \boldsymbol{i} \tag{2.47}$$

Rayner continued his study by explaining the steps to evaluate the profile power of a bird. First, he selects a wing chord for the bird based on the research of Oehme & Kitzler **(44)**.

Oehme & Kitzler research showed that bird wings chord in general can be represented by the following shape:

$$\bar{c}(\xi) = \begin{cases} 1, & \text{for } 0 < \xi < \frac{1}{2} \\ 4\xi(1-\xi), & \text{for } \frac{1}{2} < \xi < 1 \end{cases} \tag{2.48}$$

This equation is normalized, $\bar{c(\xi)} = \frac{c(\xi)}{c_0}$ and $\xi = \frac{y}{b}$ where y is the distance of a wing segment from the root of the wing.

The angular position of the wing is assumed to be periodic during downstroke, thus the angular position for $0 < t < \tau T$ is given by:

$$\eta(t) = -\frac{1}{2}(\phi) \cos \frac{\pi t}{\tau T} \tag{2.49}$$

From this assumption is possible to evaluate the velocity of a wing segment $\boldsymbol{U_\pm}$ (negative = left wing, positive = right wing). With the velocity $\boldsymbol{U_\pm}$ the profile force per unit length can be retrieved:

$$\boldsymbol{F_{pro\pm}} = -\frac{1}{2}\rho c_0 \bar{c}(\xi) C_{D_0} U \boldsymbol{U_\pm} \tag{2.50}$$

where $C_{D_0} = 0.02$ and $c_0 = \frac{S}{2b}$ as the mean chord length.

Now that the profile force per unit length $\boldsymbol{F_{pro\pm}}$ is obtained, the mean profile drag can be written as:

$$\boldsymbol{D_{pro}} = -\frac{b}{T} \int_0^{\tau T} \int_0^1 (\boldsymbol{F_{pro+}} + \boldsymbol{F_{pro-}})\, d\xi\, dt \tag{2.51}$$

The total profile power P_{pro} is retrieved from the sum of the local profile drag experienced by each wing segment times the corresponding local velocity:

$$P_{pro} = -\frac{\mu b}{T} \int_0^1 \int_0^{\tau T} (\boldsymbol{F_{pro+}} \cdot \boldsymbol{U_+} + \boldsymbol{F_{pro-}} \cdot \boldsymbol{U_-})\, d\xi\, dt \tag{2.52}$$

The factor μ considers the work done during upstroke. It is defined as $1 + \frac{m_s}{m_p} = 1 + 0.1 = 1.1$; where m_p and m_s are respectively the masses of the pectoralis and the supracoracoideus muscles.
The first muscle is active during downstroke while the second one is active during upstroke. This correction is small, in fact the author assumes that the wing is fully retracted in upstroke, minimizing air resistance.

For better clarity, Rayner decided to adimensionalize the time t and flight speed V_∞ as follow:

$$\bar{t} = \frac{\pi t}{\tau T} \qquad\qquad \bar{V} = \frac{2 V_\infty \tau T}{b \phi \pi} \tag{2.53}$$

Using these adimensional values, the P_{pro} can be written as:

$$P_{pro} = \frac{\mu\rho b^4 c_0 C_{D_0}\phi^3\pi}{8\tau^2 T^3}\int_0^1\int_0^\pi \bar{c}(\xi)\bar{U}^3(\xi,\bar{t})\,d\xi\,dt \tag{2.54}$$

with $\bar{U} = (\bar{V}^2+2\bar{V}\xi\cos\gamma\sin\bar{t}\cos(\frac{1}{2}\phi\cos\bar{t})+\xi^2\sin^2\bar{t})^{\frac{1}{2}}$

To complete Rayner's model the induced power P_{ind} must be derived. The novel approach, proposed by Rayner, is described in the following text,

"*is to calculate the induced power as the rate at which kinetic energy is supplied to vortex-induced flows in the wake (...) The vortex sheet shed during each downstroke is assumed to become a plane elliptic vortex ring of small core radius. Each ring must support the bird's weight and overcome profile and parasite drags for the duration T of the stroke cycle. Successive rings are separated by self-convection and by the distance travelled by the bird in a time T. (...) The induced power is calculated as the increment in wake kinetic energy on the addition of a further member to the chain of vortices (assumed semi-infinite) formed by preceding wing-strokes*" [12].

In Figures 2.18 and 2.19 is possible to visualize the overall problem. The thick lines, in Figure 2.19, indicate the position of the vortex rings at different instant. The ring i is the newly generated, the other rings $i-1$, $i-2$, were created previously. The dashed lines indicate the initial positions of those old rings.

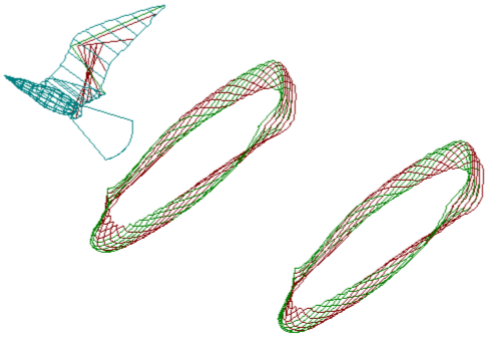

Figure 2.18: Vortex rings visualisation **(45)**

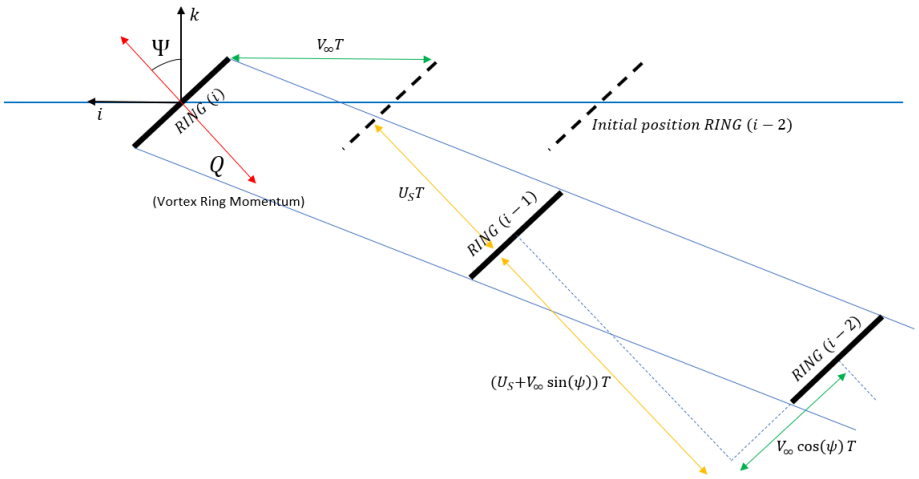

Figure 2.19: Image reproduction: Cross-section of the wake (Figure 3 of **(42)**)

A zoom on one of these rings reveals the diagram of Figure 2.20 that represents a vortex ring generation seen from the side $\boldsymbol{j}$.

[12] Quotes the article **(42)**

This will help us to define the momentum $|\boldsymbol{Q}|$ and the inclination Ψ of an elliptical vortex ring. In the diagram of Figure 2.20 H_1 and H_2 are the positions of the humeral joint at the beginning and at the end of downstroke.
Similarly, T_1 and T_2 indicate the positions of the wing tips at different points in time. The wing tips follow an elliptical arc and the trailing vorticity is assumed to form an elliptical ring. The ring extends from A_0 to A_2, the length of the ring is a fraction R' of the length between $T1$ and $T2$.
The oldest part of this ring A_0, is pushed downwards due to three different vorticity effects; its own vorticity, the vorticity bounded to the wings and the vorticity of the previous wake elements. This movement is approximately perpendicular to the airflow and at the end of downstroke the ring occupies the plane A_1A_2.
We suppose that Ψ_0 is small, thus, the variation in length between A_0-A_2 and A_1-A_2 is negligible.

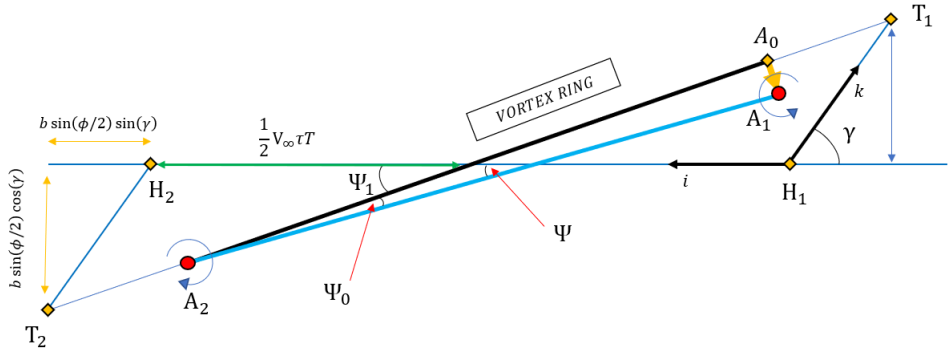

Figure 2.20: Image reproduction: Vortex ring close-up (Figure 2 of **(42)**)

The elliptical vortex ring generated at each wing-stroke, in a period T, must sustain and propel the bird. Therefore, from Figure 2.19, the ring momentum $|\boldsymbol{Q}|$ and inclination Ψ must satisfy the following equation:

$$|\boldsymbol{Q}|(\boldsymbol{i}\sin\Psi+\boldsymbol{k}\cos\Psi) = T(mg\boldsymbol{k}-\boldsymbol{D_{par}}-\boldsymbol{D_{pro}}) \tag{2.55}$$

In this equation, only the stroke-plane angle γ is unknown. Based on the geometry shown in Figure 2.20, we can write:

$$\Psi = \Psi_1-\Psi_0 \tag{2.56}$$

The unknown γ is retrieved by solving the equation 2.56. This value is fundamental to compute the parasitic P_{par} and the profile power P_{pro}.

The value Ψ_1 can be obtained again from Figure 2.20:

$$\tan\Psi_1(\gamma, V_\infty) = \frac{b\sin\frac{\phi}{2}\sin\gamma}{b\sin\frac{\phi}{2}\cos\gamma+\frac{1}{2}V_\infty\tau T} \tag{2.57}$$

Ψ_0 is the angle between the segments A_1A_2 and A_0A_2; the vortex rings formed at the end and at the beginning of downstroke. The value Ψ_0 depends on the wing circulation however since the convection velocity U_{s_0} is small compared to the freestream flow V_∞, Ψ_0 will be small in forward flight.

We define the transverse axis b_0 of the elliptic vortex as the semi-wingspan b times R' and the longitudinal axis a_0 as the product between R' and the length T_1T_2. The end A_0 of the ring roll up with the velocity of a circular ring[13] of radius $\frac{b_0^2}{a_0}$. We assume that the vortex has a core of radius $R_0(a_0b_0)^{\frac{1}{2}}$.

The adimensional core radius R_0 is difficult to calculate properly. Rayner set its value to 0.171, (i.e. a value known for elliptical rigid wing).

The circulation k of the vortex ring is given by the momentum $|\boldsymbol{Q}|$ divided by the area of the ring (area of an ellipse is equal to πa_0b_0).

[13]See the appendix of the Rayner's article for more information.

The quantities needed to evaluate Ψ_0 are summarized here below:

$$b_0 = bR' \qquad a_0 = R' \frac{b \sin\frac{\phi}{2} \cos\gamma + \frac{1}{2} V_\infty \tau}{\cos\Psi_1} \tag{2.58}$$

$$k = \frac{|\boldsymbol{Q}|}{\rho\pi a_0 b_0} \qquad U_{s_0} = \frac{k a_0}{4\pi b_0^2} \left\{ \ln\left[\frac{8}{R_0}\left(\frac{b_0}{a_0}\right)^{\frac{3}{2}}\right] - \frac{1}{4} \right\} \tag{2.59}$$

$$\tan\Psi_0 = \frac{1}{2} \frac{\tau T U_{s0}}{a_0} \tag{2.60}$$

We have now all the means to compute the induced power P_{ind} of the bird. The wake kinetic energy can be divided into two components:

- The self-energy E_s of the newly generated vortex ring
- The interactive/mutual energy between E_m this new formed ring and the previously formed rings

Let us define the major a_r and minor b_r semi-axes of an elliptical vortex ring:

$$a_r = max(a_0, b_0) \qquad b_r = min(a_0, b_0) \tag{2.61}$$

The elliptical vortex eccentricity is equal to:

$$e^2 = 1 - \frac{b_r^2}{a_r^2} \tag{2.62}$$

Through vortex theory, we can compute the self-energy E_s of this vortex:

$$E_s = \frac{1}{2}\rho k^2 a_r \bar{E}_s \qquad \bar{E}_s = \frac{2}{\pi}\left\{ E(e)\left[\ln\left(\frac{8}{R_0}\right) - \frac{3}{4}\right] - (1 - \frac{1}{2}e^2)K(e) \right\} \tag{2.63}$$

with K and E as the complete elliptic integrals of first and second kinds.

To evaluate the mutual energy contribution E_m the normalized vertical $\bar{b}a_0$ and horizontal $\bar{h}a_0$ spacing of two adjacent vortex rings must be defined.

Figure 2.21 represents two adjacent vortex rings and the vertical/horizontal spacing between them.

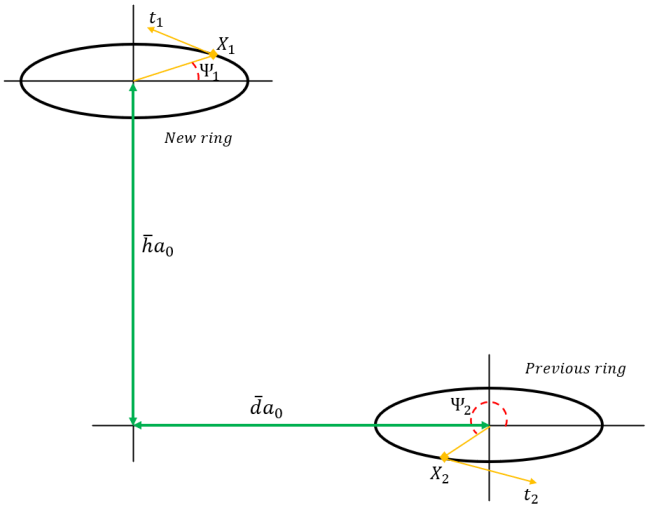

Figure 2.21: Image reproduction: Adjacent vortex rings (Figure 4 of **(42)**)

Skipping the intermediate calculations, the total mutual energy contribution E_m is defined as the sum of the contributions of all previously formed rings:

$$E_m = \frac{1}{2}\rho k^2 a_r \bar{E}_m \qquad \bar{E}_m = \frac{a_0}{a_r} \sum_{n=1}^{\infty} f_m^n\left(\frac{b_0}{a_0}, \bar{d}, \bar{h}\right) \tag{2.64}$$

$$f_m^n(\frac{b_0}{a_0},\bar{d},\bar{h}) = \frac{1}{2\pi}\int\int_0^{2\pi} \frac{\sin\psi_1\sin\psi_2+(\frac{b_0}{a_0})^2\cos\psi_1\cos\psi_2}{[(\cos\psi_1-\cos\psi_2-n\bar{d})^2+(\frac{b_0}{a_0})^2(\sin\psi_1-\sin\psi_2)^2+n^2\bar{h}^2]^{\frac{1}{2}}}\,d\psi_1\,d\psi_2 \tag{2.65}$$

When the bird flies at high speed, rings far in the wake make no significant contribution to the mutual energy. In fast forward the sum of mutual contribution converges approximately after $n = 5$ terms. At low flight speed more terms are necessary to converge. This implies that the induced power P_{ind} is inversely proportional to the flight speed:

- Low flight speed → High mutual energy → High induced power
- High flight speed → Low mutual energy → Low induced power

This is exactly the expected behaviour for the induced power.

The final formulation of P_{ind} is given by the sum of the self-energy and the mutual energy:

$$P_{ind} = \frac{1}{2}\rho k^2 a_r \frac{\bar{E}_s+\bar{E}_m}{T} \tag{2.66}$$

The total aerodynamic power of the bird is then equal to:

$$P(\phi, f, \tau, V) = P_{ind}+P_{par}+P_{pro}$$

Rayner's part 2 model overestimates the power at very low speed, close to hovering flight. A complete functional power curve model is obtained by combining part 1 and part 2 models. This conclude Rayner's work.

For a long time Pennycuik's and Rayner's models remained the only models capable of describing avian power curves. Due to the "momentum deficit paradox" and to poor computational power no major discoveries/innovations were made in this field before the 21^{st} century.

At the beginning of the new century Rayner, summarized and classified in his article **(46)** all the literature, of time, on avian power curves. He divided the literature models in 4 categories:

- *Blade Element*: models based on measured or estimated birds polar curve **(47)**,**(48)**.
- *Fixed-wing lifting-line*: models similar to Pennycuick's study **(28)**,**(49)**,**(50)**.
- *Flapping lifting-line*: modified lifting line theory suitable for flapping flight **(51)**,**(52)**.
- *Free Vortex*: models that use vortex theory as support to describe avian flight **(41)**,**(42)**,**(53)**.

In the same decade, through the DPIV, the "momentum deficit paradox" was solved.

Not long after this discovery, Tobalske **(54)** reviewed all the major researches of the avian flight field. In his work he manages to concentrate in a concise way nearly the totality of avian flight literature. Tobalske pointed out the lack of research around bird profile power P_{pro} and exhorted the public to develop new (or enhanced) mathematical models to unveil the secrets of avian flight.

In 2010, B. Parslew and W. J. Crowther, in their article "*Simulating avian wingbeat kinematics*"**(32)**, developed a new tool to understand bird flight kinematic. Their avian flight model was based on a multi-segment blade element[14].

The bird studied by Parslew and Crowther was a Rock pigeon (*Columba Livia*) and in their model the wing was divided in three segments: proximal arm, forearm and hand. With this tool it was possible to capture nearly any wing motion.

The model was optimized to obtain the minimum aerodynamic power P at each flight speed V_∞ and the optimization was conducted on four flight kinematic parameters (ϕ, θ, γ and the wing retraction factor e).

The results of this work found a good correlation with Pennycuick's experimental data. After these promising results, B. Parslew updated and enhanced his model in the articles **(36)**,**(61)**.

[14]With an actuator disk model supporting the model at low flight speed

In recent years, a research team of the Biology Department of Lund University developed an universal model describing avian power curves.

This milestone work is described in the article of M.Klein Heerenbrink et al.: *"Power of the wingbeat: modelling the effects of flapping wings in vertebrate flight"* **(33)**. We will take some time to explain the idea and the results of this article.

The principal goal of the research team was to formulate explicit expressions for the various parameters defining flapping flight and obtaining parametric power curves based on those expressions.

The main part of the study is the development of a numerical vortex wake model similar to the one of Hall & Hall **(52)**.
The innovative idea is to find the wake geometry that minimizes the aerodynamic power of the flyer, thus obtaining the optimal circulation distribution. This new model considers the following power contributions:

- Induced power P_{ind}
- Lift-dependent viscous power $P_{v,2}$ (not considered in any previous models)
- Zero-lift viscous drag $P_{v,0}$

The nature of this model is vastly explained in article **(33)**.

The viscous drag is expressed as $d_{vis} = \frac{1}{2}\rho c V^2 (C_{D_0} + C_{D_2} C_L^2)$ where V is the wing segment local velocity and c[15] the wing segment local chord. The lift-dependent coefficient is set to $C_{D_2} = 0.03$ and the zero-lift coefficient C_{D_0} here is given by the Blasius'flat plate boundary layer solution **(55)** assuming fully laminar attached flow:

$$C_{D_0} = \frac{2.66}{\sqrt{Re_c}} \tag{2.67}$$

with $Re_c = \frac{\rho c V^2}{\mu}$

Parasitic drag P_{par} contribution is not present in the wake model but it is added at a late stage to compute the total power P_{tot}. The frontal body area[16] S_b is equal to equation 2.4 and the parasitic drag coefficient is given by $C_{D_b} = 0.2$. Is worth mentioning that the values for S_b and C_{D_b}, used in this article, underestimate the parasitic drag at low speed V_∞ as proven by **(57)**.

The wake in article **(33)** is assumed to be periodic; downstroke and upstroke have the same duration and in addition the wing retracts during upstroke. The wake geometry is modulated by three different kinematic parameters:

- Flapping frequency: $f = \frac{1}{T}$
- Flapping Amplitude: ϕ
- Stroke plane angle: γ

The flapping frequency f is given by Equation 2.6 and the stroke-plane angle is 0° when parallel to the flight speed V_∞. The wing retraction is modelled as follow:

$$b_{min} = b \cos\phi \tag{2.68}$$

$$b_{red}(t) = \begin{cases} b, & \text{for } \frac{t}{T} < 0.5 \\ b_{min} + \frac{b - b_{min}}{2}[1 + \cos(4\pi \frac{t}{T})], & \text{for } \frac{t}{T} > 0.5 \end{cases} \tag{2.69}$$

In addition, the team assumes that the wake is not deformed or displaced. This assumption is satisfied only if the flight speed V_∞ is one or two order of magnitude larger than then induced velocity v_i. Implicitly this means that at low flight speed V_∞ the constraints of the model are violated.

In Figure 2.22 is possible to appreciate the representation of a plausible wake geometry.

[15] The wing chord is considered to have an elliptic distribution
[16] If the bird studied is passerine-like $S_b = 0.0129 m^{0.614}$ **(56)**

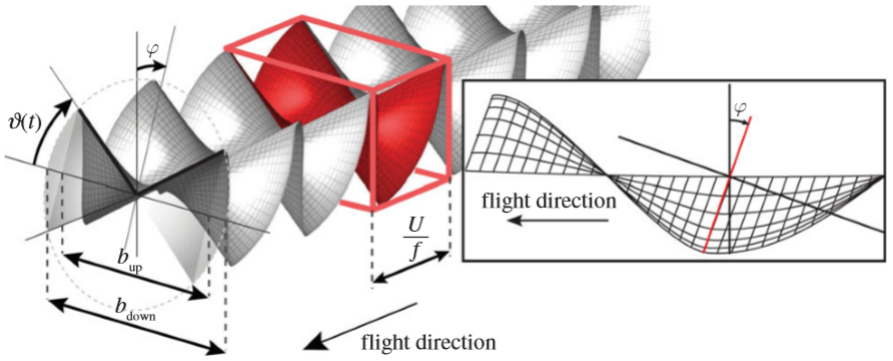

Figure 2.22: Wake geometry scheme **(33)**

The strength of Lund research team working frame is that it is characterized by only two parameters and is practically independent from the bird species physical attributes. Consequently, the problem can be generalized for different bird species. The fundamental adimensional parameters affecting the model are:

- Reduced frequency: $k_f = \frac{2\pi f b}{V_\infty}$
- Thrust ratio: $\frac{T}{L}$

The lift-dependent viscous drag might change from species to species and thus affecting the universality of the model. But as point out in the "electronic supplementary material (S2)" of the article, these changes from a species to another have a negligible impact on the model final results.

The wake geometry was optimized through the flapping amplitude ϕ: fixing a stroke-plane angle γ, ϕ was optimize for 200 random combinations of $\frac{T}{L}$, k_f, V_∞ and $\frac{L}{W}$; the sample ranges are reported in Table 1.

T/L	k_f	V_∞	L/W
0−0.3	1−6	3−20	0.2−3

Table 1: Sample Space

The research team had chosen these ranges in accordance with the experimental observations present in Pennycuick's book **(19)**. The flapping amplitude ϕ was set between 0° and 90°. The optimization was repeated for different stroke-plane angle γ ranging from 0° to 50° with steps of 10°.

The data obtained from this optimization can be fitted using a nonlinear regression. The flapping amplitude ϕ results are expected to depend on the thrust-ratio $\frac{T}{L}$ and the reduced frequency k_f. By plotting $\tan(\phi)$ as function of $\frac{T/L}{k_f}$ all the data can be approximated by the following numerical regression:

$$\phi = (1+qk_f)\arctan\left(p_{1/2}\left(\frac{T/L}{k_f}\right)^{1/r}+p_1\left(\frac{T/L}{k_f}\right)+p_4\left(\frac{T/L}{k_f}\right)^4\right) \tag{2.70}$$

In this function, the coefficients q, $p_{1/2}$, p_1 and p_4 are linked to the stroke-plane angle γ. The relationship between γ and these coefficients is expressed as a quadratic regression; the three coefficients $p_{i,0}$, $p_{i,1}$, $p_{i,2}$ of this quadratic regression are displayed in Table 2:

$$\bar{\gamma} = \tan(\gamma) \tag{2.71}$$

$$p_i(\bar{\gamma}) = p_{i,0}+p_{i,1}\bar{\gamma}+p_{i,2}\bar{\gamma}^2 \tag{2.72}$$

	$p_{1/2}$	p_1	p_4	q	r
$p_{i,0}$	1.277±0.048	6.214±0.125	227.8±12.7	0.0107±0.0008	2.620±0.047
$p_{i,1}$	/	/	/	0.0565±0.0014	/
$p_{i,2}$	/	3.631±	1481±42	−0.0169±0.0011	/

Table 2: Flapping amplitude ϕ fitted coefficients

Through the same procedure, drag and power components (D_{ind}, $D_{v,0}$, $D_{v,2}$ and P_{ind}, $P_{v,0}$, $P_{v,2}$) are fitted. Consequently, is possible to express the overall bird aerodynamic power P_{tot} as a parametric function proportional to $\frac{T}{L}$, k_f and γ.

These fitted equations can be found in the online library "AFPT – Animal Flight Performance Tool" created by Marco Klein Heerenbrink. In this library, Marco Klein Heerenbrink et al. work is written in R (programming language). The CRAN package containing Lund code can be found on the following website **(58)** and the documentation, for a better understanding of the code, is linked to the pdf **(59)**.

We will now comment the results of "AFPT – Aerodynamic model" when inserting the data of our reference bird. The AFPT takes as inputs the mass m (i.e. White Ibis 1.2 kg), the wingspan b and wing area S of bird and return the following output values:

Total Power	Stroke-plane angle	Flapping amplitude
$P_{tot}(V)$	$\gamma(V)$	$\phi(V)$

Table 3: AFPT Outputs

From those output values, we can derive the points of interest of the power curve. The power curve is limited by the maximum aerodynamic power P_{max_A} achievable by the bird. The P_{max_A} constraint is present in the AFPT but its formulation is not explicitly explained in the documentation of the code. This limitation adds to the model two other interesting points: the minimum V_{min} and maximum V_{max} flight speed.

In Table 4 all the points of interested are grouped and Figures 2.23, 2.24, 2.25 depict a reproduction of AFPT results.

Outputs of AFPT				
P.I.	V[m/s]	P [W]	γ [°]	ϕ [°]
V_{min}	5.668	22.86	49.9	43.4
P_{mp}	12.029	12.84	26.7	30.5
COT_{min}	16.024	14.93	18.3	32
V_{max}	21.168	22.86	12.1	38.9

Table 4: White Ibis Lund Outputs

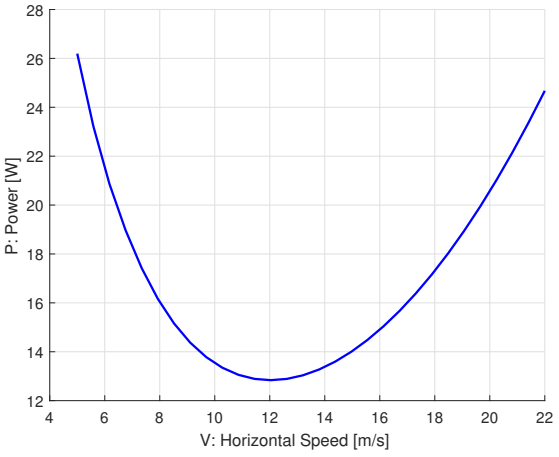

Figure 2.23: Reproduced Power Curve

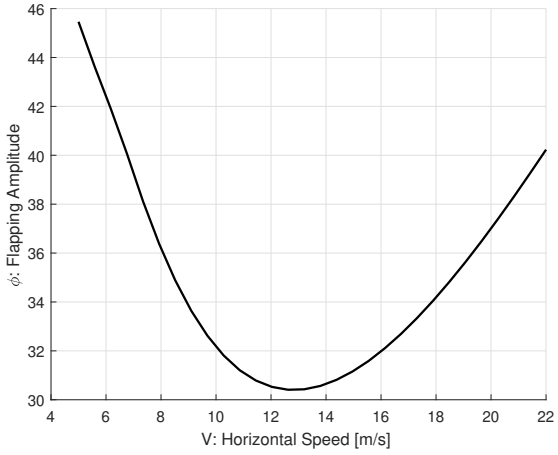

Figure 2.24: Reproduced Flapping Amplitude ϕ

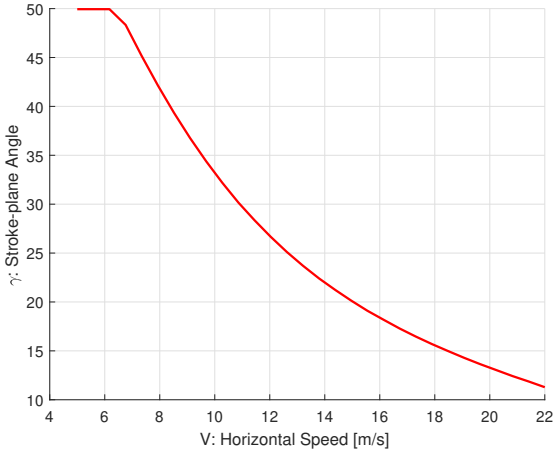

Figure 2.25: Reproduced Stroke-Plane Angle γ

The trend obtained for $\gamma(V_\infty)$ seems to follow what is expected in literature and it is close to the experimental data presented by Pennycuick in section 2.3. At low speed, γ reaches the maximum value (i.e. 50°) set by the model, flight speeds V_∞ lower than this point violate the constraints of the model.

Experimental data describing the evolution of bird flapping amplitude $\phi(V_\infty)$ are not available in literature however, B. Parslew **(36)** numerical results shows a similar trend to the one of the AFPT.

The flapping amplitude ϕ reaches a minimum in accordance with the minimum power P_{mp} and slightly increases when flight speed increases. At low speed, ϕ increases faster that at high speed. The overall trend of the flapping amplitude ϕ is similar to the trend of the flapping frequency f explained in section 2.3.

At low speed V_∞ the bird is in a transitory state (i.e. it will not remain in this state for a long time) and it has to sustain its weight without the support of the incoming flow. To maintain this flight state, a high flapping amplitude ϕ and a high flapping amplitude f are required.

In general, birds prefer flight zones between the minimum power and the minimum COT speed. These zones are optimal for any type of flight, because flapping frequency f and amplitude ϕ are at their minimum.

Of course, for evasion or hunting, birds must reach higher speed. This leads to a loss in term of performances. The required power for these flight zones is greater than the optimal flight zone but slightly smaller than the low speed zones.

The AFPT has a wide range of other functionality, for example is possible to change the frequency f of the flyer, to obtain the value of $P_{v,0}$, $P_{v,2}$, P_{ind} and P_{par} or to evaluate the flyer maximum climbing rate.

For the moment, the trend of the frequency f with respect to flight speed V_∞ has only been studied in **(36)** using a numerical optimization; a proper explicit expression for the flapping frequency $f(V)$ is not available in literature.

The bird lift-dependent viscous power $P_{v,2}$ is not well documented but Lund work **(33)** shows that its impact on the power curve is quite relevant. In Figure 2.26 all the power contributions of Lund model are displayed, the lift-dependent viscous power $P_{v,2}$ evolves similarly to the induced power P_{ind}.

Figure 2.26 is directly extracted from the R package: the red curve represents P_{ind}, the blue one $P_{v,2}$, the green one $P_{v,0}$ and the yellow one P_{par}.

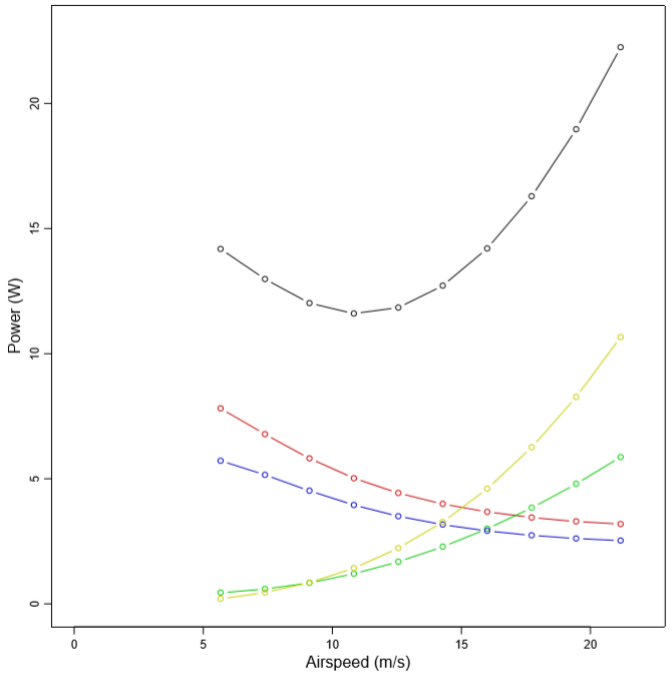

Figure 2.26: Lund Power curve different contributions

The work produced by Lund University, to the best of our knowledge, is the most up to date (Article

accepted date: 10/03/2015) analysis on power curves that can be found in the literature.

For this reason, this article has to be considered as pillar for future research in this field.

3 Aerodynamics of Flapping flight

After having summarized most of the available literature on power curves in the previous chapter, this chapter will now explain in an exhaustive manner the fundamental principles of flapping flight.

Throughout all this introductory discussion, the homonymous article *"Aerodynamics of Flapping flight"* **(62)** and the book *"An introduction to flapping wing aerodynamics"* **(63)** will be used as references.

A flapping cycle is often divided in two phases: downstroke and upstroke. Both phases are supposed to have the same duration. The flight is considered steady, level and periodic. The cycle duration is given by the flapping period $T = \frac{1}{f}$ of the bird.

During downstroke, the bird generates most of the lift needed to sustain its own weight and compensate the profile and parasitic drag by producing consistent thrust.

In upstroke, drag production is unavoidable, thus the bird will use some "techniques" to minimize this contribution. In addition, during this phase, a relevant lift is produced too.

Figure 3.1 shows a typical aerodynamic forces distribution over a periodic flapping cycle[17].

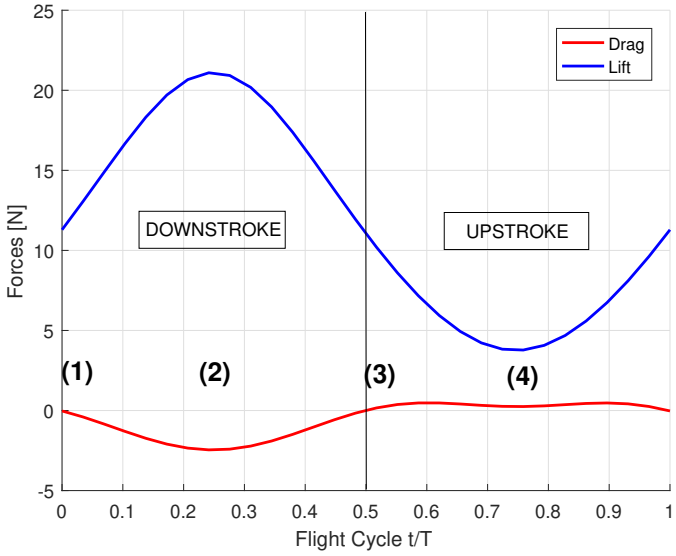

Figure 3.1: Example of Flapping cycle Forces (Trim conditions, White Ibis)

The following set of images (Figure 3.2) display the flapping cycle of a greylag goose **(64)**, starting from downstorke to upstroke:

- **(1)**: Start - Downstroke
- **(2)**: Mid - Downstroke
- **(3)**: End - Downstroke
- **(4)**: Mid - Upstroke

The wing during downstroke is tilted to ensure a similar angle of attack along all the wingspan. Vertical flapping motion near the shoulder joint is small therefore, tilting this part of the wing is unnecessary. On the other hand near the wingtip, the perceived vertical motion is high; tilt is needed to avoid stall.

[17] From flapping model of section 8.4

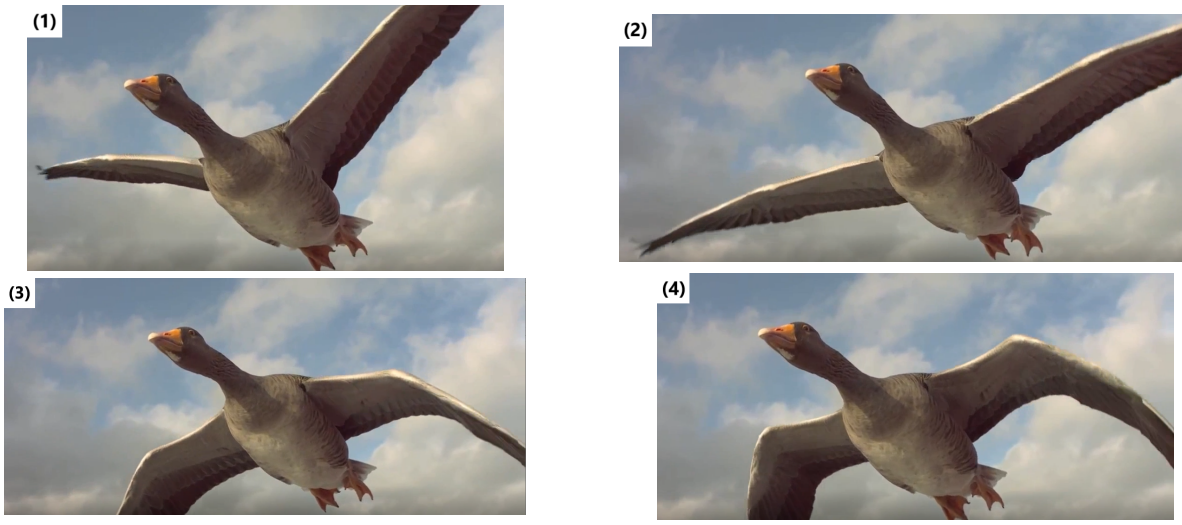

Figure 3.2: Flapping cycle of a greylag goose **(64)**

The upstroke motion is largely more complex motion than the downstroke phase. From the images **[3]** and **[4]** of Figure 3.2 is possible to state that roughly from the shoulder to the centre of the wing (arm), the angle of attack is close to zero (wing parallel to the airflow). This is fundamental to minimizes air resistance.

The outer part of wing (hand) is instead folded and retracted toward the body. These two motions are continuous during upstroke but are more pronounced around mid-upstroke. Through this "techniques", the bird manages to consistently reduce drag.

The folding motion could also have another role: Horst Räniger **(65)** stated that in presence of high lift in the area of the arm, folding could lead to a concentration of lift in the mid-span and consequently to thrust generation.

This discussion gives an overview of an avian flapping cycle, we can go further by defining the kinematics parameters describing the cycle. In a 2-dimensional space, a simple analysis of the flapping motion can be characterized by a plunging/pitching airfoil. The plunging motion is defined as the vertical displacement, in radians, of the airfoil and the pitching motion as the rotation of the airfoil along the wingspan direction.

We suppose that in steady flight both motions can be defined as periodic functions (Φ = plunging, Θ = pitching). The convection here is that the flight motion starts at the end of upstroke/beginning of downstroke, thus both plunging and pitching are written as:

$$\Phi(t) = \phi \cos(\omega t) \tag{3.1}$$

$$\Theta(t) = \theta_0 + \theta_1 \cos(\omega t + \eta) \tag{3.2}$$

here ϕ is the flapping amplitude, θ_1 is the pitching amplitude, θ_0 is the pitching offset, $\omega = 2\pi f$ is the angular speed and η is the phase difference between plunging and pitching.

The phase angle η is set to $\frac{\pi}{2}$. This ensures that the minimum pitching angle occurs when the plunging velocity perceived by the airfoil is at its maximum, allowing maximum aerodynamic force to be generated **(32)**.

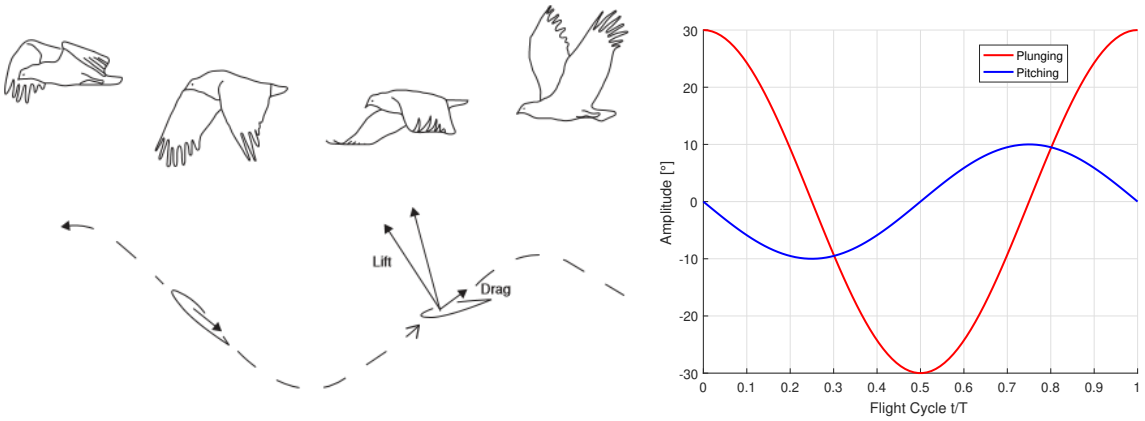

Figure 3.3: Representation of 2-D kinematics ($\phi = 30°$ and $\theta = 10°$) **(63)**

Through this simple model is possible to evaluate the angle of attack α_{ind} seen by the airfoil. Figure 3.4 displays the velocities and the forces generated by a plunging airfoil. The yellow dot in the figure is called pivot point (control point) and is often set at a distance of $\frac{1}{4}c$ from the airfoil leading edge. Velocities and forces are calculated on this specific point.

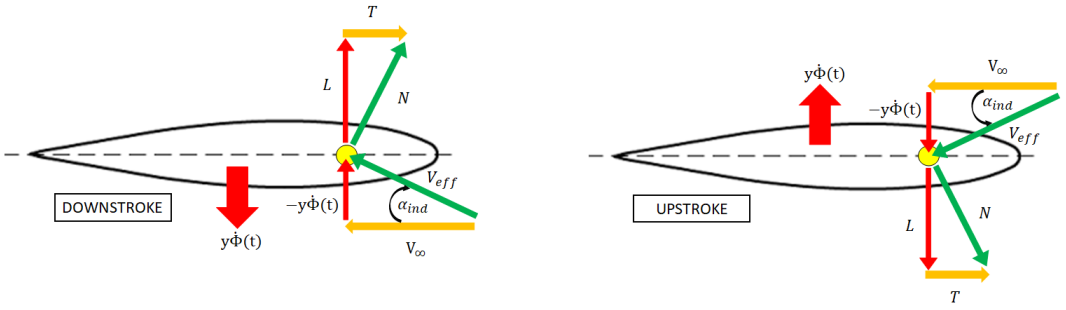

Figure 3.4: Angle of attack α_{ind} schematic

Based on this scheme the angle of attack α_{ind} of plunging airfoil can be written as (pl = plunging):

$$\alpha_{ind}(t) = \tan^{-1}\left(\frac{-V_{pl}(t)}{V_\infty}\right) = \tan^{-1}\left(\frac{-y\dot{\Phi}(t)}{V_\infty}\right) \tag{3.3}$$

where V_∞ is the flight speed and y is the distance of the airfoil from the shoulder. The minus sign is due the fact that the airfoil perceives an airflow opposite to the vertical displacement.

Pitching is fundamental to avoid high angles of attack when flapping amplitude $\dot{\Phi}(t)$ is too high or when flight velocity V_∞ is too low. Figure 3.5 depict the utility of the plunging motion, fundamental to avoid stall **(66)**. A plunging/pitching airfoil sees an effective angle of attack α_{eff} equal to:

$$\alpha_{eff}(t) = \Theta(t) + \alpha_{ind}(t) \tag{3.4}$$

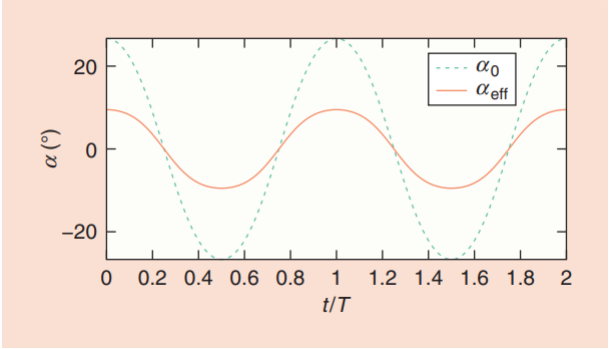

Figure 3.5: Role of the pitching angle **(67)** ($\alpha_0 = \alpha_{ind}$)

Another motion called sweep (forward/backward motion along the chord axis), hard to spot in Figure 3.2, occurs over a flapping cycle.

A better representation of the flapping flight aerodynamic, could be obtained using a 3-D model. Figure 3.6 depicts an example of 3-D kinematic. This example considers only the possible motions of the wing shoulder therefore, elbow and wrist joint are static.

In this frame:

- $\boldsymbol{x_0}$-axis flight speed V_∞ direction
- $\boldsymbol{y_0}$-axis is the wingspan direction
- $\boldsymbol{z_0}$-axis is set upward and perpendicular to the $\boldsymbol{x_0}$-$\boldsymbol{y_0}$ plane

The first frame rotation is respect to the $\boldsymbol{y_0}$-axis and defines the stroke plane (rotation $\boldsymbol{\gamma}$). The amplitude of the stroke plane angle γ is different depending of the phase (down/upstroke), but is often consider γ as equal along both phases.

The second rotation defines the flapping/plunging plane (rotation $\Phi(t)$), the frame rotates around the $\boldsymbol{x_\gamma}$-axis.

Successively, the frame rotates around the $\boldsymbol{y_\Phi}$-axis to describe the pitching plane (rotation $\boldsymbol{\Theta(t)}$).

Finally, in order to integrate in the model a sweeping motion, we apply a frame rotation of $\Psi(t)$ around the $\boldsymbol{z_\Theta}$-axis.

All the rotation matrices are reported here below and in Figure 3.6 is possible to visualize the different frames[18]; for a better clarity, we avoid to insert time dependence in the rotation matrices.

A similar flapping flight frame to Figure 3.6 is used in the model presented in the appendix 8.4. The model described in 8.4 was an attempt of understanding bird flight kinematic with a simpler tool than the articulated lifting line (ALL). A great amount of time was spent in its realisation. This model would have given an intermediary analysis between the literature models and the ALL model. The model took inspiration from B. Parslew **(32)**,**(36)**,**(61)**, work but unfortunately, even if promising, it did not return correct flight kinematic result nor good power curves trend when trimmed. Therefore, it was not considered in the main body of this thesis however, it is available in the appendix as complementary work of this thesis.

$$R_y(\gamma) = \begin{bmatrix} \cos\gamma & 0 & \sin\gamma \\ 0 & 1 & 0 \\ -\sin\gamma & 0 & \cos\gamma \end{bmatrix} \qquad R_x(\Phi) = \begin{bmatrix} 1 & 0 & 0 \\ 0 & \cos\Phi & -\sin\Phi \\ 0 & \sin\Phi & \cos\Phi \end{bmatrix} \tag{3.5}$$

$$R_y(\Theta) = \begin{bmatrix} \cos\Theta & 0 & \sin\Theta \\ 0 & 1 & 0 \\ -\sin\Theta & 0 & \cos\Theta \end{bmatrix} \qquad R_z(\Psi) = \begin{bmatrix} \cos\Psi & -\sin\Psi & 0 \\ \sin\Psi & \cos\Psi & 0 \\ 0 & 0 & 1 \end{bmatrix} \tag{3.6}$$

[18] Attention in Figure 3.6 pitching is called feathering ($\Theta = \alpha$) and sweeping is called elevation ($\Psi = \theta$).

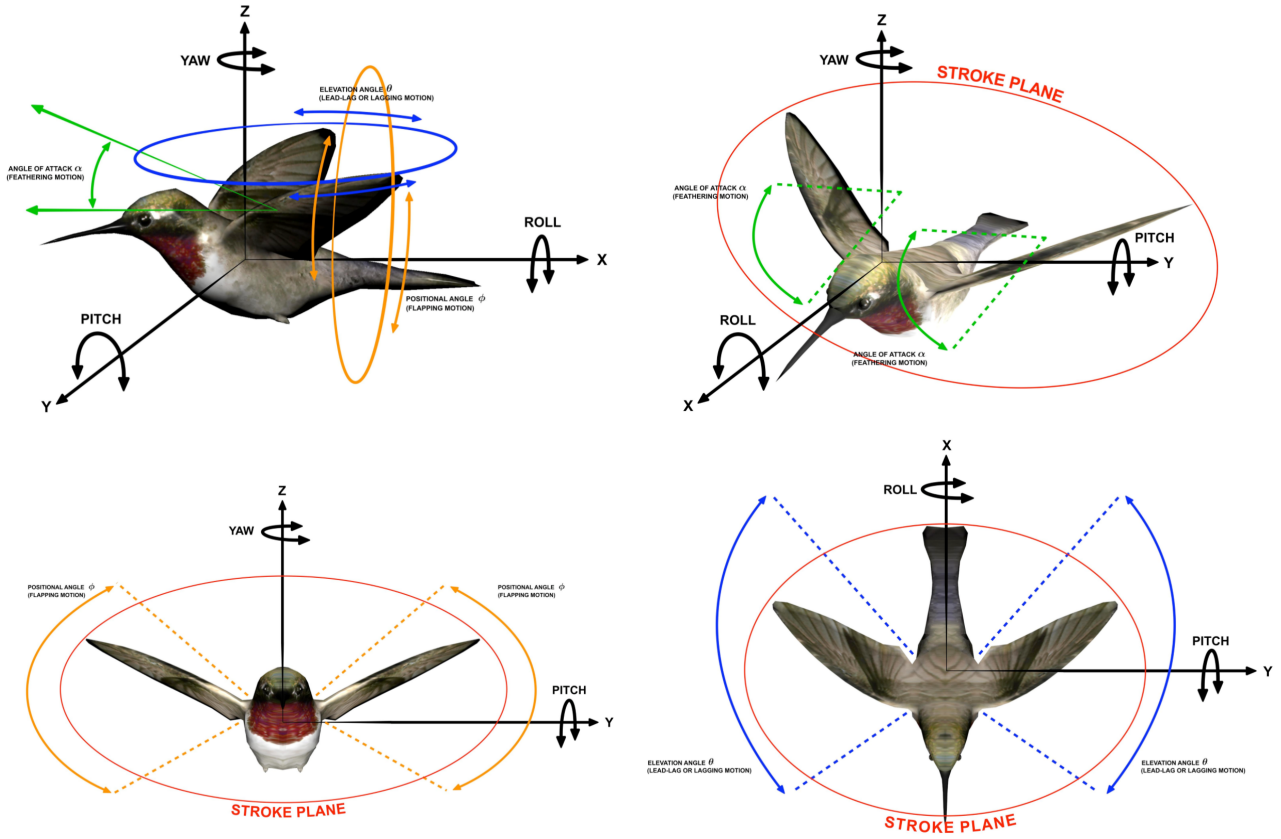

Figure 3.6: 3-D Kinematic Model **(62)**

Before concluding this discussion, the wing retraction and wing folding motions have to be addressed to simulate as close as possible avian flight.

For the wing retraction, we refer to section 2.4 were the wing retraction formula (2.68, 2.69) suggested by M.KleinHeerenbrink et al.**(33)** is presented. We suppose, here, that the retraction is independent from the flapping amplitude ϕ thus b_{min} of equation 2.68 can be written as:

$$b_{min} = b\cos\epsilon \tag{3.7}$$

where ϵ is the retraction factor (in radians); Figure 3.7 displays the trend of this kinematic parameter.

For the wing folding, B. Parlsew in his thesis **(61)**, implements this motion by dividing the wing in two part: arm and hand. The arm goes from the shoulder joint to the wrist joint whereas the hand goes from the wrist to the wingtip. Only the hand of the wing is subjected to the folding motion and thus rotates by an angle Σ along the chord direction ($\boldsymbol{x_\psi}$-axis).

The rotation matrix describing this motion can be expressed as:

$$R_\Sigma(\Sigma) = \begin{cases} \begin{bmatrix} 1 & 0 & 0 \\ 0 & 1 & 0 \\ 0 & 0 & 1 \end{bmatrix}, & \text{for } y < y_w \\ \begin{bmatrix} 1 & 0 & 0 \\ 0 & \cos\Sigma & -\sin\Sigma \\ 0 & \sin\Sigma & \cos\Sigma \end{bmatrix} & \text{for } y < y_w < b/2 \end{cases} \tag{3.8}$$

where y_w is the position of the wrist joint.

In his thesis, B. Parslew provides few information regarding the behaviour of the angle Σ. We could speculate, based on everyday observation, that wing retraction and wing folding are directly proportional to the airflow speed V_∞: when a bird increases its speed, wing folding and wing retraction

are accentuated. The numerical results of **(61)** and the experimental data of **(68)** indicate that wing retraction follows this trend.

From the flapping cycle of a greylag goose (Figure 3.2) is possible to extract a plausible trend of Σ. The folding motion is present only in the upstroke phase, its angular frequency is similar to the one of the flapping motion and the value Σ can be considered negative over all the upstroke. Using these hypothesises and assuming that the maximum fold occurs during mid-upstroke, we can express Σ as:

$$\Sigma(t) = \begin{cases} 0, & \text{for } y < t < T/2 \\ -\sigma \cos\left(wt + \frac{\pi}{2}\right), & \text{for } T/2 < t < T \end{cases} \tag{3.9}$$

Finally, it is worth mentioning that the flapping cycle is not always symmetric, sometimes the downstroke is faster than the upstroke and vice versa. The factor τ, the downstroke ratio, take into account this difference. Every motion, described in this introductory discussion, can be rewritten as a function of τ; in Figure 3.8 the new plunging and pitching motion are shown:

$$\Phi(t) = \begin{cases} \phi \cos(\frac{\omega}{2\tau} t), & \text{for } 0 < t < \tau T \\ \phi \cos[\frac{\omega}{2(1-\tau)}(T-t)], & \text{for } \tau T < t < T \end{cases} \tag{3.10}$$

$$\Theta(t) = \begin{cases} \theta_0 + \theta \cos(\frac{\omega}{2\tau} t + \eta), & \text{for } 0 < t < \tau T \\ \theta_0 + \theta \cos[\frac{\omega}{2(1-\tau)}(T-t) + 3\eta], & \text{for } \tau T < t < T \end{cases} \tag{3.11}$$

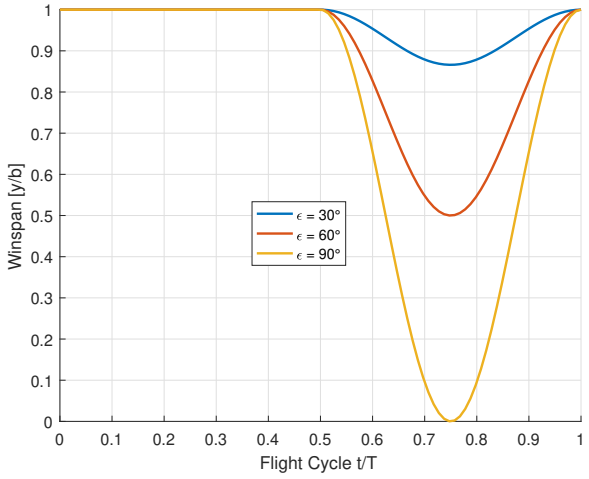

Figure 3.7: Wing Retraction

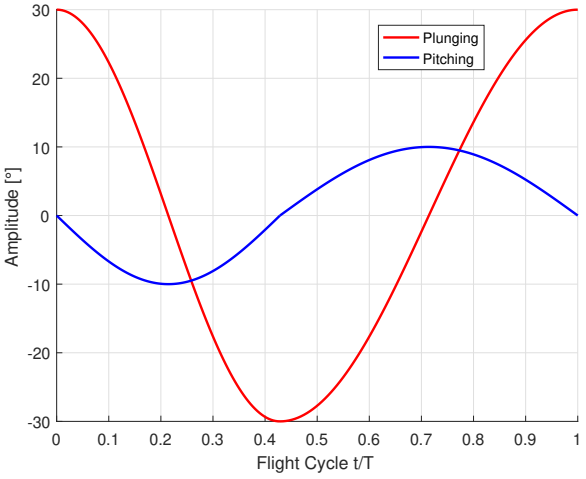

Figure 3.8: Asymmetric kinematics ($\tau = 3/7$)

3.1 Articulated Lifting Line Model

This section describes the aerodynamic model employed to compute the aerodynamic power of the reference bird. We used an articulated lifting line (ALL) developed within the RevealFlight network, which defines the motions of a bird wing and evaluates the aerodynamic loads acting on it for a specific flight speed V_∞.

The ALL model applies Prandtl's lifting line theory **(69)** to the articulated wing skeleton of a White Ibis. The wing of the bird is divided in 3 joints and 3 segments. Three rotations are associated to each joint. These rotations capture the flight kinematics of the bird.

The joints of the bird skeleton[19] are sketched in Figures 3.9 and 3.10:

- Shoulder (S)
- Elbow (E)
- Wrist (W)

[19] Figure 3.9 only depicts one wing but the model takes into account both wings.

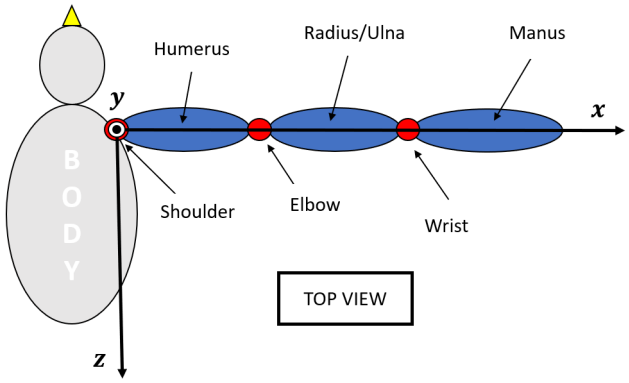

Figure 3.9: Model frame of reference

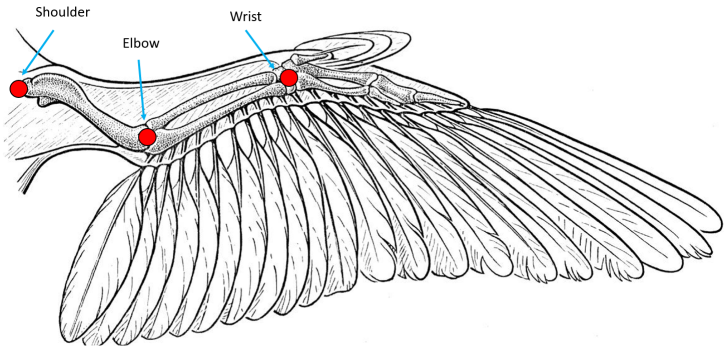

Figure 3.10: Real avian wing

ALL reference frame is decomposed in three axes, accordingly to a right-handed frame, and is centred around the shoulder joint:

- [**x**]-axis: Wingspan direction
- [**y**]-axis: Lift direction
- [**z**]-axis: Chord-wise/incoming airflow V_∞ direction

The rotation around the **x**-axis is defined as a pitching motion, the one around **y**-axis as a sweeping motion and the one around **z**-axis is equivalent to a plunging motion.

The flapping cycle, in this model, starts at mid-downstroke. The elbow and wrist rotation are constrained respectively in the **z**-axis and in the **x**-axis. These two constraints replicate the limitations of real flyers elbow and wrist. Consequently, the ALL can achieve in total 7 types of rotations (3 S; 2 E; 2W). These rotations can be formalized by the following equation:

$$\alpha_{i,j}(t) = \alpha_{0_{i,j}} + \alpha_{1_{i,j}} \sin(\omega t + \eta_{i,j}) \tag{3.12}$$

with i and j as the axis of rotation and the rotating joint, α_0 as the offset angle, α_1 as the amplitude angle, $\omega = 2\pi f$ as the angular frequency and η as the phase angle.

The flapping frequency $f = 4$ [Hz] of the model is considered as a constant for most part of the thesis. This frequency was selected using the available data for this scale of birds.

For better clarity each rotation is divided in three categories: plunging $= \phi_j$ (**z**-axis), pitching $= \theta_j$ (**x**-axis) and sweeping $= \psi_j$ (**y**-axis).

$$Shoulder = \begin{cases} \phi_S(t) = \phi_{0_S} + \phi_{1_S} \sin(\omega t + \eta_{\phi_S}) \\ \theta_S(t) = \theta_{0_S} + \theta_{1_S} \sin(\omega t + \eta_{\theta_S}) \\ \psi_S(t) = \psi_{0_S} + \psi_{1_S} \sin(\omega t + \eta_{\psi_S}) \end{cases} \tag{3.13}$$

$$Elbow = \begin{cases} \theta_E(t) = \theta_{0_E} + \theta_{1_E} \sin(\omega t + \eta_{\theta_E}) \\ \psi_E(t) = \psi_{0_E} + \psi_{1_E} \sin(\omega t + \eta_{\psi_E}) \end{cases} \tag{3.14}$$

$$Wrist = \begin{cases} \phi_W(t) = \phi_{0_W} + \phi_{1_W} \sin(\omega t + \eta_{\phi_W}) \\ \psi_W(t) = \psi_{0_W} + \psi_{1_W} \sin(\omega t + \eta_{\psi_W}) \end{cases} \tag{3.15}$$

The ALL wings are divided n segments (from $-b/2$ to $b/2$) and the kinematic is discretized temporally (from 0 to $T = \frac{1}{f}$) in m steps (Figure 3.11). The kinematic velocity $\vec{v}_k$ is computed trough a numerical derivative between two temporal state of the wings.

The kinematic velocity $\vec{v}_k$ is fundamental to compute the wings effective angle of attack α_{eff} that is then inserted in the lifting line developed by the research team.

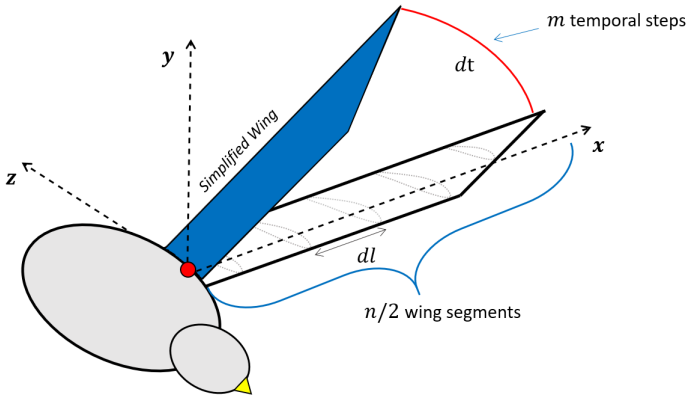

Figure 3.11: Model discretization

Once extrapolated the wing envelope at each time step, the resulting aerodynamic force is computed via the Prandtl's lifting line model. Prandtl's lifting line theory **(69)** derives the lift distribution of a 3-D wing from its geometry. Here, are shortly reported the steps to solve lifting line theory for a fixed wing.

The lift of a wing can be expressed as:

$$L = \int_{-b/2}^{b/2} l(x)dx = \rho V_\infty \int_{-b/2}^{b/2} \Gamma(x)dx \tag{3.16}$$

with $\Gamma(x)$ as the circulation of the wing segment. We suppose that the angle of attack α in this example is the same for every wing airfoil. Figure 3.12 contextualizes the problem:

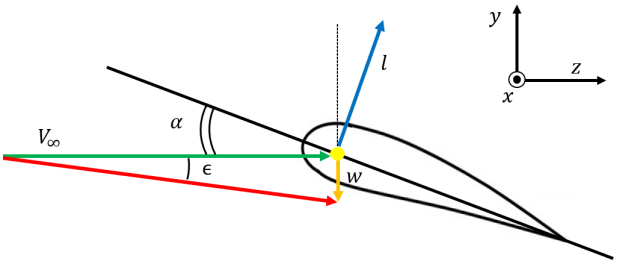

Figure 3.12: Lifting line airfoil schematics

The down-wash velocity $w << V_\infty$ is derived trough Biot-Savart law:

$$w(x) = -\frac{1}{4\pi} \int_{-b/2}^{b/2} \frac{1}{x-x'} \frac{d\Gamma(x')}{dx'} dx' \tag{3.17}$$

From Figure 3.12, supposing that $\epsilon << 1$, is possible to extract the effective angle of attack α_{eff} seen by the airfoil:

$$\alpha_{eff}(x) = \alpha(x) - \epsilon(x) = \alpha(x) + \left(\frac{w(x)}{V_\infty}\right) \tag{3.18}$$

The lift coefficient of thin airfoil theory is expressed as $C_l(x) = 2\pi\alpha_{eff}$, consequently the effective angle of attack α_{eff} can also be written as:

$$\alpha_{eff}(x) = \frac{\Gamma(x)}{\pi c(x) V_\infty} \tag{3.19}$$

with $c(x)$ as the airfoil chord length.

By inserting equation 3.17 in 3.18 and using equation 3.19 we obtain the Prandtl compatibility relation as described below:

$$\Gamma(x) = \pi c(x) V_\infty \left[\alpha(x) - \frac{1}{4\pi V_\infty} \int_{-b/2}^{b/2} \frac{1}{x-x'} \frac{d\Gamma(x')}{dx'} dx'\right] \tag{3.20}$$

Equation 3.20 is solved iteratively, by computing the circulations for every segment of the wings. Once at convergence, the aerodynamic forces acting on each segment are calculated. In ALL reference frame, these forces are written as:

$$d\vec{F}^{i,j} = \rho\Gamma^{i,j}(\vec{U}\times\vec{e}_t)dl^{i,j} \tag{3.21}$$

with i as a wing segment, j as a temporal step, $\vec{U}$ as the vector sum between the airflow speed and the wing kinematic velocity, $\vec{e}_t$ as vector of coordinates $[\vec{e}_x,\vec{e}_y,\vec{e}_z]$ and $dl^{i,j}$ as the length of a wing segment i at a time j.

The forces acting on a segment $d\vec{F}^{i,j}$ are decomposed in:

- Lateral force: $dF_x^{i,j}$ (**x**-axis)
- Lift force: $dF_y^{i,j} = dL^{i,j}$ (**y**-axis)
- Drag force: $dF_z^{i,j} = dD^{i,j}$ (**z**-axis)

We can now compute the mean aerodynamic forces over a flapping cycle:

$$\bar{F} = [\bar{F}_x, \bar{F}_y, \bar{F}_z] = \frac{1}{T}\sum_{j=1}^{m}\sum_{i=1}^{n} d\vec{F}^{i,j} \tag{3.22}$$

Before retrieving the power output P of the ALL model let recall the definition of power. The power is defined as the product of a force on an agent and the velocity of the agent. Generally, the power of a weightless articulated structure can be computed in two ways:

$$P = \vec{\tau}\bullet\vec{w} \tag{3.23}$$

$$P = \vec{F}\bullet\vec{V} \tag{3.24}$$

with $\vec{\tau}$ as the aerodynamic torque and $\vec{w}$ as the kinematic angular velocity.

ALL model does not give us access to the kinematic angular velocity $\vec{w}$, thus we must focus our work on equation 3.24. The force $\vec{F}$ generated by the wings is derived from the lifting line and the speed $\vec{V}$ should be equal to the kinematic velocity $\vec{v}_{kin}$ of the wings.

At first $\vec{V} = \vec{v}_{kin}$ does not seem intuitive, we are more tempted to use $\vec{V} = \vec{U}$. To clarify this point, we can imagine the bird as a static structure (i.e. turbine). The forces $\vec{F}$ generated by the wings increase the speed V_∞ of the fluid but the wings frame remains static. Thus, the wings (i.e. agent) velocity is independent from the speed V_∞ of the fluid.

After this clarification, the aerodynamic power of the White Ibis is expressed in the following formula:

$$P = -\frac{1}{T}\sum_{j=1}^{m}\sum_{i=1}^{n} d\vec{F}^{i,j}\bullet d\vec{v}_{kin}^{i,j} \tag{3.25}$$

The minus sign considers the fact that the wing sees an airflow in the opposite direction of the wing motion.

ALL model is a powerful tool, capable to capture nearly every motion of the flyer. The flapping framework presented at the beginning of this chapter was limited by the models of the wing retraction and folding that did not reproduced perfectly the flight kinematic of the bird.
Here these two motions are easily described by the kinematic of the elbow and wrist the joints.

Figure 3.13 reproduces these motions as seen from the bird skeleton.

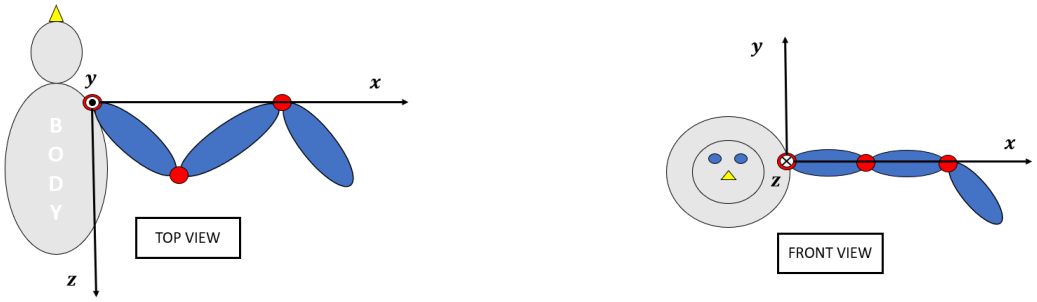

Figure 3.13: Examples of wing retraction (left) and folding (right)

The complexity and modularity of this model opens up new types of research that go far beyond the actual literature.

4 PSO framework

In this chapter the coupling between the ALL model and the selected optimizer is vastly explained. The first part of this chapter arguments the choice of the optimizer, the second part describes the working principles of the optimizer and the last part details how a selected flight kinematic is coupled with the optimizer.

4.1 The Contribution

The idea started from a simple question: how can we retrieve power curves from the ALL model?

Power curves exist only if trim conditions are satisfied. These conditions depend on the flight kinematic and on the flight speed V_∞ of the bird. We could find the trimmed kinematic using the **21** potential kinematic variables λ_{kin} of the ALL model. As a reminder trim conditions for a given flight speed V_∞ are defined as:

$$Lift = Weight \tag{4.1}$$

$$Thrust = Drag \tag{4.2}$$

The ALL model returns lift $\bar{F}_y$ and drag $\bar{F}_z$ as a function of the flight kinematic and flight speed V_∞. We know the thrust T needed to fly at different flight speed and we also have the information on the weight W of the bird therefore, we have all the data to solve the problem through an optimization.

What optimizer should we use? The search space seems to be too wide for a local optimization and the number of variables is astronomically high. Therefore, a global optimizer seems to fit better this problem.

I, first, tried a gradient based global optimizer[20] however, this optimizer did not converge to a trimmed solution and was heavy in term of computational time. The failure of the gradient based optimization might be related to the complex shape of the search space.

Therefore, I opted for an optimization that could potentially work for any type of search space. Based on my knowledge, two choices were possible: a genetic optimization or a particle swarm optimization and I selected the latter.

This optimization can return various solutions, meaning that multiple trimmed kinematic are possible. We should define a criteria to distinguish different trimmed solutions.

In terrestrial locomotion, the gait kinematic of the agent (animal) is often optimized to minimize its power/energy consumption **(70)**. The same approach can be applied for avian flight.

Following this idea, the optimizer has to find the trimmed kinematic that minimizes the bird aerodynamic power for a given flight speed V_∞. Proceeding in this way, we should finally obtain the minimum power curve PC_{min} and the minimum power kinematic of the reference bird. This overall approach is explained in the next section.

4.2 The PSO

The Particle Swarm Optimization (PSO) **(71)** is an evolutionary and stochastic optimization technique that mimics the navigation and foraging of a flock of birds.

In PSO, a swarm of k particles communicate with one another using search directions. The algorithm uses a set of particles that fly over a search space to locate a global optimum. Each particle position $\vec{x}$ is updated, during the PSO iteration, based on its previous experience and the experience of its neighbors. We initialize the PSO by creating a number k of random particles. The PSO search strategy is to update the velocity vector $\vec{v}$ at each iteration t by direct and indirect communication with the other particles:

$$\vec{x}^{t+1}_{k(i)} = \vec{x}^{t}_{k(i)} + \vec{v}^{t}_{k(i)} \tag{4.3}$$

$$\vec{v}^{t+1}_{k(i)} = w\vec{v}^{t}_{k(i)} + c_1 r_1(\vec{p}^{t}_{k(i)} - \vec{x}^{t}_{k(i)}) + c_2 r_2(\vec{g}^{t}_{k(i)} - \vec{x}^{t}_{k(i)}) \tag{4.4}$$

The first element of Equation 4.4 is called inertia component and can be modulated by the inertia factor w. The second element is called cognitive/local component and can be modulated by the local

[20] From the Optimization Python Library: scipy.optimize

acceleration coefficient c_1. The value p indicates the best recorded position of the current particle (local best). Finally the third element is the social/global component where g is the best recorded position of the entire swarm (global best). This component can be modulated by the global coefficient c_2. The value r_1 and r_2 are random vectors having the same length of the vector $\vec{x}$ and ranging from 0 to 1.

When the particles are initialized at $t = 0$, they occupy a position $\vec{x}^0_{k(i)}$ in the search space. The search space is defined by the cost function J that we want to optimize. Therefore at each position of the search space is associated a cost.

The particles at first have no direction to follow. The one with the best cost (i.e. value closer to the optimum we are seeking) is selected as the swarm leader. The leader position $\vec{g}^0_{k(i)}$ (global best) and cost plus all the current particles positions $\vec{p}^0_{k(i)}$ (local bests) and costs are "saved" in the PSO. For futher reference, we are going to call these saved values "swarm characteristics".

This sets the algorithm in motion and gives to the particles a direction to follow. At the next iteration $t = 1$, the particles go toward the leader with a velocity $\vec{v}^1_{k(i)}$ that depends on the previous velocity $\vec{v}^0_{k(i)}$ (i.e =0), the local best position of the current particle $\vec{p}^0_{k(i)}$ and the global best position $\vec{g}^0_{k(i)}$ of the swarm. The intensity of this velocity can be modulated by the different factors described previously (w, $c1$, $c2$).

The vectors $r1$ and $r2$ have a fundamental role because they give to the particles the opportunity to explore the search space and the possibly to find a better position than the current global best $\vec{g}^0_{k(i)}$. Without these factors, the PSO will return, most of the time, the global best obtained during the initialization phase ($t = 0$).
The particles at end of $t = 1$ reach new positions $\vec{x}^1_{k(i)}$ and the swarm characteristics are updated. The iteration goes on till the target value (optimum) is reached. The PSO then returns the best position of the swarm. The diagram in Figure 4.1 depicts what explained above.

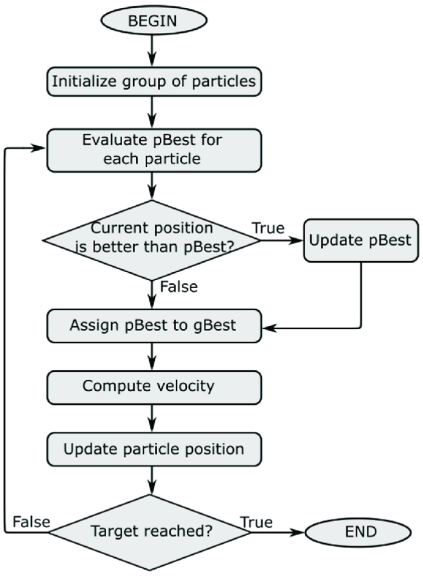

Figure 4.1: Particle Swarm Optimization Algorithm **(72)**

The PSO evolution in a search space is better explained trough a picture than trough words, Figure 4.2 shows the movement of different particles from the initial state to the final state (global minimum of the search space).

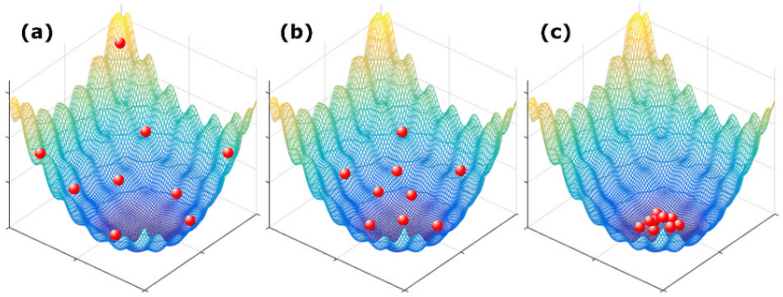

Figure 4.2: PSO progression in the search space **(73)**

It is now time to define the particles and the search space of our PSO.

The PSO model selected for this study is found in the Python package "*pyswarm*" **(74)**. This PSO has three stopping criteria; when the maximum number of iterations t selected is reached or when the new best position found differ from the previous best less than a selected amount k_{pos} or when new best cost differ from the previous best for less than a selected amount k_{cost}.

The position of a particle is given by the wing kinematic λ_{kin}. The wing kinematic is an array of angles describing the ALL joints motions:

$$\lambda_{kin} = [\phi_{0_S}, \phi_{1_S}, \eta_{\phi_S}, \theta_{0_S}, \theta_{1_S}, \eta_{\theta_S}, \psi_{0_S}, \psi_{1_S}, \eta_{\psi_S}, \theta_{0_E}, \theta_{1_E}, \eta_{\theta_E}, ...] \tag{4.5}$$

The position of the particle is related to a cost in the search space. The cost function J describing the search space must consider the aerodynamic power P and the aerodynamic forces (lift and drag) of the flyer. To ensure both power minimization and trim conditions, the following cost function J was used:

$$J(\lambda_{kin}) = P(\lambda_{kin})^2 + \zeta[Trim(\lambda_{kin})] \tag{4.6}$$

with $\zeta = 10^4$ and $Trim$ as:

$$W = mg = \bar{F}_y = L \tag{4.7}$$

$$T = -(D_{par} + D_{pro}) = \bar{F}_z = D \tag{4.8}$$

$$Trim = |T - D| + |L - W| \tag{4.9}$$

In equation 4.8, the parasitic drag is $D_{par} = \frac{1}{2}\rho S_b C_{D_b} V_\infty^2$ (C_{D_b} is obtained section in 5.1, Equation 5.5) and the profile drag is $D_{pro} = \frac{1}{2}\rho S C_{D_{pro}} V_\infty^2$ ($C_{D_{pro}} = 0.03$, $S = 0.179\ m^2$).

The factor ζ in Equation 4.6 has the role to penalize the particles that do not satisfy trim conditions. The cost function J simultaneously looks for the minimum power curve and for a trimmed flight. A solution is accepted if $Trim < 0.01$.

The Figures 4.3 and 4.4 depict the overall structure of the optimization problem for a given flight speed V_∞:

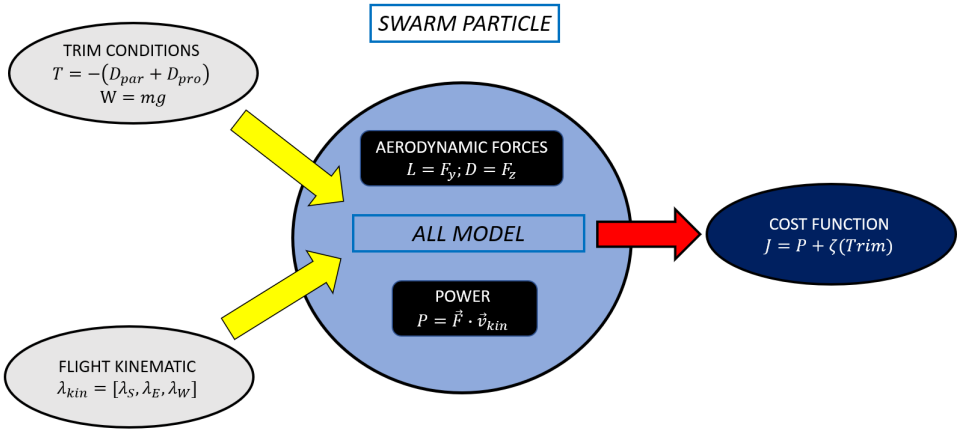

Figure 4.3: Particle schematic

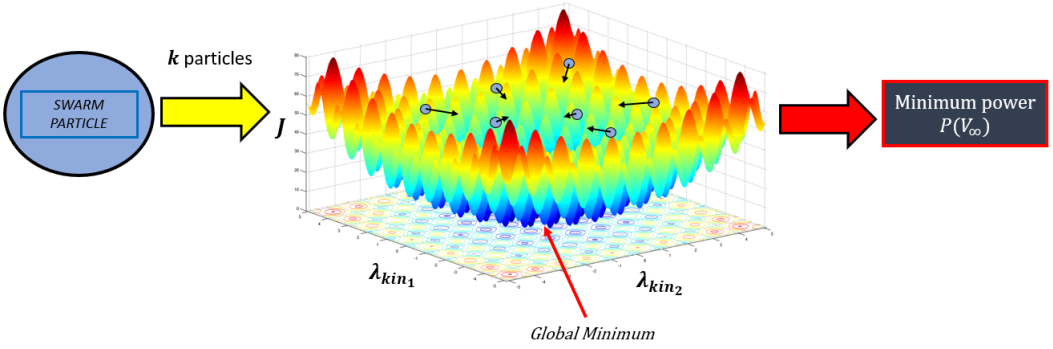

Figure 4.4: Example of 3D search space (Rastrigin's function **(75)**)

This complete the PSO framework description. The Rastrigin's cost function displayed in Figure 4.4 is not chosen by chance. Section 5.2 will demonstrate qualitatively that the search space of the ALL model has a similar shape to the Rastrigin's function.

The particularity of the Rastrigin's function search space is that positions distant from each other may have similar cost value. Consequently, finding the global minimum ($res = [0, 0]$) of this search space is a tough task.

It is important to highlight that the profile drag D_{pro} could be retrieved using the ALL model. Each segment of the wing experiences a local airflow speed $\vec{V}_{loc}(\lambda_{kin})$ consequently, the local profile drag $\vec{D}_{pro_{loc}}(\lambda_{kin})$ is different for every wing segment. The profile drag is thus related to the flight kinematic of the bird and is derived for each particle. This model is more realistic than the previous one and is a novel way of evaluating profile drag.

The present approach is a suggestion for future analysis but it is not used in this thesis. Nonetheless, we are going to show the steps to define this new model:

$$\vec{D}^{i,j}_{pro_{loc}} = \frac{1}{2}\rho c^{i,j} C_{D_{pro}} (\vec{V}^{i,j}_{loc})^2 \, dl \, dt \tag{4.10}$$

$$\vec{D}_{pro} = [D_{pro_x}\,; D_{pro_y}\,; D_{pro_z}] = \frac{1}{T}\sum_{j=1}^{m}\sum_{i=1}^{n} \vec{D}^{i,j}_{pro_{loc}} \tag{4.11}$$

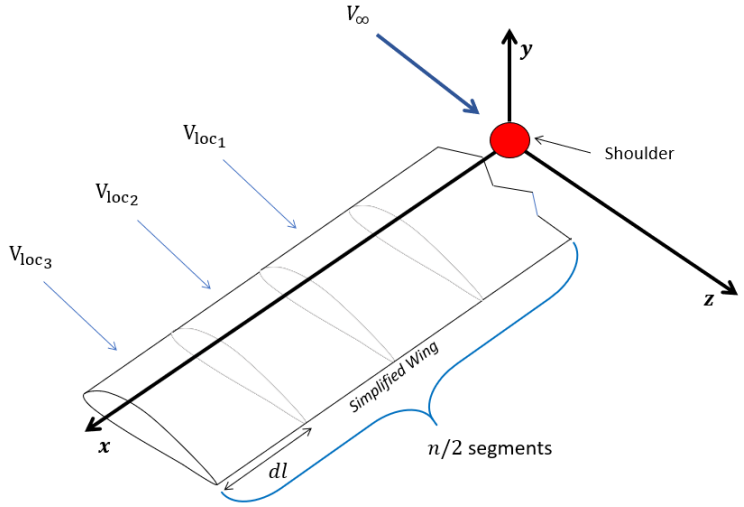

Figure 4.5: Local speed visualization

Dividing the profile drag in its tree components lead to the following trim conditions:

$$W = mg + D_{pro_y} = \bar{F}_y = L \tag{4.12}$$

$$T = -(D_{par}+D_{pro_z}) = \bar{F}_z = D \tag{4.13}$$

$$Lat = -D_{pro_x} = \bar{F}_x \tag{4.14}$$

$$Trim = |T-D|+|L-W|+|Lat-\bar{F}_x| \tag{4.15}$$

With this last contribution we conclude this section. The next section describes the selected reference flight kinematic and how it is coupled with the PSO.

4.3 Reference kinematic

Describing the exact flight kinematic of ibises is out of the scope of this work. To present a plausible flight kinematic for our reference bird we can take inspiration from the study of Tobalske **(13)** on pigeon flight kinematic.

Part of his research was already shown in Figure 2.4 (later view), here Figure 4.6 depicts the pigeon flight kinematic from a dorsal prospective. Similarly to Figure 2.4, Figure 4.6 highlights the wingtips and wrist paths of the bird.

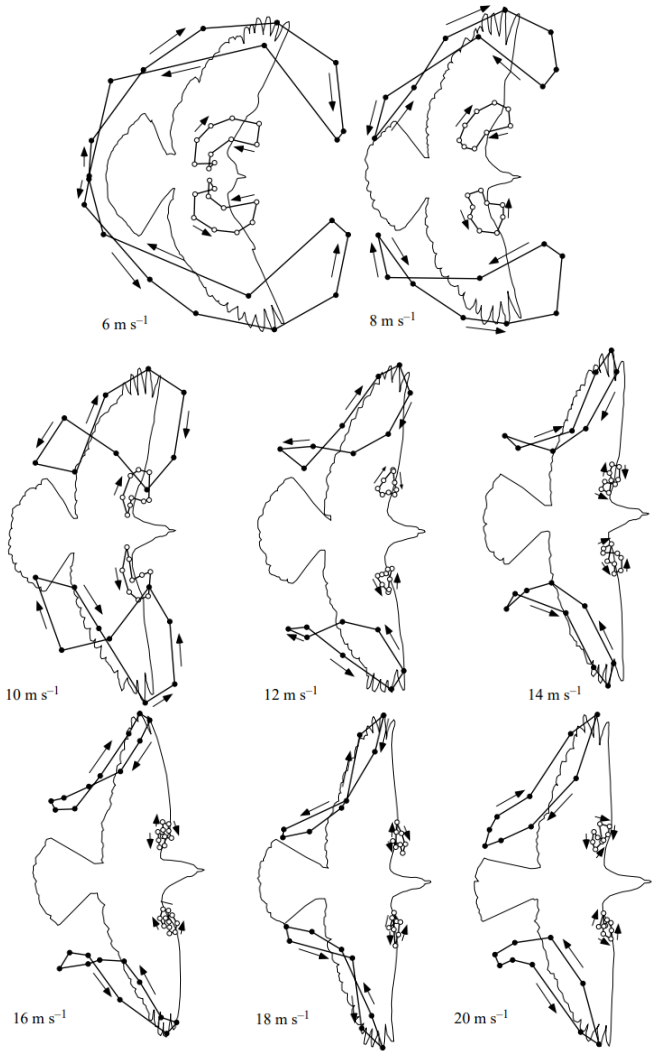

Figure 4.6: Dorsal view of a pigeon flight kinematic in steady-speed flight conditions **(13)**

By rescaling these results to our reference bird, we derive, using the ALL model, a flight kinematic that can match ibises flight. This kinematic scenario will be named **Reference** case and is reported in Table 5 and depicted in the subsequent figures:

Joint	α_0 [°]	α_1 [°]	η [°]
Shoulder x	free	0.8	−90
Shoulder y	−19	20	90
Shoulder z	0	free	180
Elbow x	0	−30	90
Elbow y	30	30	−90
Wrist y	−30	30	−90
Wrist z	0	0	0

Table 5: Flight kinematic: **Reference** case

Shoulder:

The flapping amplitude ϕ_{1_S} and the pitching offset are θ_{0_S} are not imposed in this scenario. These two kinematic parameters can be considered as the variables of our optimization problem. The phase angle η_{ϕ_S} ensures that the flapping cycle starts at mid-downstroke. The value of the phase angle η_{θ_S} is selected to ensure that minimum pitching angle occurs when the plunging velocity reaches its maximum. The phase angle η_{θ_S} ensures that the maximum sweeping angle occurs in accordance with the maximum plunging velocity.

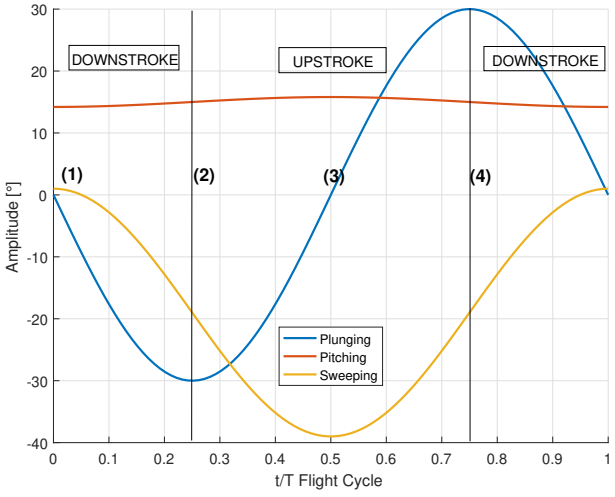

Figure 4.7: Shoulder kinematics ($\phi_{1_S} = 30°$, $\theta_{0_S} = 15°$)

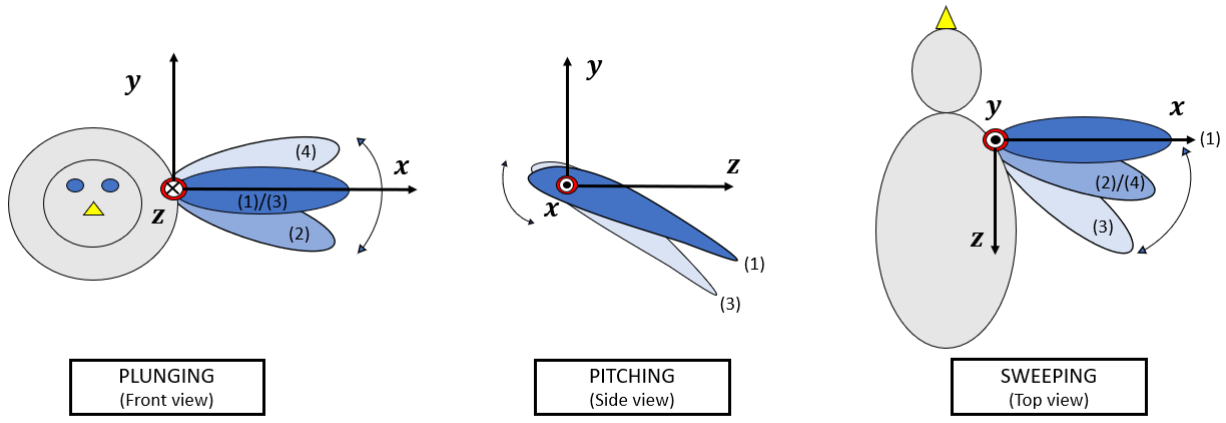

Figure 4.8: Shoulder kinematic Visualization

Elbow:

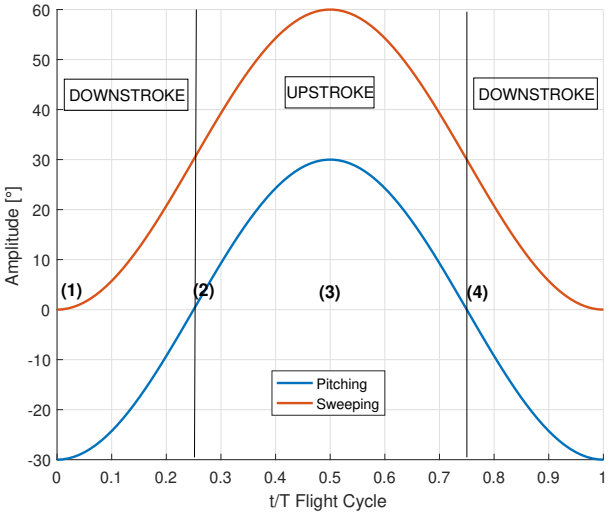

Figure 4.9: Elbow kinematic

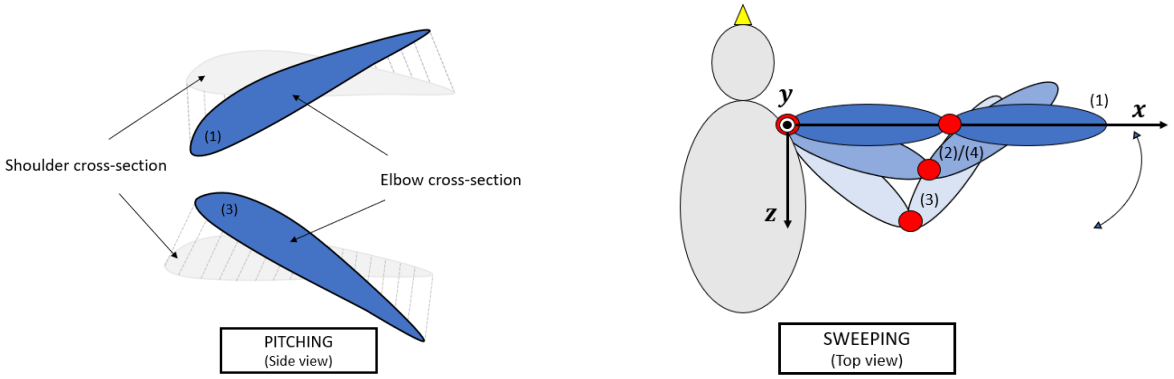

Figure 4.10: Elbow kinematic visualization

Wrist:

In this scenario the wrist plunging motion is set to zero, thus no wing folding motion is specified (see Figure 3.13). A plausible wrist plunging motion is represented in Figure 4.12. However, wrist plunging motion will not be studied in this thesis.

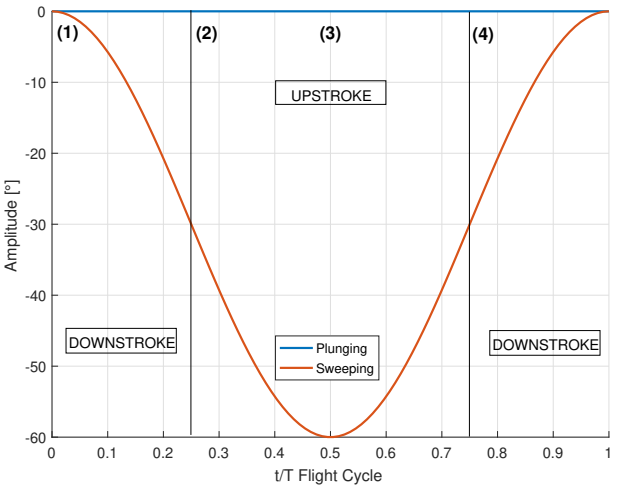

Figure 4.11: Wrist kinematic

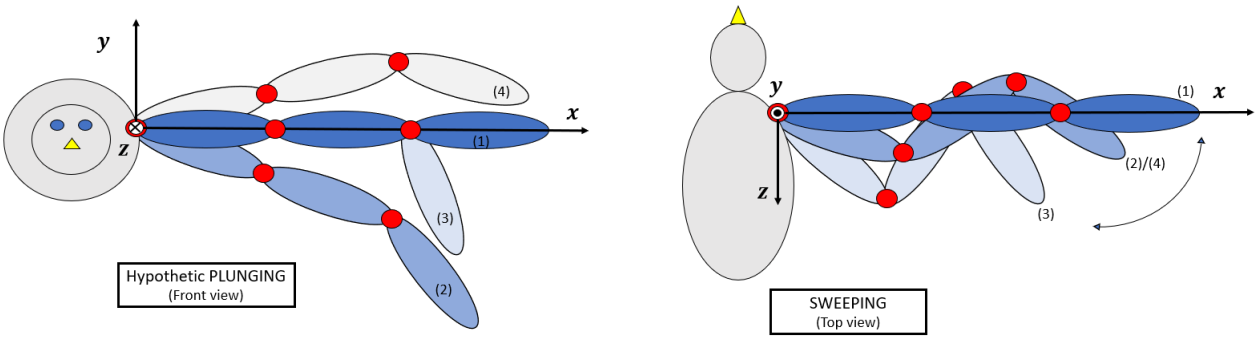

Figure 4.12: Elbow kinematic visualization

The PSO framework is first applied on the two free variables ϕ_{1_S} and θ_{0_S} of the problem. Then subsequently, the 5 shoulder kinematic parameters are freed.

The inputs of the PSO model are listed here below. Generally, to return optimal results, a high number of particles k is requested. This value was reduced in order to obtain acceptable solutions in a reasonable amount of time. Clerc and Kennedy **(71)** proposed suitable PSO coefficients ($w = 1$, $c1 = c2 = 2.05$) for a vast majority of problem but these coefficients did not work out in this context perhaps due to the low number of particles k.

The optimizer needs obviously to be improved. A dedicated research should be conducted to achieve better performances. The basic PSO tool, proposed in this thesis, must be seen as a starting point for future improvements.

PSO model:

- Number of particles:

$$k = \begin{cases} 50 & \text{for } \lambda_{kin}(2) \\ 100 & \text{for } \lambda_{kin}(> 5) \end{cases} \tag{4.16}$$

- Coefficients: $w = c1 = c2 = 0.5$
- Number of iteration: $t = 50$
- Minimum change in position: $k_{pos} = 0.05$
- Minimum change in cost: $k_{cost} = 0.1$

Finally, for the optimization, the ALL wings were discretized spatially in $n = 16$ segments and temporally in $m = 20$ steps.

The PSO and the ALL model are now coupled. In the next chapter, the White Ibis flight kinematic is optimized and the evolution of its kinematic parameters is discussed. Due to a lack of literature support, most of the results obtained are commented in a speculative manner.

5 Results

This chapter addresses the main question of this thesis: trace out the power curves for large migratory birds.

We start this analysis adopting current methods found in literature and described in chapter 2.4. The principal goal of the first section of this chapter is to present a straight and easy way of computing a power curve.

The power curves obtained here are perhaps not ideal, however, they give a good indication on the flight proprieties of a selected bird of mass m.

These models are used as benchmark to validate the results of the ALL power curves. In addition, the limitations of each of the existing models is commented and possible variations are suggested.

In the second section of this chapter, a parametric study is conducted on the ALL/PSO coupling. Power curves are derived from the model and compared to Lund numerical method results (i.e. AFPT **(33)**).

Finally, the thesis suggests ways to improve the current coupled model (i.e. ALL/PSO).

5.1 Literature Power Curves

The reference bird, of this thesis, is a White ibis. The White Ibis has approximately a mass of $m = 1.2$ kg. The allometric results of section 2.2 for this type of bird are reported in Table 6 hereafter.

$\boldsymbol{b}$ (m)	1.252	$\boldsymbol{S}$ (m^2)	0.180
$\boldsymbol{S_b}$ (m^2)	$9.18{\cdot}10^{-3}$	$\boldsymbol{Fr_t}$ ($-$)	6.25
$\boldsymbol{f_{ref}}$ (Hz)	4.44	$\boldsymbol{V_{mp}}$ (m/s)	9.307
$\boldsymbol{P_{mp}}$ (W)	13.54	$\boldsymbol{V_{mc}}$ (m/s)	16.28
$\boldsymbol{COT_{min}}$ ($-$)	0.1043	$\boldsymbol{P_{mc}}$ (W)	18.53
$\boldsymbol{\phi_{ref}}$ ($^\circ$)	31.79	$\boldsymbol{P_{max_A}}$ (W)	20.676

Table 6: White Ibis Characteristics: $\boldsymbol{m} = 1.2$ [kg]

The points of interest (i.e. V_{mp}, V_{mc}, P_{mp}, P_{mc}) of Table 6 are used as reference values and they are compared to each of the model presented in this chapter. The flight speed V_∞ range studied for each one these models is [0−20] m/s.

The first power curve model analysed is the one of Pennycuick **(28)** that we name **Model 1**:

$$P_{ind} = W v_{if} \tag{5.1}$$

$$P_{pro} = \frac{1}{2}\rho S C_{D_{pro}} V^3 \tag{5.2}$$

$$P_{par} = \frac{1}{2}\rho S_b C_{D_b} V^3 \tag{5.3}$$

$$P_{tot_1} = P_{ind}+P_{pro}+P_{par} \tag{5.4}$$

with $C_{D_{pro}} = 0.03$ and $C_{D_b} = 0.2$.

P.I.	Allometric	Model 1
V_{mp}	9.327	7.475
V_{mc}	16.28	9.90
P_{mp}	13.54	7.794
P_{mc}	18.53	8.848
COT_{min}	0.1043	0.0759

Table 7: **Model 1**: Points of Interest

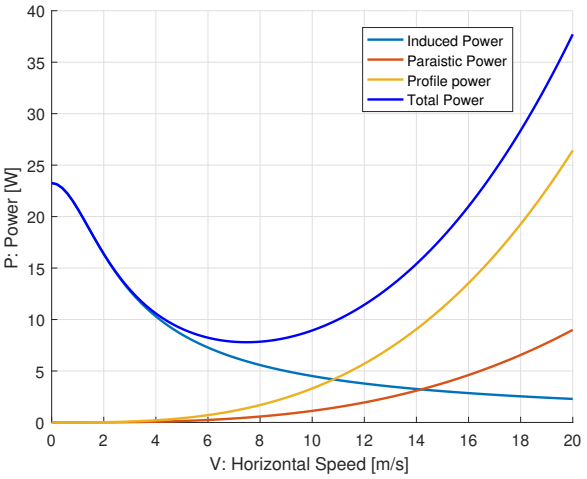

Figure 5.1: **Model 1**: Power Curve

In Table 5.1, the points of interest of **Model 1** are reported and put together with the allometric results of Table 6.

The power output P_{tot_1} is quite low compared to the value obtained by the numerical model (AFPT) of Lund University (Figure 2.23). This is linked directly to the nature of the model. In fact, the actuator disk strongly underestimates bird aerodynamic power.

Since the White Ibis is a migratory bird, we are more interested in finding the position of the minimum COT than the rest of the power curve.

Therefore, our analysis will be particularly focused on the right side of the power curve. This part is more affected by the parasitic P_{par} and the profile drag P_{pro} than by the induced power P_{ind}. It would be interesting to see how the points of interested change in function of these two contributions.

The only true variables of **Model 1** are $C_{D_{pro}}$ and C_{D_b}; tuning these two parameters affect parasitic and profile drag. For this purpose, two variations of the **Model 1** are studied. These variations are plausible and reflect the incertitude, in literature, around these two drag coefficients.

- **Varition 1**: $C_{D_{pro}} = 0.02$ & $C_{D_b} = 0.1$
- **Varition 2**: $C_{D_{pro}} = 0.04$ & $C_{D_{par}} = 0.3$

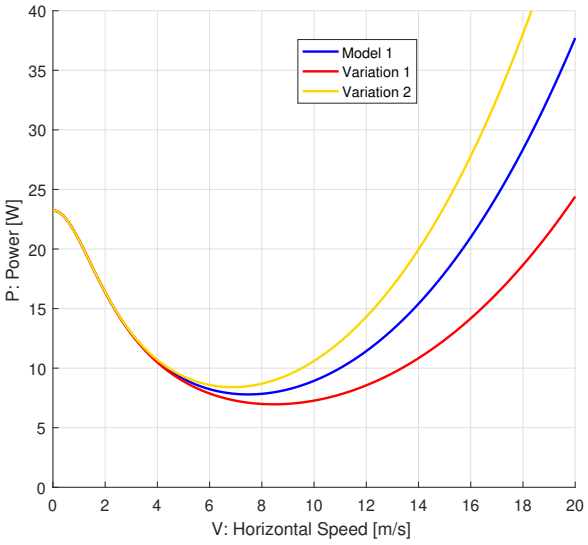

Figure 5.2: Power Curve Comparison

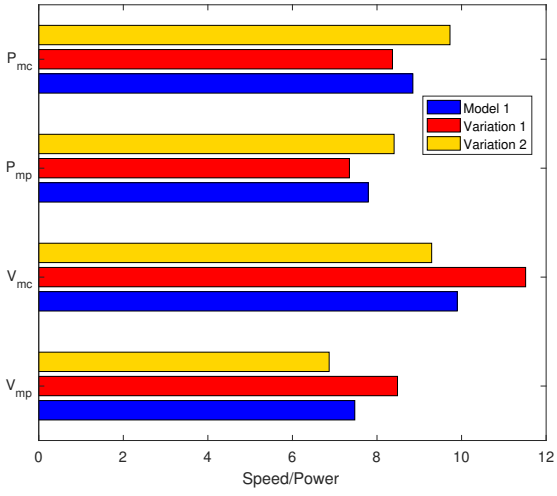

Figure 5.3: P.I. Comparison

As expected only the right part of the curves is affected by these variations. Lowering the value of $C_{D_{pro}}$ and C_{D_b} leads to lower P_{mp} and P_{mc} and to higher V_{mp} and V_{mc}. Of course, the opposite occurs

when $C_{D_{pro}}$ and C_{D_b} increase. This example points out the variability and uncertainty of this simplistic model. Therefore, the results have always to be evaluated considering the order of magnitude and not on their specificity.

5.1.1 Parasitic/Profile drag modification

As stipulated in section 2.3 and reported in section 8.1, the body drag coefficient C_{D_b} varies with respect to the incoming airflow V_∞. The bird changes its trunk shape in order to diminish its impact on the flow thus reducing parasitic drag.

Maybury, in his thesis **(21)**, derived an explicit formula describing the evolution of C_{D_b} with respect to the airflow speed and to the bird morphology. This formula is inserted in **Model 1**:

$$C_{D_b} = 66.6m^{-0.511}FR_t^{0.915}S_b^{1.063}Re^{-0.197} \tag{5.5}$$

Similarly, the profile drag coefficient $C_{D_{pro}}$ evolves as a function of the airflow V_∞. The article **(60)**, described in section 8.2, studies the profile drag coefficient $C_{D_{pro}}$ of a jackdaw during gliding flight. The trend of this parameter is shown to be parabolic with a minimum in accordance with the minimum power speed V_{mp} of the flyer. The $C_{D_{pro}}$ data of the jackdaw is extrapolated and arranged around the minimum power speed V_{mp} of our reference bird.

The value of V_{mp} is taken from the results of the AFPT. The extrapolated data is valid in the speed range between 6 m/s and 20 m/s but can be used at lower speed without having a noticeable impact on the final results.

Of course, the profile drag coefficient $C_{D_{pro}}$, which is different for every flyer, is a mere approximation. We are trying, here, to understand the impact of its parabolic trend on the power curve.

$$C_{D_{pro}} = \frac{0.0262V_\infty^2 - 0.6459V_\infty + 5.3873}{100} \tag{5.6}$$

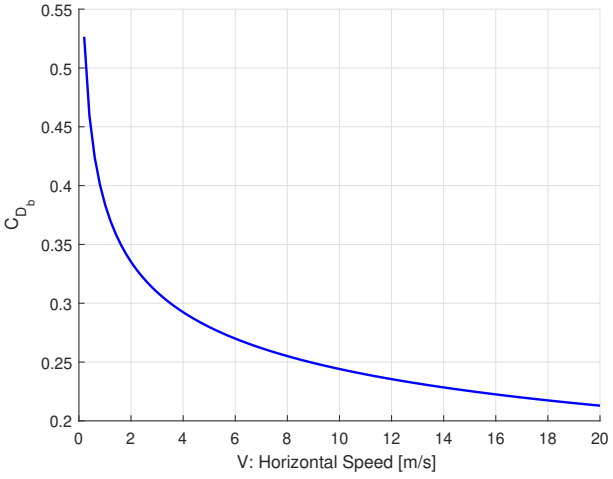

Figure 5.4: C_{D_b}: Body drag coefficient

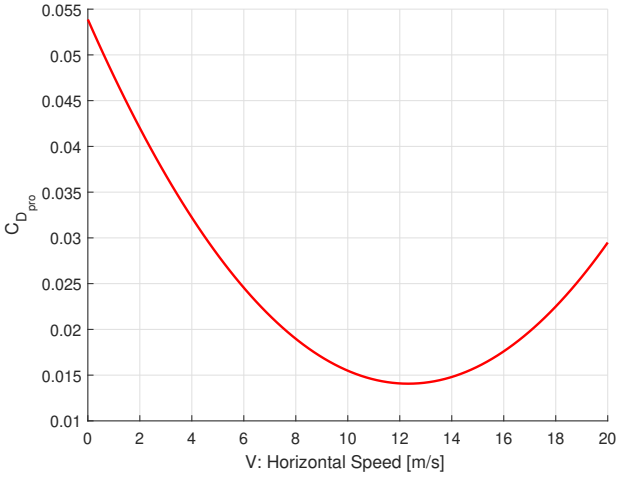

Figure 5.5: $C_{D_{pro}}$: Profile drag coefficient

Before adding these new features to **Model 1**, we correct the induced power P_{ind}, as done by Pennycuick, by multiplying the actuator disk with a compensating factor $k = 1.2$. This new model is named **Model 2**. Here below we compare **Model 1** to **Model 2**:

P.I.	Allometric	Model 1	Model 2
V_{mp}	9.327	7.475	9.09
V_{mc}	16.28	9.90	11.912
P_{mp}	13.54	7.794	8.37
P_{mc}	18.53	8.848	9.44
COT_{min}	0.1043	0.0759	0.0673

Table 8: **Model 2**: Points of Interest

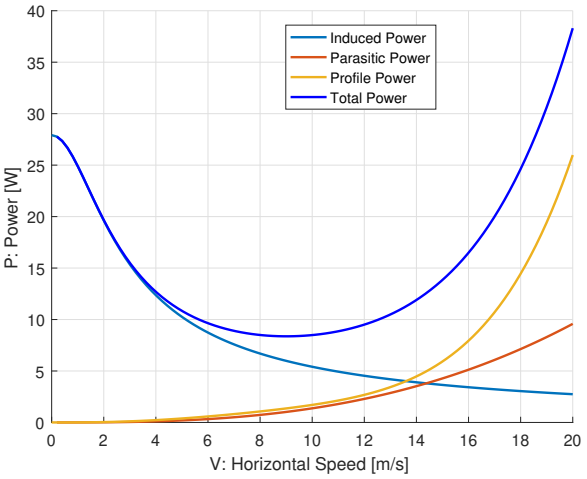

Figure 5.6: **Model 2**: Power Curve

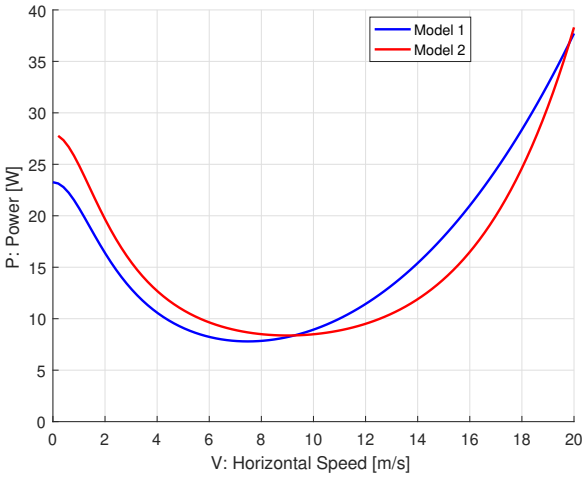

Figure 5.7: **Model 1** and **Model 2** Comparison

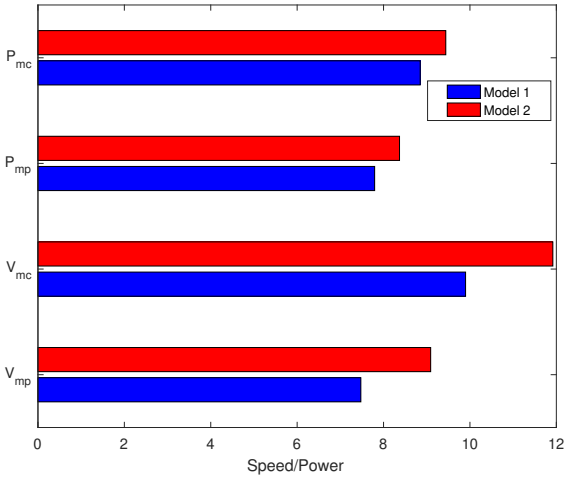

Figure 5.8: P.I. Comparison

The new parasitic power contribution does not affect considerably the power curve, on the other hand the new profile power has a strong impact on the position of V_{mc}. The reduction of $C_{D_{pro}}$ around the minimum speed V_{mp}, prevents an early increase of the profile power, thus the minimal cost of transport of the curve is displaced.

The power output P_{tot_2} of **Model 2** is still low compared to the allometric results. This means that the compensating factor k is underestimated for this model. This factor is often incorrect **(33)** and must be tuned depending on the flyer studied. The compensating factor that would fit best our model, based on the allometric power results, is set between 1.9−2.5.

5.1.2 Rayner Model Analysis

A proper analysis of Rayner's power curve model (Part 2 **(42)**) is conducted in this subsection. The model takes as input the flapping amplitude ϕ, the flapping frequency f and the downstroke ratio τ. The impact of the kinematic flight parameters on the power curve is studied. The stroke-plane angle γ is an output of the model but it is not considerably affected by input variations.

We start the analysis with the following inputs (**Model 3**):

- Flapping amplitude[21]: $\phi = 60°$
- Flapping frequency: $f_{ref} = 4.44$ [Hz]
- Downstroke ratio: $\tau = \frac{1}{2}$

[21] Value used in Rayner's work.

- Maximal body angle: $\beta_1 = 80°$

The power curve is limited on the left side to a speed of 3 [m/s]. We set this limitation because Rayner's part 2 model is not suitable for very low speed. **Model 3** is depicted in Figure 5.9.

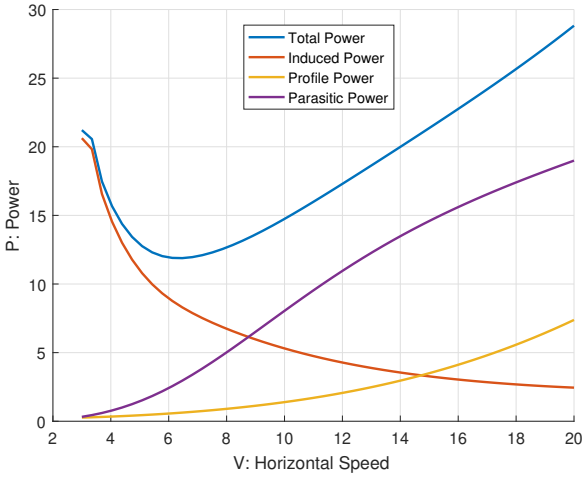

Figure 5.9: **Model 3**: Power Curve

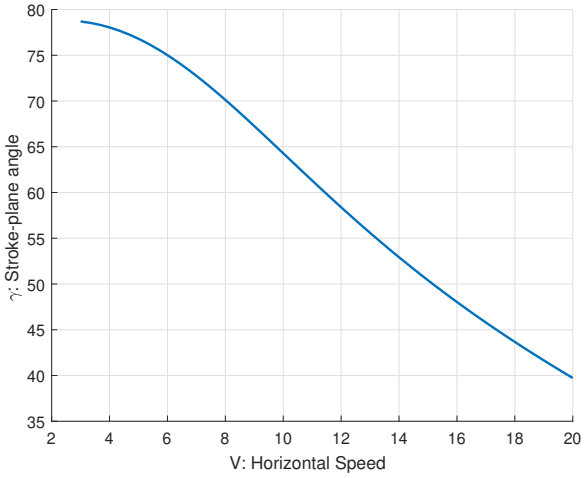

Figure 5.10: Model Stroke-plane angle γ

P.I.	**Allometric**	**Model 2**	**Model 3**
V_{mp}	9.33	9.09	6.122
V_{mc}	16.28	11.912	10.98
P_{mp}	13.54	8.37	11.58
P_{mc}	18.53	9.44	17.09
COT_{min}	0.1043	0.0673	0.1322

Table 9: **Model 3**: Points of Interest

This model returns good estimations in term of aerodynamic power, but poor results in term of flight speed.

The important presence of the parasitic power dramatically affects the trend of this power curves. Compared to **Model 2** the power drag is two to three times higher.

In **Model 3** V_{mp} and V_{mc} are far apart from each other when compared to **Model 2** and this leads to a wider optimal flight zone[22] between these two speeds.

The stroke-plane angle γ follows the expected trend. Although, when put aside with results of section 2.3, we clearly see that Rayner's model overestimates the value of γ.

Rayner's model shows the impact of the parasitic drag at low speed. This contribution seems to be too important but captures a natural behaviour of flyers. Perhaps, applying a correction to the value of γ could lower the parasitic contribution. Although, correcting this value would violate the trim conditions of the model.

Rayner's power curves are quite atypical when compared with previous models. In particular, the right side of the curve is unusually linear. This leads to a strong uncertainty on the location of the COT_{min} point of interest. Indeed, this point of interest is strongly affected by any change of the model inputs. The next analysis will assert this point.

The following parametric analysis is conducted on Rayner's power curve:

- Flapping amplitude variation ($f = 4.44$ [Hz], $\tau = 1/2$): $\phi = [45° ; 60° ; 75°]$
- Downstroke ratio variation ($\phi = 60°$, $f = 4.44$ [Hz]): $\tau = [3/7 ; 1/2 ; 4/7]$
- Flapping frequency variation ($\phi = 60°$, $\tau = 1/2$): $f = [4/5 f_{ref} ; f_{ref} ; 6/5 f_{ref}]$

[22] Zone were the cost of transport is roughly identical to COT_{min}

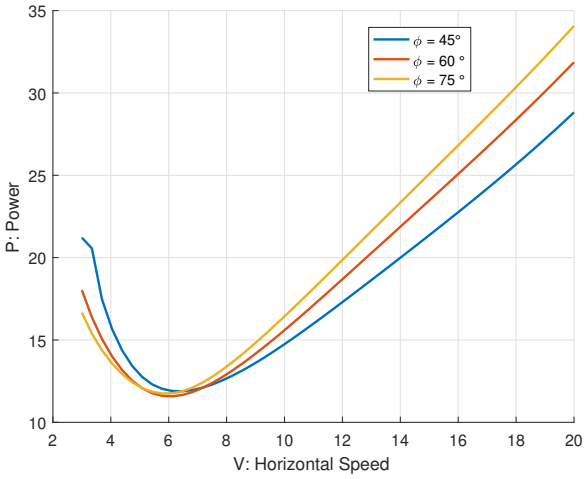

Figure 5.11: Flapping Amplitude ϕ Comparison

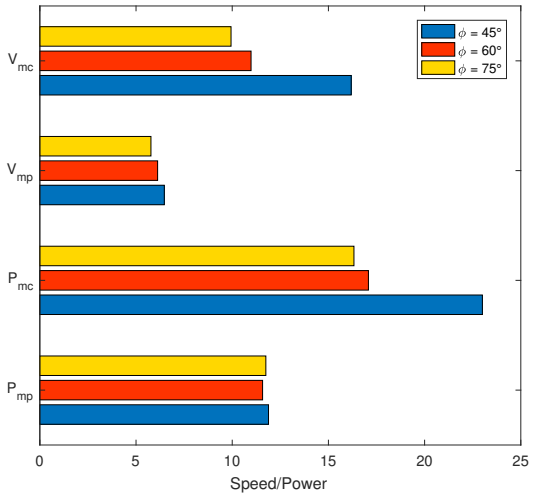

Figure 5.12: P.I. Comparison

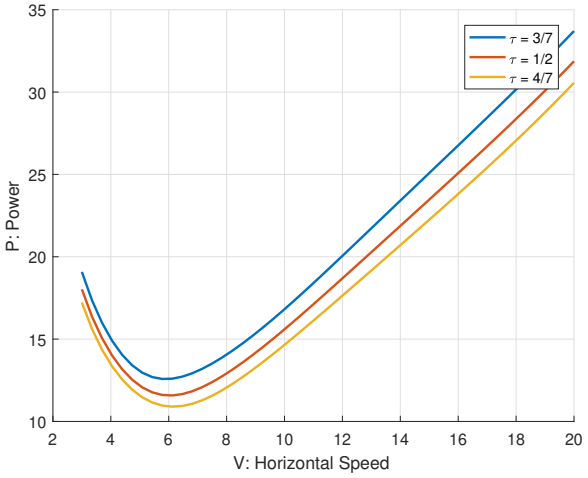

Figure 5.13: Downstroke ratio τ Comparison

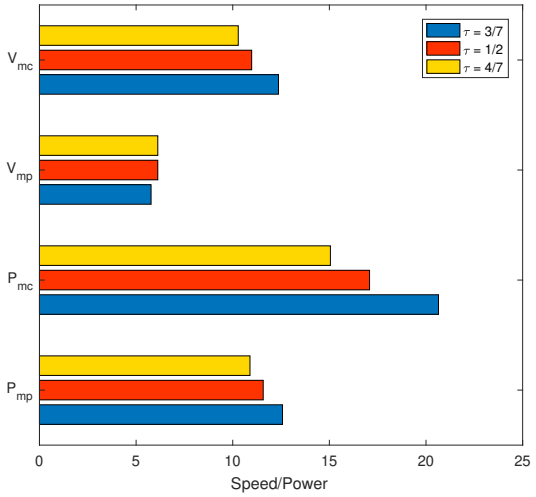

Figure 5.14: P.I. Comparison

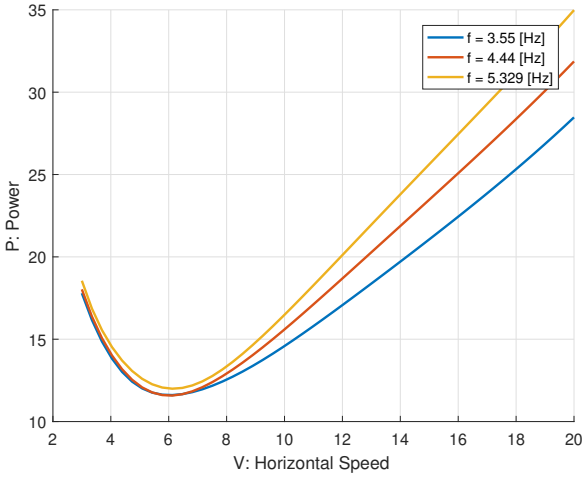

Figure 5.15: Flapping frequency f Comparison

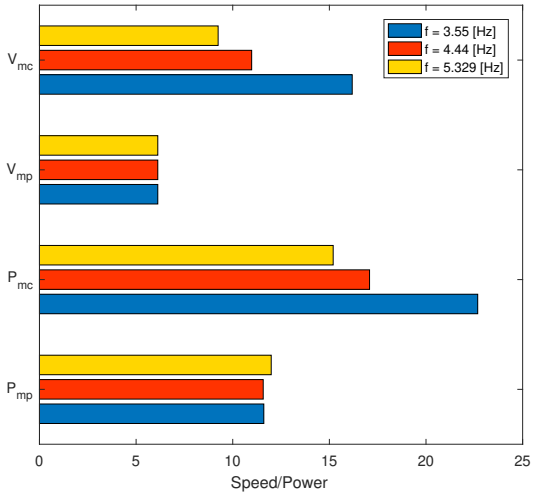

Figure 5.16: P.I. Comparison

In Rayner's model only the induced P_{ind} and the profile P_{pro} power are affected directly by the variations of the input parameters. The parasitic power P_{par} is strictly related to the stroke-plane γ output, thus indirectly affected by input variations. The variation of γ with respect to the model inputs is negligible.

The first parameter studied is the flapping amplitude ϕ. Decreasing this parameter increases the induced power and decreases the profile power. This can be explained by the following statements.

The size of the rings generated by the bird is directly proportional to the flapping amplitude ϕ. Therefore, more rings are needed to support the bird weight leading to a consistent augmentation of the induced power.

Profile power, in Rayner's formulation, is directly proportional to the flapping amplitude ϕ. Intuitively, when the flapping motion is closer to gliding flight conditions ($\phi = 0°$, $f = 0$) less air resistance is experienced by the wing.

The second parameter studied is the downstroke ratio τ. Decreasing this parameter increases the induced power. The downstroke is shorter, thus the energy imparted to the rings is smaller. A higher rings production is then needed to support the bird weight. The impact on the profile power is negligible in this case.

The last parameter analysed is the flapping frequency f. The induced power is not considerably affected by this parameter. On the other hand, profile power variations are strongly related to this parameter. Decreasing f leads to a lower profile power. Again, similarly to the flapping amplitude ϕ, when f is reduced the flapping motion get closer to gliding flight conditions ($\phi = 0°$, $f = 0$) reducing profile power.

As stated previously and shown in the figures above, the location of V_{mc} is strongly affect by input variations.

5.1.3 Compensating factor Model

As discussed previously, it is important to have a good estimate for the compensating factor k.

This factor is selected in order to achieve the best approximate of the induced power P_{ind}. In this chapter we assume that Rayner's discrete actuator disk model (Part 1 **(41)**) can be applied in forward flight. Consequently, we assume that the vortex rings generated by the bird, even in forward flight, are aligned along the same axis and are superposed one over the others[23] (Figure 5.17).

This is a strong assumption; two vortex rings are distant from each other in forward flight, the superposition of two rings rarely occurs.

The only possible way to respect this hypothesis is to consider the bird as a static structure, similar to a turbine. This is the approach that we will use in this section.

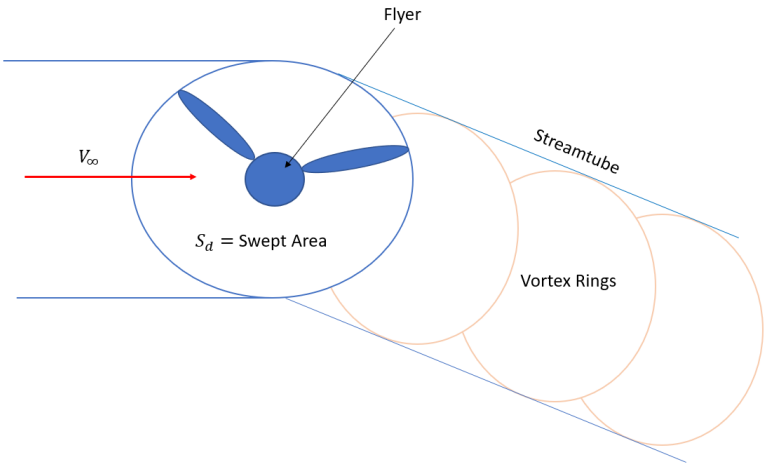

Figure 5.17: Discrete actuator disk in forward flight

This approach has to be considered as a helpful tool to rapidly estimate the aerodynamic power of a bird and in no case as a model reflecting the physic of avian flight. The compensating/correction

[23] Of course in reality the vortex rings of the image do not have the same radius of the stream tube

factor $k(=\sigma)$ of Rayner's part 1 model was given by the following formula:

$$k = \sigma = \frac{0.95}{R'} + \frac{1.2}{R'^5} f_p \tag{5.7}$$

The vortex ring size reduction factor R' depends on the wing chord c and on the flapping amplitude ϕ. The feathering parameter f_p is related to the swept area S_d an to flapping frequency f. Therefore, the compensating factor σ can be written as a function of two flight kinematic parameters (ϕ,f). The induced power P_{ind} of this new model is then given by:

$$P_{ind} = \sigma(\phi, f) P_{ind_1} \tag{5.8}$$

Here the flapping frequency f is considered as constant. Even though the experimental data of Pennycuick in section 2.3 shows a cubic trend, the flapping frequency f always sits around pigeon reference frequency $f_{ref} = 5.8$ [Hz].

The flapping amplitude ϕ is first studied through a constant value and afterward through the results of Lund numerical method (i.e. AFPT).

The model of this section, named **Model 4**, takes as inputs the following kinematic parameters:

- Flapping amplitude[24]: $\phi = 45°$
- Flapping frequency: $f_{ref} = 4.44$ [Hz]

The parasitic and profile power P_{par} and P_{pro} of **Model 4** are the same of **Model 2**.

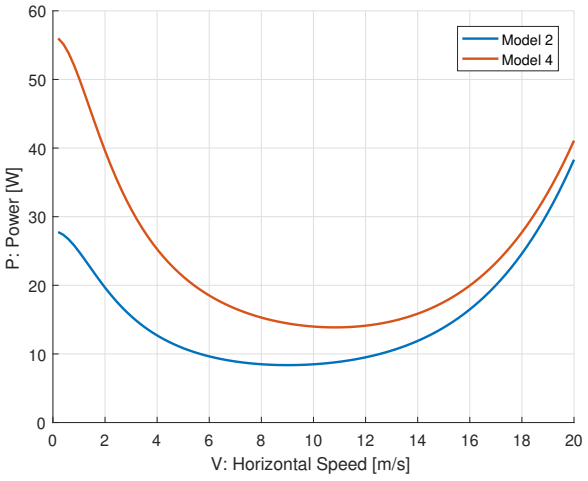

Figure 5.18: **Model 2** and **Model 4** Comparison

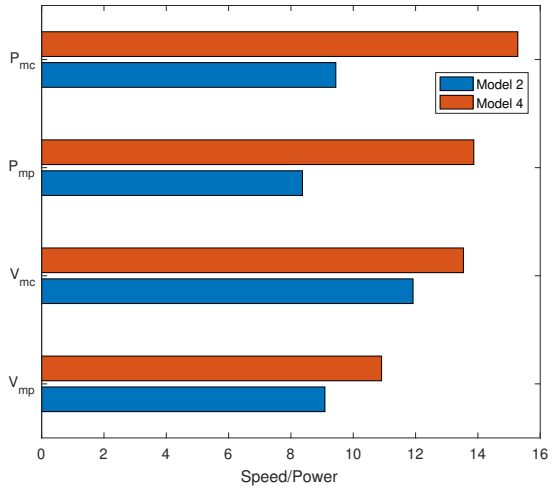

Figure 5.19: P.I. Comparison

P.I.	Allometric	Lund Results	Model 2	Model 4
V_{mp}	9.33	12.03	9.09	10.90
V_{mc}	16.28	16.024	11.912	13.53
P_{mp}	13.54	12.84	8.37	13.87
P_{mc}	18.53	14.93	9.44	15.281
COT_{min}	0.1043	0.0774	0.0673	0.0959

Table 10: **Model 4**: Points of Interest

With the selected parameters, the compensating factor σ is equal to 2.42 [-]. **Model 4** returns good estimates of both power and speed and shares some similarity with both allometric and AFPT results. Before introducing in **Model 4** the flapping amplitude $\phi(V)$ results of AFPT, we are going to conduct a parametric study of the present model:

[24]Estimated mean flapping amplitude ϕ, for the White Ibis, over a wide range of flight speed

- Flapping amplitude: $\phi = [30°, 45°, 60°]$
- Flapping frequency: $f = [4/5 f_{ref}\,; f_{ref}\,; 6/5 f_{ref}]$

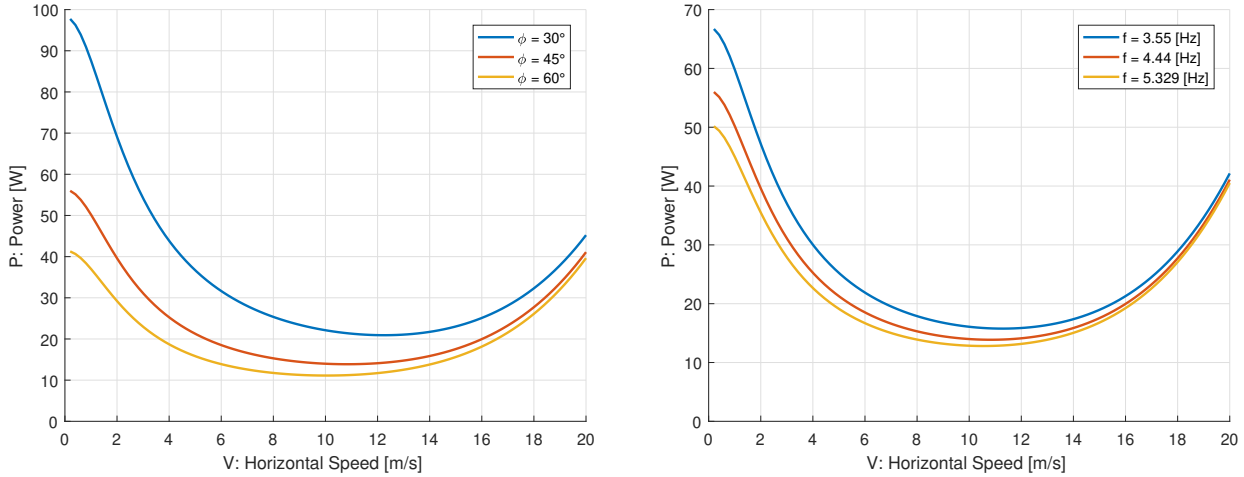

Figure 5.20: Flapping Amplitude ϕ and Frequency f Comparison

These two graphs show that the compensating factor σ is inversely proportional to both the frequency f and the flapping amplitude ϕ.

The flapping amplitude ϕ is directly proportional to the vortex size reduction factor $R^{'}$. Increasing $R^{'}$ leads to the production of wider vortex rings, thus to a larger stream tube. Consequently the apparent induced velocity of the tube is reduced. These changes are reflected through the value of σ, inversely proportional to $R^{'}$. The flapping frequency f has an impact on the rate of vortex rings production. If more rings are generated a more consistent discretized stream tube is created therefore, the model gets closer to the ideal stream tube.

The flapping amplitude $\phi(V)$ of the AFPT is valid as long as the stroke-plane angle $\gamma \leq 50°$. This condition is not valid for speed lower than the minimum flight speed $V_{min} = 5.668$ m/s. Since we are not interested in the left part of the power curve, we can interpolate the results of AFPT and find an approximated value of ϕ for all the speed range.

We then inject the interpolated $\phi(V)$ into the formula of σ and compute this new model (**Model 5**). In addition, following Lund analysis, the profile drag coefficient $C_{D_{pro}}$ of **Model 5** is given by Blasius'flat plate boundary layer solution **(55)**.

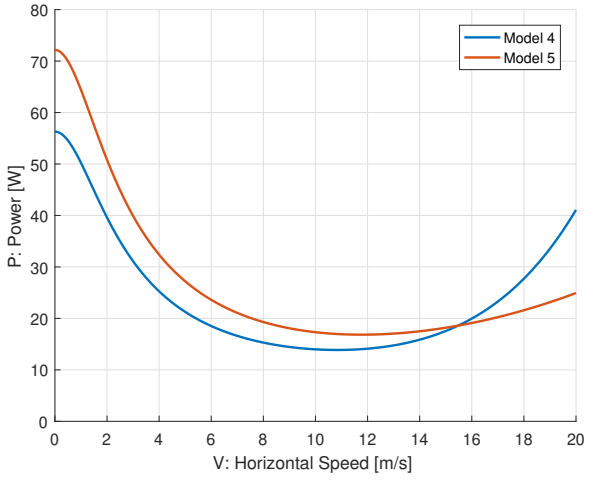

Figure 5.21: **Model 2** and **Model 4** Comparison

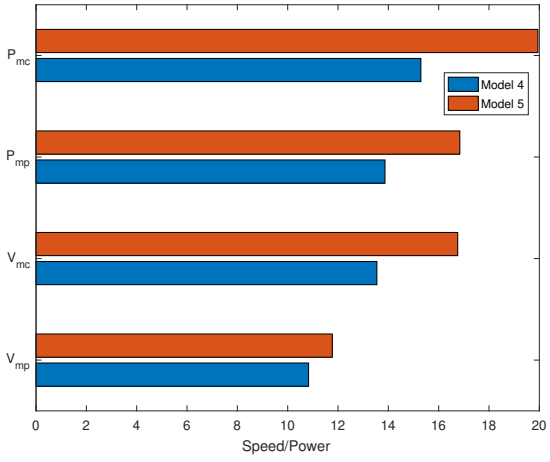

Figure 5.22: P.I. Comparison

P.I.	Allometric	Lund Results	Model 5
V_{mp}	9.33	12.03	11.77
V_{mc}	16.28	16.024	16.76
P_{mp}	13.54	12.84	16.84
P_{mc}	18.53	14.93	19.94
COT_{min}	0.1043	0.0774	0.1097

Table 11: **Model 5**: Points of Interest

Unfortunately, even though V_{mp} and V_{mc} are closer to Lund results, this approach returns poor results in term of aerodynamic power. This is the last model of section 5.1. All these models lack of a lift-dependent viscous power contribution $P_{v,2}$, thus it is the role of the compensating factor k to address this missing contribution. This was the idea behind **Model 4** and **Model 5**.

We conclude this section by finding the V_{min} and V_{max} of **Model 4** and **Model 5**. The maximal aerodynamic power of the reference bird based on Lund model is equal to $P_{max_A} = 22.86$ [W].

P.I.	Lund Results	Model 4	Model 5
V_{min}	5.668	4.556	6.263
V_{max}	21.168	16.89	18.82

Table 12: **Model 4/5**: Max and Min speed

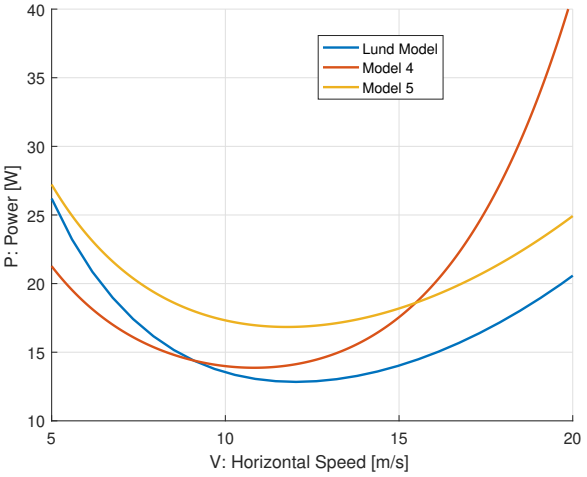

Figure 5.23: Lund model Comparison

5.2 ALL Power Curves

We address now the central topic of this work: the ALL/PSO power curves.

First the coupled model ALL/PSO is studied on two shoulder flight kinematic parameters:

- Flapping amplitude ϕ_{1_S}
- Pitching offset θ_{0_S}

These parameters are supposed to be the most relevant during flight. The rest of the articulation kinematic is identical to the **Reference** kinematic of section 4.3.

Afterward, the analysis is conducted on the 5 shoulder kinematic parameters; always keeping the elbow and wrist kinematic of the **Reference** case:

- Flapping amplitude ϕ_{1_S}
- Pitching offset θ_{0_S}
- Pitching amplitude θ_{1_S}
- Sweeping offset ψ_{0_S}
- Sweeping amplitude ψ_{1_S}

Finally, we end this section by exposing the limitations of the current coupled model and by suggesting possible solutions to enlarge its reach.

5.2.1 Two parameters optimization: ϕ_{1_S}, θ_{0_S}

Optimizing ALL kinematic for two parameters λ_{kin} is the same as solving a system of two equations (i.e. trim conditions). The solution obtained is the unique one possible.

The PSO search space is often limited to avoid undesirable solutions. For this first analysis, we constrained the flapping amplitude ϕ_{1_S} and the pitching offset θ_{0_S} to the following range[25]:

$$\lambda_{kin} = [\phi_{1_S}, \theta_{0_S}] \in \{0, 70°\} \tag{5.9}$$

The optimization is repeated for different flight speed V_∞:

$$V_\infty = [4, 5, 6, 7, 8, 9, 10, 12, 14, 16, 18] \quad m/s \tag{5.10}$$

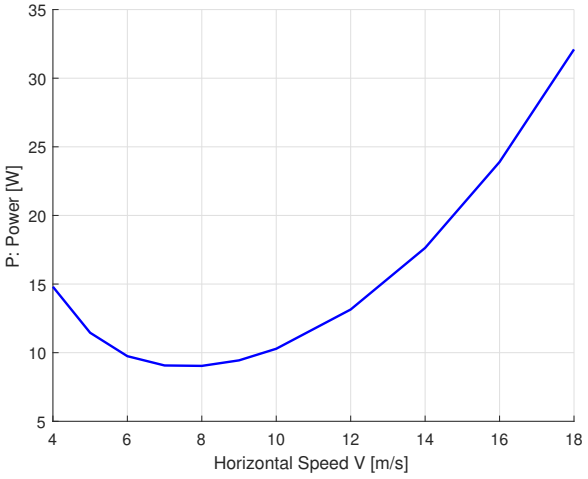

Figure 5.24: Power curve

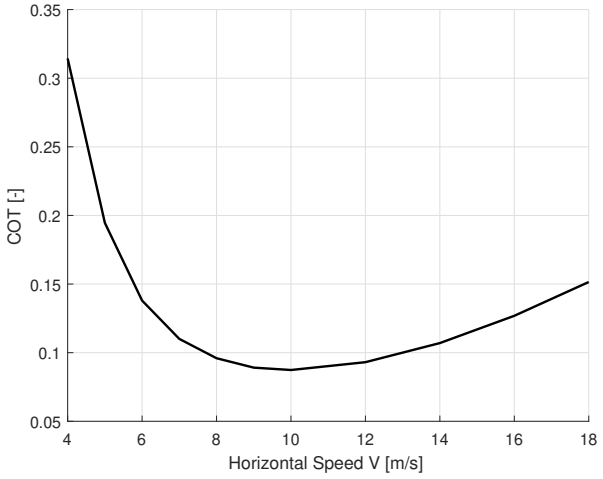

Figure 5.25: Cost of transport

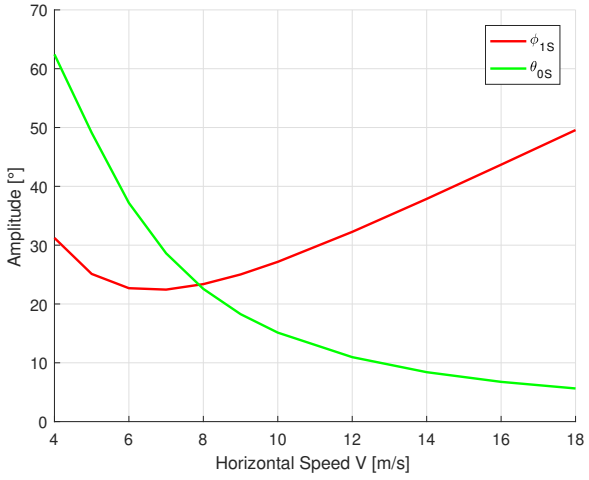

Figure 5.26: Flight kinematic

Figures 5.24, 5.25 and 5.26 present the results of this first optimization. The power curve is in the right power range (see AFPT results) but the minimum power speed V_{mp}(= 8 m/s) and the minimum COT speed V_{mc}(= 10 m/s) are quite low when compared to the results of section 5.1. Despite that, the minimum cost of transport $COT_{min} = 0.0874$ sits between allometric and Lund results.

[25]The selected range is arbitrary, in a future study a more specific range could be envisioned.

P.I.	Allometric	Lund Results	ALL Model
V_{mp}	9.33	12.03	8
V_{mc}	16.28	16.024	10
P_{mp}	13.54	12.84	9.04
P_{mc}	18.53	14.93	10.29
COT_{min}	0.1043	0.0774	0.0874

Table 13: **ALL Model**: Points of Interest

The flapping amplitude ϕ_{1_S} reaches its minimum near the minimum power speed V_{mp}. It increases rapidly at low speed and gently at high speed. The same trend was obtained by Lund research team. However, the flapping amplitude ϕ_{1_S} here is considerably low; the minimum obtained by the AFTP was around 31°, in our case it sits below 25° (exact value 22.44°).

The offset angle θ_{0_S} decreases sharply when the flight speed V_∞ increases. This is exactly the same trend as the stroke-plane angle γ. The ALL model is bodyless, thus we can say that in this context, the offset angle θ_{0_S} is exactly the stroke-plane γ. Figure 5.27 depicts this analogy.

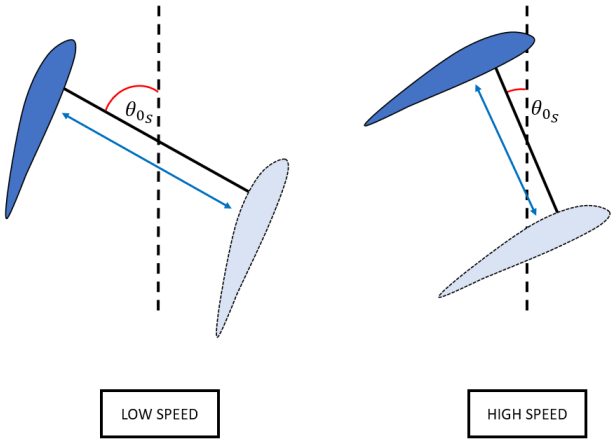

Figure 5.27: Stroke plane γ analogy

The comparison with both Pennycuick's experimental (section 2.3) and Lund numerical results suggests that the kinematic parameter θ_{0_S} follows the correct trend.

Some of the obtained results, even if trimmed, might be impossible to sustain due to stall condition. The stall limit in avian flight is not well documented in literature, we imagine here that stall occurs at an angle of attack of $\alpha = 20°$.

To help us visualise what part of the power curve is more realistic, Figures 5.28, 5.29 and 5.30 show both the aerodynamic forces and angle of attack over a cycle for various flight speeds. A solution of the model is accepted only if the angle of attack in the central part of wing is below the stall limit. The wingtips zone has a negligible contribution to lift generation, therefore, it is acceptable for this zone to be in a moderate stall condition; wingtips stall will not be considered as a problem for avian flight.

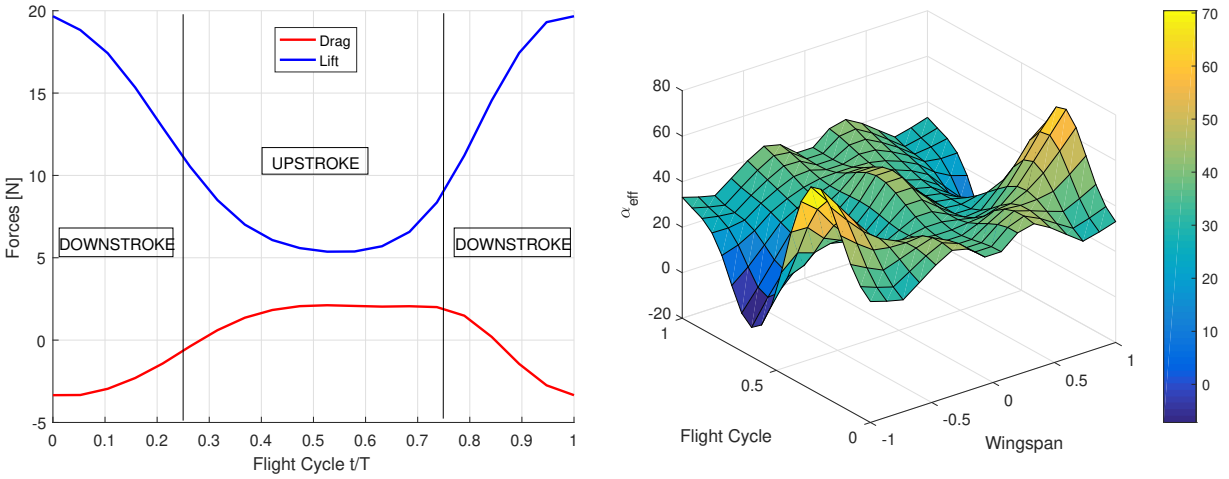

Figure 5.28: Aerodynamic forces and Angle of attack at 6 [m/s]

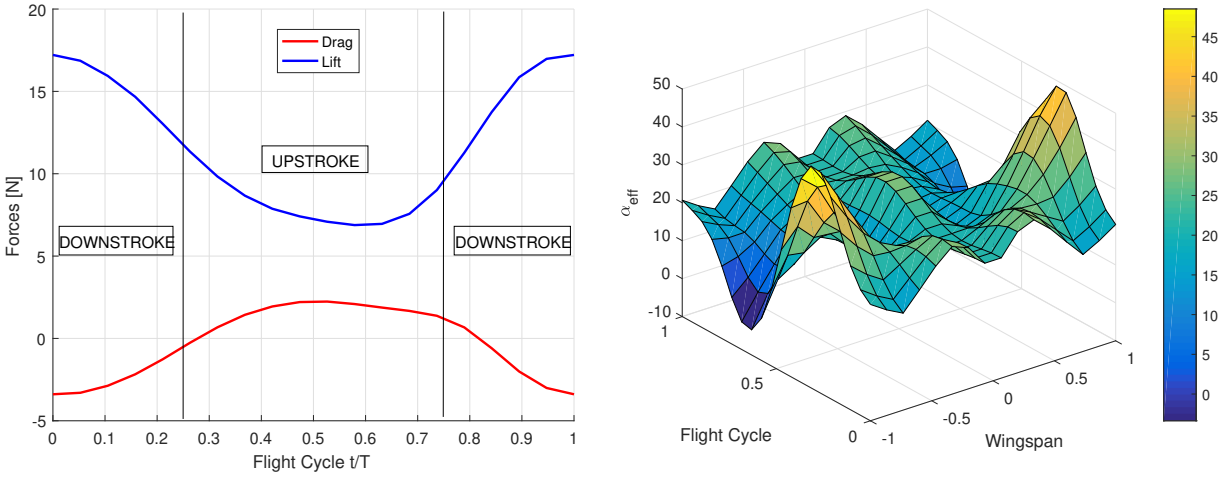

Figure 5.29: Aerodynamic forces and angle of attack at 8 [m/s]

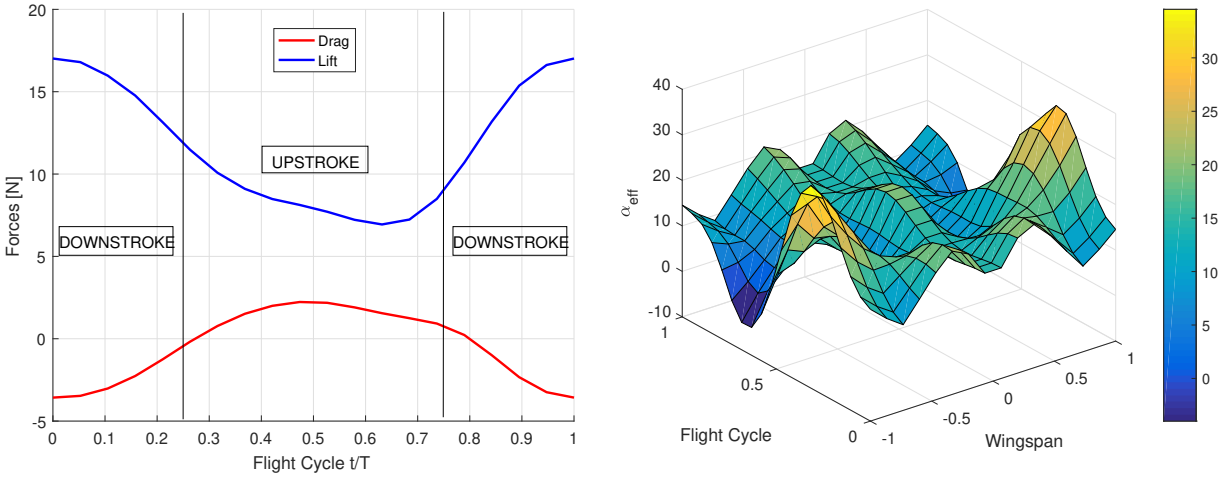

Figure 5.30: Aerodynamic forces and angle of attack at 10 [m/s]

The aerodynamic forces over a cycle do not give any real insight on the validity of the flight. The angle of attack, on the other hand, leads us to the following conclusions:

- 6 m/s: the wing is in stall for the majority of the time, this flight is not realistic
- 8 m/s: half of the wing (from 0.5 to 1) is in stall, this flight is more plausible

– 10 m/s: only the wingtips are in stall, this flight is realistic

These results suggest to approach the optimization problem differently.

Rather than optimizing just the aerodynamic power P, the J cost function should also penalise flight kinematic solutions that are in stall. For example, we could add to J a penalising factor that takes as input the mean angle of attack α_{mean} over a flapping cycle; the cost function J would then resemble to the following equation:

$$J = P^2 + \zeta|Trim| + \xi(\alpha_{mean}) \tag{5.11}$$

with for example:

$$\xi(\alpha_{mean}) = \begin{cases} 0 & \text{for } \alpha_{mean} < \alpha_{stall} = 20° \\ 100|\alpha_{mean} - \alpha_{stall}| & \text{for } \alpha_{max} > \alpha_{stall} = 20° \end{cases} \tag{5.12}$$

Another factor that might affect the validity of the flight is the flapping frequency f. As stated in the section 2.3, this flight parameter is high at low speed, reaches a constant value at mid-speed and rises at higher speed.

In order to visualize the impact of a frequency change on the ALL power curves, we conducted an optimization on the following model variation (speed range $V_\infty = [6, 8, 10, 12, 14, 16, 18]$ [m/s]):

- **Reference** case with $f = 3$ [Hz]
- **Reference** case with $f = 5$ [Hz]

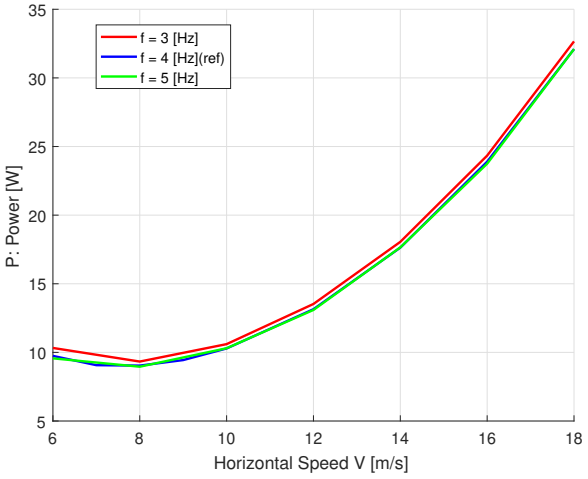

Figure 5.31: Power curve comparison

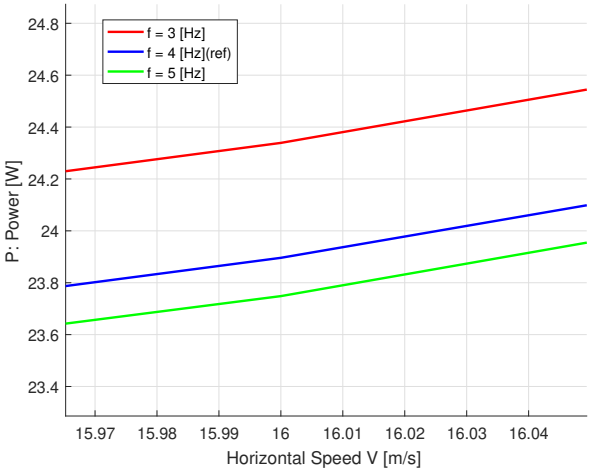

Figure 5.32: Zoom of the power curves

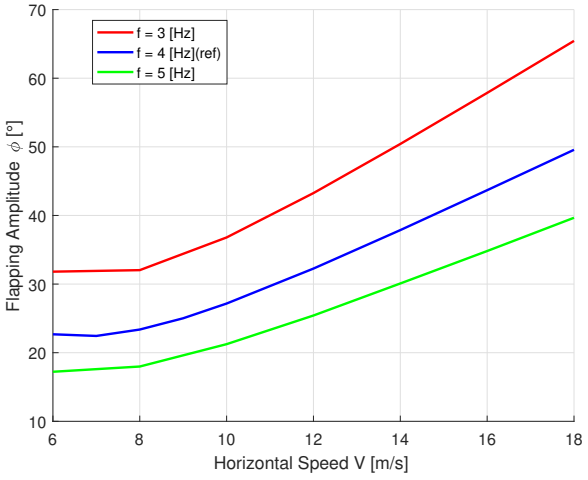

Figure 5.33: Flapping amplitude variation ϕ_{1_S}

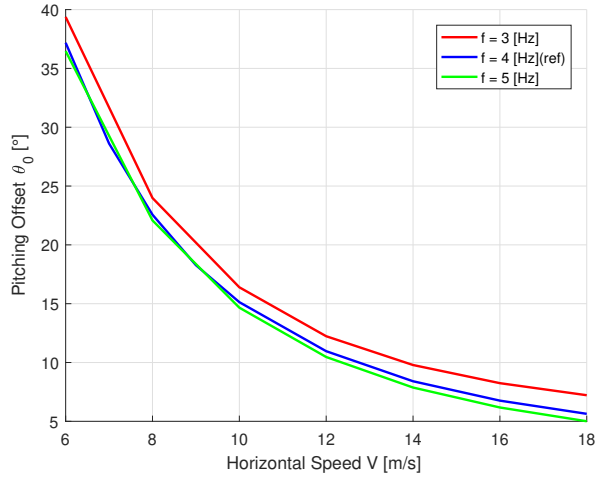

Figure 5.34: Pitching offset variation θ_{0_S}

Surprising enough, the frequency variations do not have any noticeable impact aerodynamic power P. This result is counterintuitive; aerodynamic power should increase with the flapping frequency f. By zooming on the plot, we can see that the contrary occurs; the aerodynamic power is inferior at higher frequencies. Additional researches must be conducted to assert the validity of this trend.

From Figure 5.33 is possible to affirm that the flapping amplitude ϕ_{1_S} is inversely proportional to the flapping frequency f.

This trend is explained through the following equation, describing the plunging velocity of the shoulder joint:

$$\dot{\phi}_S = A\cos(2\pi ft{+}180°) = 2\pi f\phi_{1_S}\cos(2\pi ft{+}180°) \tag{5.13}$$

This equation is directly linked to the kinematic velocity v_{kin} of the wing. For the **Reference** case A has specific value suited for trim conditions. If the flapping frequency decreases, the value of A decreases.

In order to ensure trim conditions, the flapping amplitude ϕ_{1_S} must increase. Inversely, if f increases the flapping amplitude ϕ_{1_S} decreases to satisfy trim conditions.

This gives a simplistic way of understanding the "antagonistic" relation between the flapping frequency f and amplitude ϕ_{1_S}.

The pitching offset θ_{0_S} seems to be affected in a similar way by the frequency changes. Although, the variations of this parameter are small when compared to the flapping amplitude variations.

In conclusion, is possible to assert that the flapping amplitude ϕ_{1_S} and the pitching offset θ_{0_S}, in a minor way, are "tuned" by the bird to continue to satisfy trim conditions when a change in flapping frequency f is necessary.

5.2.2 Five parameters optimization: ϕ_{1_S}, θ_{0_S}, θ_{1_S}, ψ_{0_S}, ψ_{1_S}

The 5 shoulder parameters are now free to take a value within the following range:

$$\lambda_{kin} = \begin{cases} [\phi_{1_S},\, \theta_{0_S}] \in \{0, 70°\} \\ [\theta_{1_S}] \in \{0, 10°\} \\ [\psi_{0_S}, \psi_{1_S}] \in \{0, 30°\} \end{cases} \tag{5.14}$$

The range of θ_{1_S} is different from the other parameters because a high pitching amplitude θ_{1_S}, generates undesirable effects at mid to high speed. These effects will be discussed later.

The range of ψ_{0_S} and ψ_{1_S} were chosen to constrain the maximum sweep angle below 60°. This analysis was conducted for the subsequent flight speeds:

$$V_\infty = [6, 8, 10, 12, 14, 16, 18] \quad m/s \tag{5.15}$$

Due to a lack of consistency in the results, the PSO optimization was repeated at least 10 times for each speed. Through this cluster of results, it was possible to extract a plausible correlation between the kinematic parameters λ_{kin} and the flight speed V_∞.

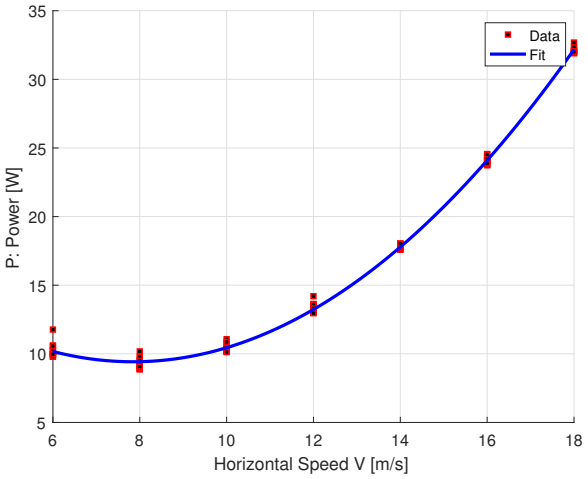

Figure 5.35: Power Curve

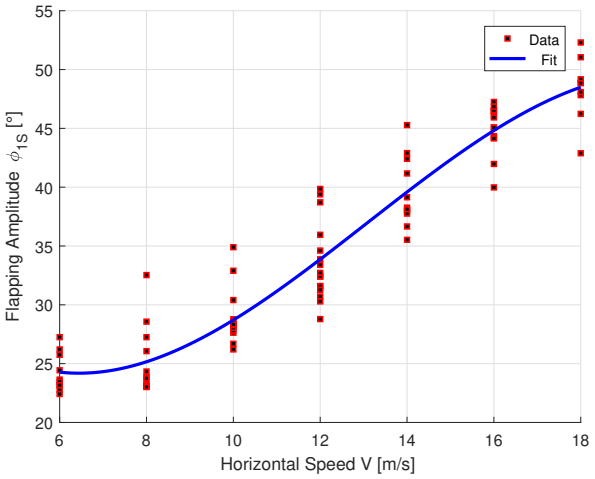

Figure 5.36: Flapping amplitude ϕ_{1_S}

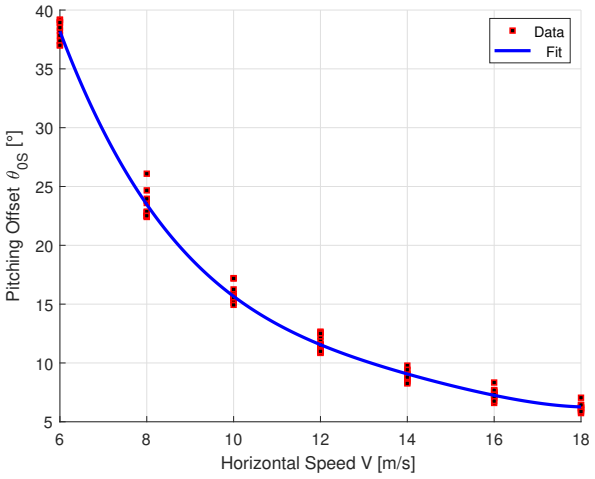

Figure 5.37: Pitching offset θ_{0_S}

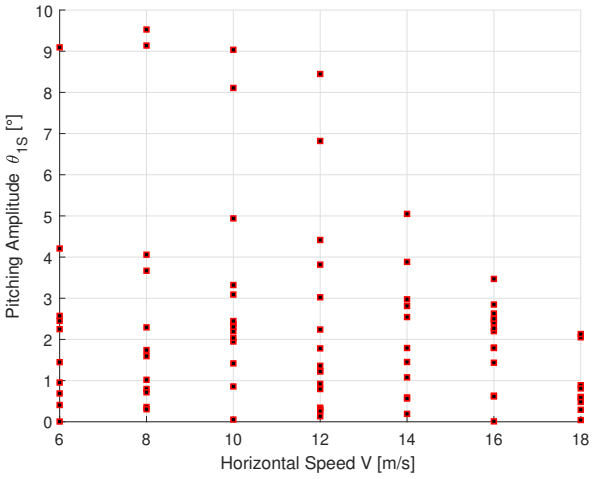

Figure 5.38: Pitching amplitude θ_{1_S}

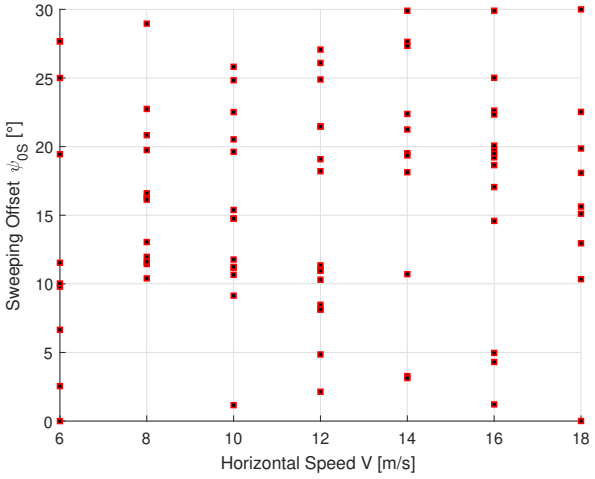

Figure 5.39: Sweeping offset ψ_{0_S}

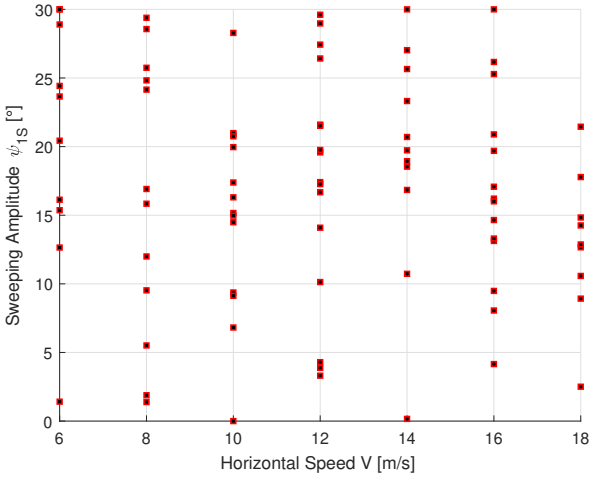

Figure 5.40: Sweeping amplitude ψ_{1_S}

We can clearly see, from Figure 5.35, that the power curve is similar to the one obtained in the previous optimization.

The flapping amplitude ϕ_{1_S} is affected by the changes of the other kinematic parameters but conserves, overall, the trend depicted in Figure 5.26.

The pitching offset θ_{0_S} is only slightly influenced by the changes of the other kinematic parameters and thus follows the same trend as Figure 5.26.

From these observations and based the flapping frequency f analysis results, it is possible to state that trimmed flight is strongly related to the flapping amplitude ϕ_{1_S} and the pitching offset θ_{0_S}.

These two parameters clearly hold the most important role in flight kinematic. They act as "flight regulators", ensuring trim conditions for every change in the flight kinematic.

Furthermore, is worth pointing out that the "flight regulator" role of the flapping amplitude ϕ_{1_S} is prevalent respect to the pitching offset θ_{0_S}. Indeed, the changes of the flapping amplitude ϕ_{1_S} with respect to flight kinematic are more pronounced than the one of the pitching offset θ_{0_S}.

No apparent correlation can be found for the other kinematic parameters that seem to have no effect on the aerodynamic power P.

Still, the results related to the pitch amplitude θ_{1_S} are more present below 5°, indicating perhaps a power reduction for low values of θ_{1_S}.

For the sweeping offset ψ_{0_S} and amplitude ψ_{1_S} no evident trend can be deduced.

To understand what the role of these parameters might be, each of them is studied separately.

First we start with the pitching amplitude θ_{1_S}: two modified versions of the **Reference** case are studied and compared afterward with the **Reference** case. The two versions keep the same kinematic expect for the studied parameter:

- Version 1: $\theta_{1_S} = 5°$
- Version 2: $\theta_{1_S} = 10°$

The results of the optimization are depicted in the figures below; the speed range of the analysis is the same as the range in Equation 5.15.

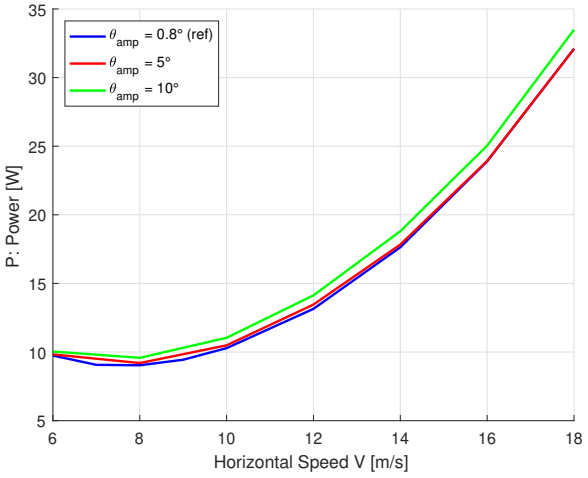

Figure 5.41: Power curves comparison θ_{1_S}

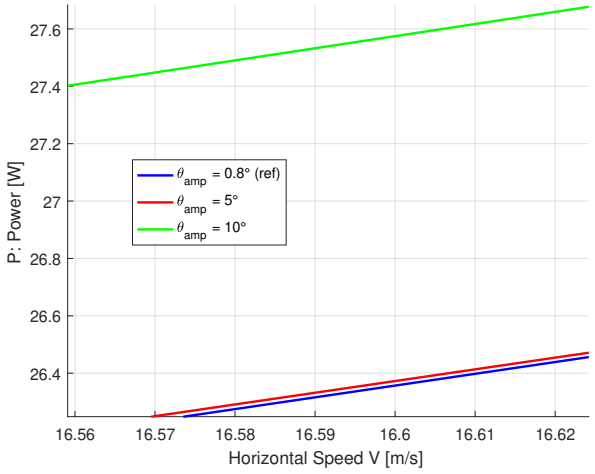

Figure 5.42: Zoom of the power curves θ_{1_S}

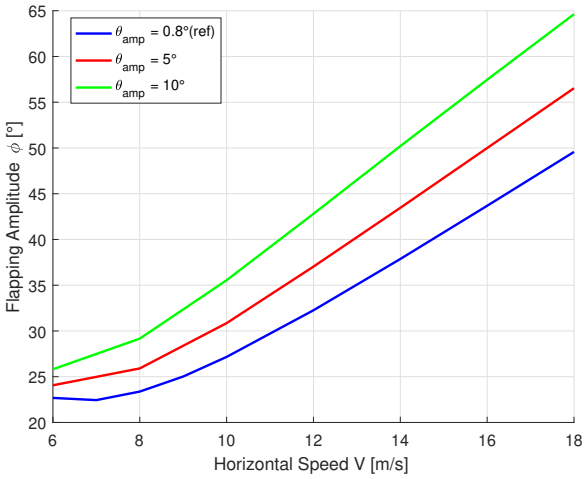

Figure 5.43: Flapping amplitude variation ϕ_{1_S}

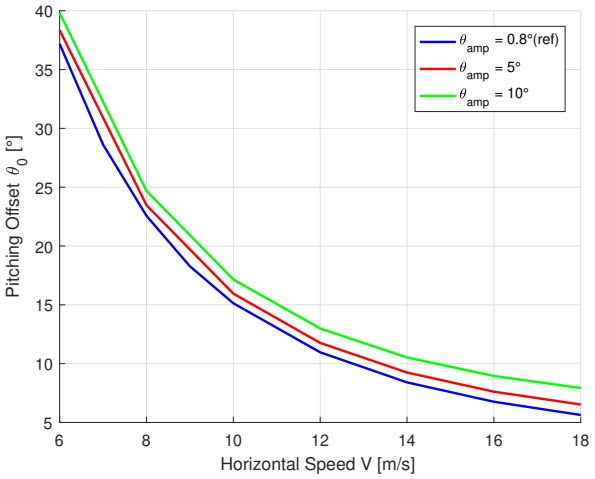

Figure 5.44: Pitching offset variation θ_{0_S}

The power curves confirm a power increase in relation to a pitching amplitude θ_{1_S} increase. This increase is hardly perceivable for $\theta_{1_S} = 5°$ but gets more consistent at $\theta_{1_S} = 10°$.

In addition, these pitch amplitude changes are balanced by an augmentation in flapping amplitude ϕ_{1_S} and in pitching offset θ_{1_S}.

From these results nothing can be said about the role of this parameter. We can speculate that the pitch amplitude θ_{1_S} has an important role at very low and low speeds and it is negligible at high speeds.

This could be demonstrated by looking at the effects of this parameter on the wings angle of attack. Figure 5.45 depicts the supposed behaviour of θ_{1_S} and Figures 5.46 and 5.47 show the wings angle of attack for two flight speeds and two pitching amplitudes.

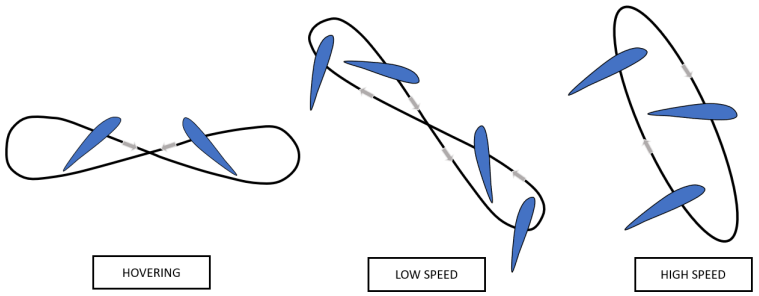

Figure 5.45: Image Reproduction (Figure 5.6 of **(8)**): Pitch amplitude θ_{1_S} role

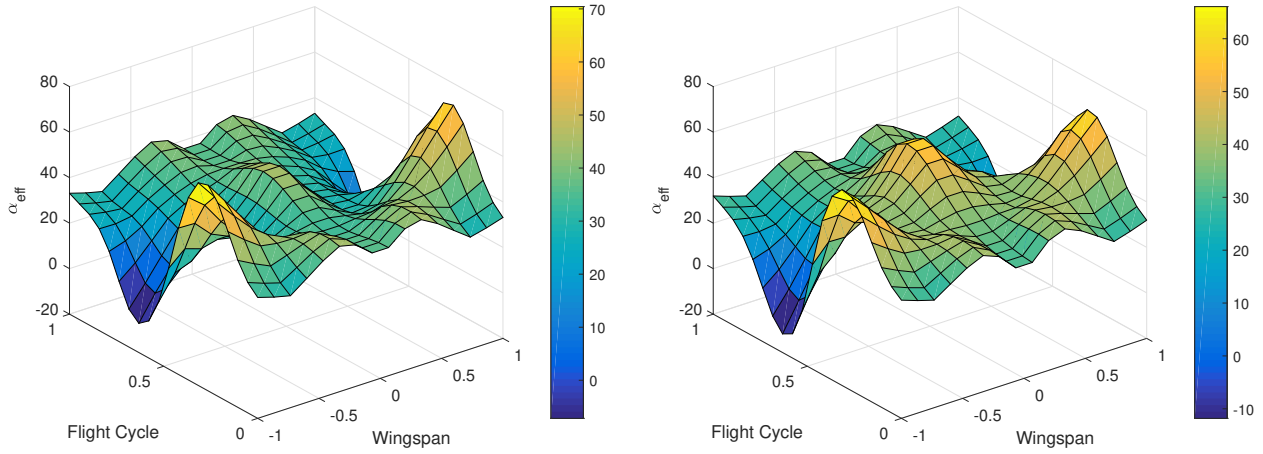

Figure 5.46: Angle of attack $V_\infty = 6$ m/s: $\theta_{1_S} = 0.8°$ (left) and $\theta_{1_S} = 10°$ (right)

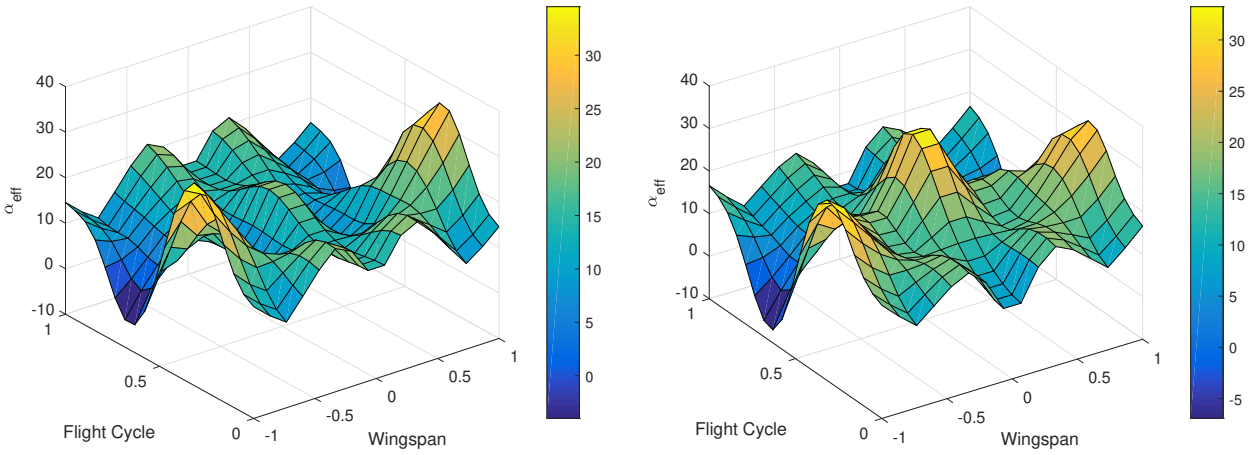

Figure 5.47: Angle of attack $V_\infty = 10$ m/s: $\theta_{1_S} = 0.8°$ (left) and $\theta_{1_S} = 10°$ (right)

At low speed $V_\infty = 6$ [m/s], the pitching amplitude θ_{1_S} reduces the wings angle of attack; this parameter could prevent premature stall in this flight zones.

At higher speed, θ_{1_S} seems to have a detrimental effect on the angle of attack; an abnormal pic is present during upstroke. This type of behaviour cannot be found in nature. For this reason, in the optimization, the maximum range of this parameter was limited to $\theta_{1_S} = 10°$.

Based on Figure 5.45 the pitch amplitude θ_{1_S} should decrease with respect to the flight speed V_∞ but with our current framework is not possible to demonstrate this trend.

The problem here is related to the nature of the search space. The search space is composed by a high number of solutions that are close to each other in term of aerodynamic power P but are far in term of kinematic λ_{kin} (i.e. Rastrigin's search space). The PSO framework cannot distinguish two solutions that have nearly the same aerodynamic power P, therefore, the real global minimum is hardly found. It is possible that adding other constraints to the J cost function could help the PSO to reach the expected solutions.

The same approach is used to analyse the other two shoulder kinematic parameters: ψ_{0_S} and ψ_{1_S}. The four modified versions studied, are:

- Version 3: $\psi_{0_S} = -10°$
- Version 4: $\psi_{0_S} = -30°$
- Version 5: $\psi_{1_S} = 10°$
- Version 6: $\psi_{1_S} = 30°$

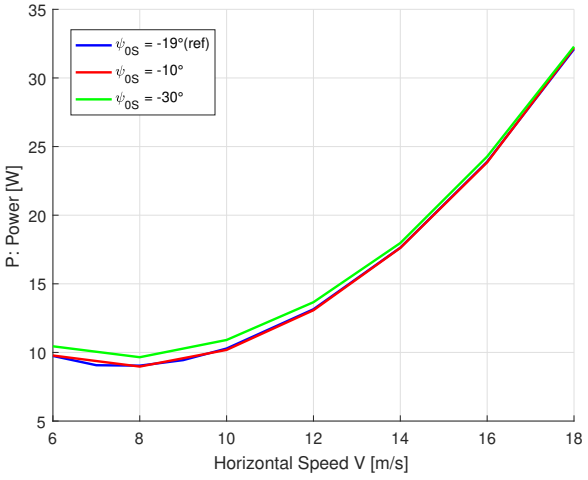

Figure 5.48: Power curves comparison ψ_{0_S}

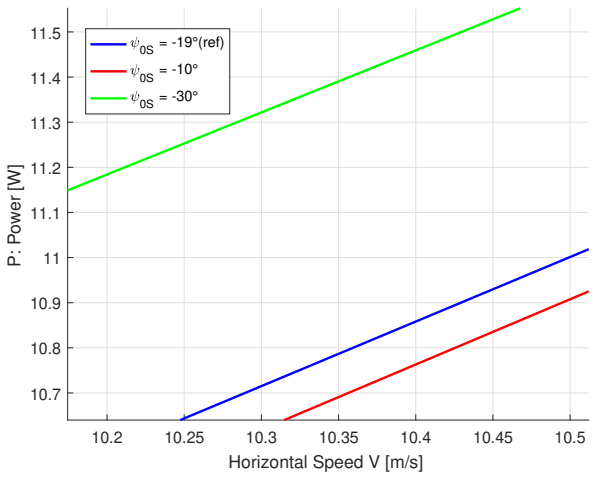

Figure 5.49: Zoom of the power curves ψ_{0_S}

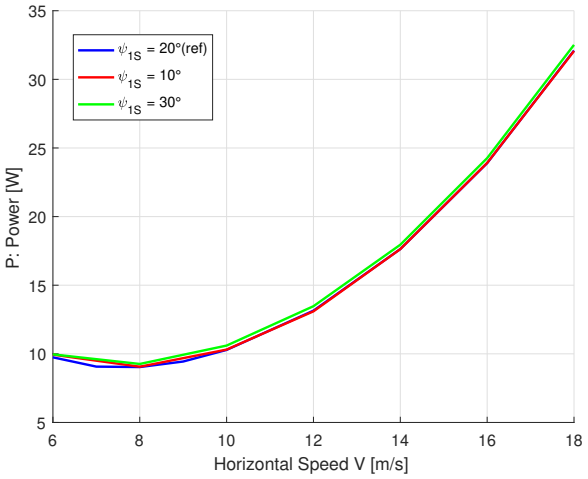

Figure 5.50: Power curves comparison ψ_{1_S}

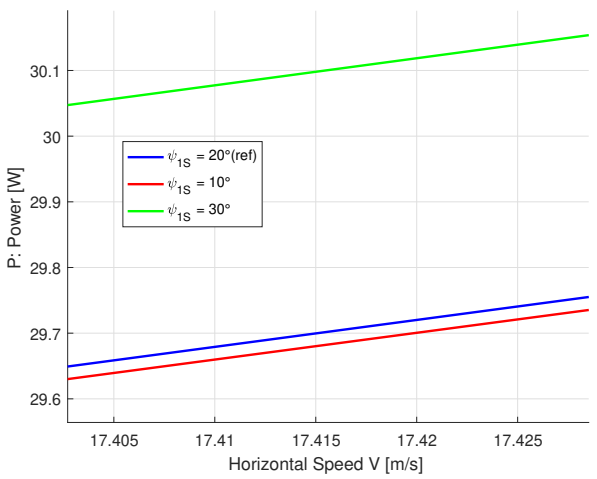

Figure 5.51: Power curves comparison ψ_{1_S}

Again, from the above graphs, it is possible to state that the sweeping offset ψ_{0_S} and amplitude ψ_{1_S} have a negligible effect on the bird aerodynamic power P. Although, high sweeping offset ψ_{0_S} can be detrimental at low and mid flight speed.

The shoulder sweeping motion is responsible with the other joints sweeping motions (i.e. **E**, **W**) of the wing retraction (see right image in Figure 4.12). As said in chapter 3, the wing retraction has a fundamental role in minimizing drag during flight.

The obtained results show the opposite; wing retraction seems to not participate actively to aerodynamic power reduction. In order to clearly assert the previous statement, we run the optimization for a specific version of the **Reference** case: in this case the shoulder, elbow and wrist sweeping motions are set to zero degrees (**Zero** case). Figure 15 depicts a comparison between the **Zero** and the **Reference** case.

Joint	α_0 [°]	α_1 [°]	η [°]
Shoulder x	free	0.8	−90
Shoulder y	0	0	90
Shoulder z	0	free	180
Elbow x	0	−30	90
Elbow y	0	0	−90
Wrist y	0	0	−90
Wrist z	0	0	0

Table 14: Zero case kinematic

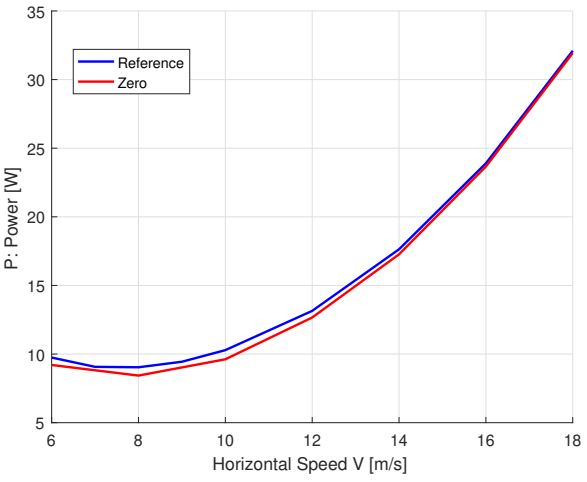

Table 15: Power: **Zero** & **Reference** case

Figure 15 indicates, also, that wing retraction, surprisingly enough, have a detrimental impact on the bird aerodynamic power P. At low flight speed the power is lower if the wings are left unretracted. Often these power variations are not noticeable by the optimization tool.

Thus, from this analysis, we can assert that the aerodynamic power P seems to be barely affected by the flight kinematic. This implicitly means that the flight kinematic is only responsible of ensuring trim conditions and that the aerodynamic power depends almost exclusively on the bird morphology (i.e physical characteristics).

5.2.3 Coupled Model Limitations

The results obtained in the previous subsections are unexpected. According to the literature power curves of section 5.1 the flight kinematic parameters λ_{kin} should have a relevant role/impact on the aerodynamic power P of the bird. Instead, the ALL/PSO coupled model shows the opposite.

We have seen that the search space of this problem is narrow and that the power variations from two distant kinematic results are extremely small.

Based on my knowledge, any type of optimizer would hardly find a global minimum in this search space. Understanding the nature of flight through this method seems to be a hard task. Apart from the flapping amplitude ϕ_{1_S} and the pitching offset θ_{0_S}, that can be considered as pillars of the flight kinematic, the other parameters do not follow a specific trend that would identify their flight role.

This implies that other factors might determine the flight kinematic selected by a bird. Introducing a stall condition penalisation factor in the J cost function could help to restrict the pool of solutions.

Another interesting addition to ALL model could be a model describing the wing inertia. The J cost function would then contemplate the muscular power P_{mus} of the reference bird rather than the aerodynamic power:

$$P_{mus} = P_{aero} + P_{in} \tag{5.16}$$

where P_{aero} is the aerodynamic power and P_{in} is the inertial power.

This new addition might open up new ways of understanding bird flight kinematic. Some of the solutions obtained in the previous subsections could become expensive in term of muscular power P_{mus} and therefore discarded by the PSO.

The validity of the trim conditions $Trim$ should also be a topic of discussion. We have seen that in general the drag coefficients, $C_{D_{pro}}$ and C_{D_b}, are not well documented in literature. The parasitic drag D_{par} at low speed V_∞ is often higher than the one we have considered in this coupled model. In addition, as stated in section 5.1, the profile drag coefficient $C_{D_{pro}}$ seems to follow a parabolic trend. All these factors might affect the optimization results and unveil new correlation between the flight kinematic parameters.

A relevant amount of time was invested in optimizing the overall ALL model by freeing the elbow and the wrist kinematics. The obtained results did not show any specific trend with respect to the bird flight speed and led to similar conclusions of the previous subsection; the flight kinematic parameters barely affected the bird aerodynamic power P.

To avoid any redundancy in the analysis, these results are not included in this thesis.

In addition, a parametric analysis analogous to the preceding subsection was conducted. Apart from the elbow pitching amplitude θ_{1_E}, that seems to have an appreciable impact on the aerodynamic power, most of the obtained results, indicate a negligible impact on the bird aerodynamic power.

Therefore, here, we will only report the elbow pitching amplitude θ_{1_E} results of this analysis; the modified versions of the **Reference** case studied are listed here below:

- Version 7: $\theta_{1_E} = -10°$
- Version 8: $\theta_{1_E} = -20°$
- Version 9: $\theta_{1_E} = -40°$

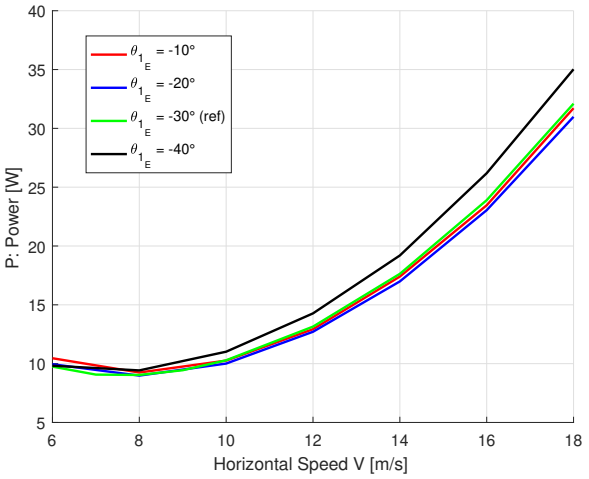

Figure 5.52: Power curves comparison θ_{1_E}

These results, suggest that for this specific flight kinematic, the optimal value of the pitching amplitude θ_{1_E} sit around $-20°$. In conclusion, Figure 5.52 shows again that distant flight kinematics λ_{kin} solutions share a similar aerodynamic power. This confirm the impossibility of the optimizer to discern two solutions that share nearly the same cost J.

6 Conclusion

This chapter provides a summary of the tools used in the thesis and of the results of this work. For better clarity, each conclusion is presented through a highlighted statement followed by a short discussion.

6.1 Tools Summary

Rapid method to retrieve the power curve of a bird of mass m.

In section 5.1 a study was conducted on the literature power curves model.
Assuming the bird as static structure (i.e. turbine), Rayner's part 1 model **(41)** was merged with the Pennycuick actuator disk model **(28)** resulting in a hybrid model capable of returning acceptable estimations of the bird power curve points of interest (i.e. V_{mp}, V_{mc}, P_{mp}, P_{mc}).

This hybrid model should be used as tool to get a first idea on the aerodynamic power needed to support the flight of the selected bird.

Under no circumstances, this model can be considered as a valid tool to describe the nature of birds flight kinematic.

Optimization tool to trim and to find the minimum power curve of the articulated lifting line of the RevealFlight project.

In chapter 4 the coupling between the articulated lifting line (ALL) and a particle swarm optimizer (PSO) was developed along with a proposal of a J cost function ensuring trim conditions and minimizing the aerodynamic power of the reference bird.

In addition, a novel way of evaluating the profile drag D_{pro} through the articulated lifting line was suggested.

6.2 Results Summary

Articulated lifting line power curves.

In section 5.2 the power curve is derived from the Reference kinematic of section 4.3. The obtained results, for the reference bird, respect the correct power range, although, the points of interest of the power curve differ strongly from those of Lund power curves **(33)**.

Despite that, the minimum cost of transport COT_{min} resulting from this analysis is in accordance with literature data.

The articulated lifting line flight kinematic results are similar to the literature findings.

The Reference kinematic (section 4.3) is trimmed in section 5.2. The flight kinematic parameters retrieved are the flapping amplitude ϕ_{1_S} and the plunging offset θ_{0_S}.

These two parameters are studied with respect to the bird flight speed V_∞. The flapping amplitude ϕ_{1_S} follows a pseudo parabolic trend with a minimum located close to the minimum power speed V_{mp}. The slope of this pseudo parabola is higher at low flight speed than at high flight speed. This trend is in accordance with Lund numerical method results **(33)**.

The pitching offset θ_{0_S} is found to be equivalent to the stroke-plane angle γ. This kinematic parameter follows a pseudo negative exponential trend. This trend is in accordance with both the Pennycuick's experimental data **(28)** and Lund numerical method results **(33)**.

The flapping amplitude $\boldsymbol{\phi_{1_S}}$ and pitching offset $\boldsymbol{\theta_{0_S}}$ are the most relevant kinematic parameters in avian flight.

In the subsection 5.2.2, the ALL/PSO coupled model was applied to the bird shoulder kinematic. Due to poor consistency in the results, the optimization was conducted several times.

The overall analysis showed that the flapping amplitude ϕ_{1_S} and the pitching offset ϕ_{1_S} varied depending on the other flight kinematic parameters but maintained the trends previously described.

The variations of these two parameters appeared to be fundamental to ensure trim conditions for any flight kinematic. A similar behaviour was shown in the flapping frequency f analysis of section 5.2.1; this analysis confirmed that the flapping amplitude ϕ_{1_S} variations compensated the flapping frequency f changes.

In the articulated lifting line model, the bird aerodynamic power is almost exclusively related to the bird physical characteristics.

The goal of this thesis is to understand the effects of the flight kinematic parameters on the power curves. My work shows that, in ALL model, the kinematic parameters have a negligible impact on the bird aerodynamic power.

The power variations with respect to the flight kinematic are often too small and can be hardly captured by the optimizer.

Wing retraction, that generally plays an important role during flight, had, in this study, a detrimental effect on the aerodynamic power.

The thesis has qualitatively shown that the search space of this problem is similar to a Rastrigin's function and consequently finding a global minimum remains a complex task.

Using a higher number of particles k for the optimization could lead to more meaningful results.

In conclusion, in this study, the aerodynamic power seems to be determined only by the physical parameters of the bird such as its mass m, wingspan b, wing area S, body frontal area S_b, body drag coefficient C_{D_b} and profile drag coefficient $C_{D_{pro}}$.

Additional time should be spent in assuring the validity of the results obtained. Understanding why the kinematic parameters do not affected the bird aerodynamic power could be the main focus of future researches.

Investigating the specific role of each flight kinematic parameter could be highly beneficial for the avian flight field of research too.

Finally, I am confident that the articulated lifting line model has the potential to open up new horizons in the comprehension of birds flight.

7 Future Work

This final chapter develops a plausible extension of the articulated lifting line. This extension could potentially enlarge the capabilities of the ALL.

The idea is to introduce in ALL a model describing the wing inertia in order to evaluate the muscular power P_{mus} generated by the reference bird.

The aim of this chapter is to give to the reader a possible idea to approach the wing inertia problem.

We begin this model by defining the shape of a bird wing bone. In the article "*Reinforcements in avian wing bones: Experiments, analysis, and modeling*" **(76)** bird wing bones are modelled as hollow cylinders or as hollow ellipses. In reality, as pointed out in the article above and shown in Figure 7.1, bird wing bones are asymmetrical hollow structures with internal calcium reinforcements called strut and ridges.

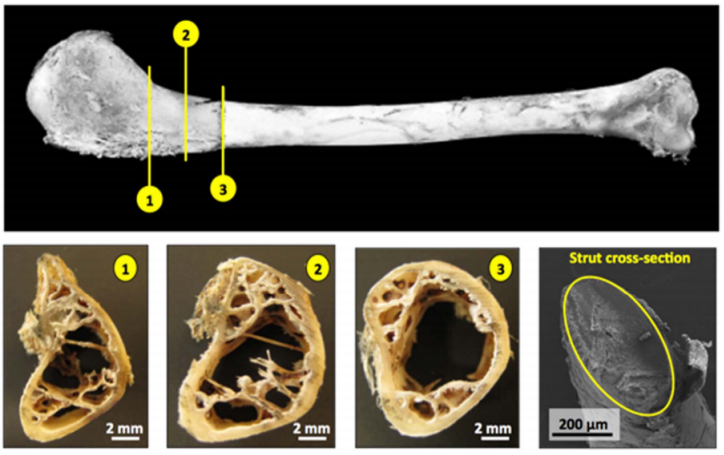

Figure 7.1: Turkey vulture humerus cross-section and microscopic analysis **(76)**

A proper bird wing skeleton is represented in Figure 7.2 where the Radius bone is not present. The length of each of the skeleton bones is different and the Carpus or Manus is divided in two bone segments. In addition, the extremities (epiphysis) of the bones are wider than the central part (diaphysis).

Reproducing this type of complexity is not feasible for the moment. We thus suppose that each bone of the wing can be represented by a hollow cylinder of external radius R and of thickness t. In Figure 7.3 this bone model is depicted.

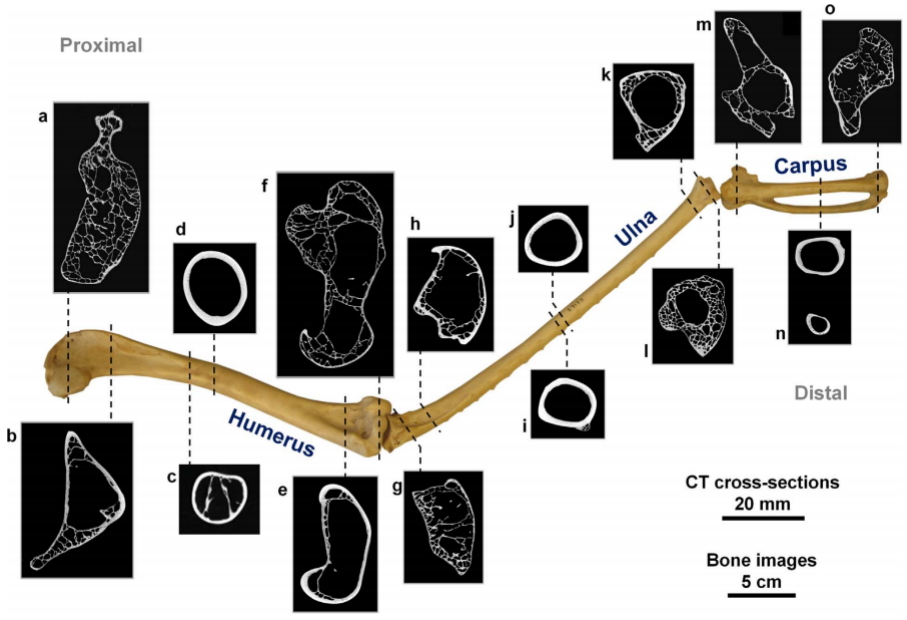

Figure 7.2: Micro-computed tomography sectional along a California Condor wing **(76)**

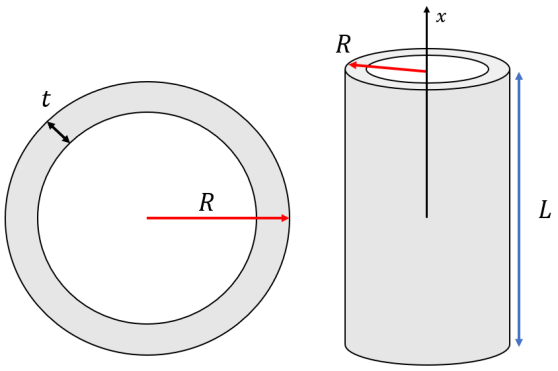

Figure 7.3: Hollow cylinder bone model

The length L of each bone of the White Ibis is already present in the ALL model:

- **Humerus**: $L_H = 0.134$ m
- **Ulna**: $L_U = 0.162$ m
- **Manus**: $L_M = 0.084$ m

An allometric formula defining the diameter of the humerus D_H is described in the article **(77)**:

$$D_H = 0.32 L_H^{0.8} \tag{7.1}$$

Looking at the diaphysis tomography showed in Figure 7.2, we assume that the diameter of the Ulna is equivalent to $D_U = \frac{2}{3} D_H$ and that the one of the Manus is $D_M = \frac{1}{2} D_H$.

The value of the wing bone thickness t is not well documented in literature. Therefore, based again on the diaphysis tomography of Figure 7.2, we suppose that the thickness of bird wing bones is approximately $t = \frac{1}{7} R$.

The moment of inertia I of a hollow cylinder, complying with the ALL reference frame notation, is defined by the following tensor:

$$\mathbf{I} = \begin{bmatrix} I_{xx} & 0 & 0 \\ 0 & I_{yy} & 0 \\ 0 & 0 & I_{zz} \end{bmatrix} \tag{7.2}$$

$$I_{xx} = \frac{1}{2} m_b (R^2 + (R-t)^2) \tag{7.3}$$

$$I_{yy} = I_{zz} = \frac{1}{12} m_b (3(R^2 + (R-t)^2) + L^2) \tag{7.4}$$

where m_b is the bone mass.

The wing mass m_w is derived using an allometric equation suggested in the article **(27)**:

$$m_w = 0.0706 m^{1.098} \tag{7.5}$$

For the White ibis ($m = 1.2$ kg), the mass m_w of a wing is equal to 0.0862 kg. We now assume that the mass of the wing is exclusively related to the bones mass; wing muscles and feathers masses are neglected.

The wing mass is distributed over the different bones. The Humerus seems to be the heaviest bone of the skeleton and the Manus the lighter consequently the wing mass m_w is disturbed on the skeleton as follow:

- **Humerus**: $m_H = \frac{3}{5} m_w$
- **Ulna**: $m_U = \frac{2}{5} m_w$
- **Manus**:$m_M = \frac{1}{5} m_w$

With all this information is possible to compute the torque $\vec{\tau}$ generated by the moving masses (i.e. bones) and obtain the inertial power P_{in}:

$$\vec{\tau} = \mathbf{I}\dot{\vec{w}} \tag{7.6}$$

$$P_{in} = \vec{\tau} \bullet \vec{w} \tag{7.7}$$

For the moment, the kinematic angular velocity $\vec{w}$ of each wing segment is not explicitly computed in the ALL model. Although, this value is derivable from the rotation matrices present in the ALL code (as done in section 8.4).

Lastly, the muscular power P_{mus} of the White Ibis is written as:

$$P_{mus} = P_{aero} + P_{in} \tag{7.8}$$

This discussion concludes my thesis. I firmly believe that adopting this simple model in ALL will provide new ways of interpreting the results of my thesis.

8 APPENDIX

8.1 Maybury Thesis, Body drag coefficient

This section deal with the body drag coefficient C_{D_b} of a bird. This topic is analysed through the thesis of Will J. Maybury *"The Aerodynamics of Bird Bodies"* **(21)** from where most of the images of this section are taken.

Flyers experience a resistance force on their bodies called parasitic drag. This drag is expressed as:

$$D_{par} = \frac{1}{2}\rho S_b C_{D_b} V^2 \tag{8.1}$$

The parasitic drag is related to two phenomena:

- **Pressure drag**: a pressure distribution due to an acceleration and deceleration of the flow around the bird body
- **Skin friction**: viscous effects caused by flow deceleration due to body friction.

Body friction depends on the body area, shape and surface texture; the characteristic of the boundary layer will strongly be affected by these parameters.

Before Maybury contribution, the parasitic drag was modelled using allometric equations extrapolated from a small range of birds. Different authors derived parasitic drag using the concept of equivalent flat plate area A_{f_p}. Pennycuick, in 1975 **(78)**, proposed the following formula:

$$A_{f_p} = 2.85{\cdot}10^{-3} m^{\frac{2}{3}} \tag{8.2}$$

Often these models do not vary with respect to the flow speed V_∞ and do not consider the morphology of the bird.

The goal of the author is to derive a parasitic drag model that depends on these omitted variables. Maybury study takes as a reference bird the European starling. The frozen body (wings and shoulder joint are removed) of this bird, is placed in a wind tunnel, as shown in Figure 8.1, and the parasitic forces around its body are derived. The trunk of the bird was treated using different products:

- Untreated (Unt)
- Waxed (Wax)
- Waxed Footless (Wax-F)
- Varnished (Var)

In addition, a model (i.e. a replica) in plaster of Paris (Mod) was created to imitate the trunk of the starling.

Two birds of the same specie are used for this analysis, since no bird is alike. In order to determine the drag coefficient C_{D_b}, Maybury first measures the minimal frontal projected area S_b for each treatment. Using these results he computes, also, a variable named fineness ratio that will be fundamental in his final analysis.

The fineness ratio FR is defined as the length from beak to tail divided by the mean body diameter (the diameter of a circle of area S_b).

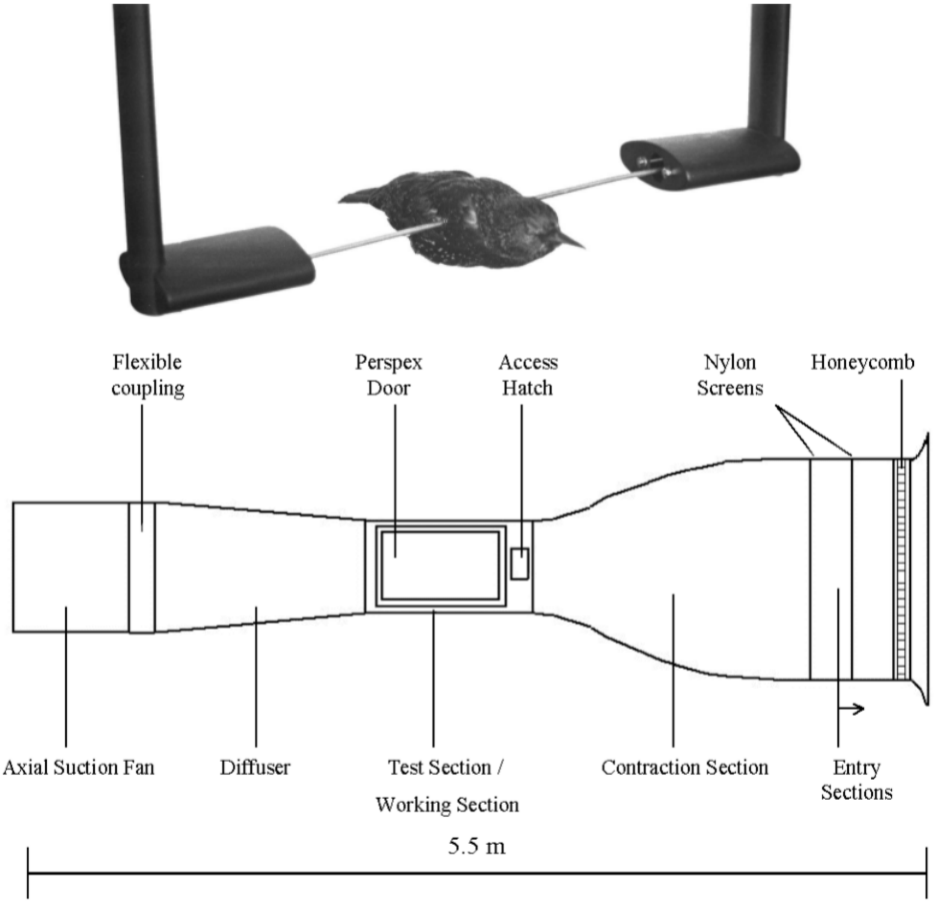

Figure 8.1: Experimental setup: reference bird and wind-tunnel

Maybury then proceeds to evaluate the coefficient C_{D_b} for different body inclination β and different freestream velocity V_∞. The results of his analysis are represented in Figure 8.2 where is visible a direct comparison between the Wax-F treatment and the plaster of Paris model (Mod). The analysis is conducted for speed between 4 m/s and 12 m/s and body inclinations ranging from 0° to 10°.

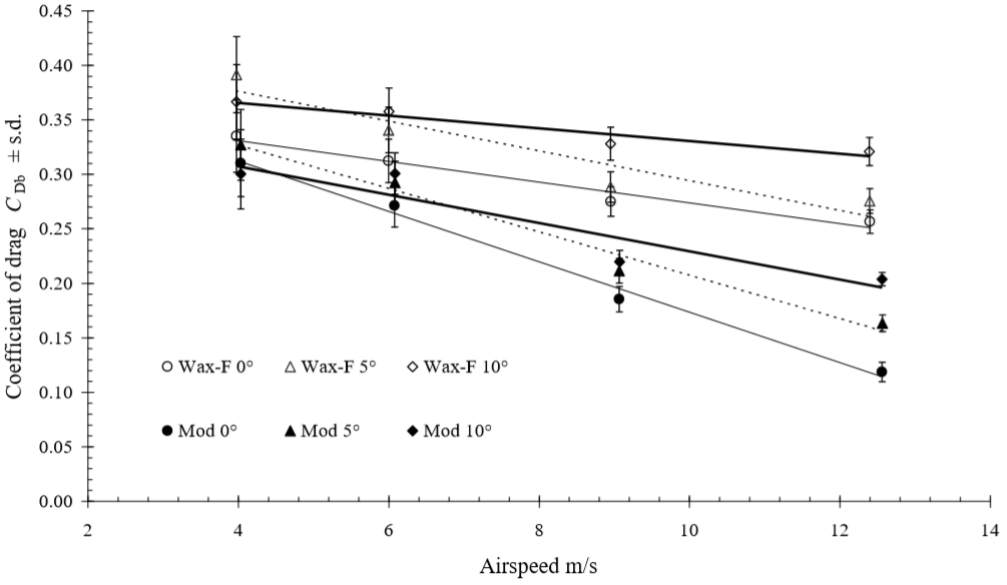

Figure 8.2: Body drag coefficient against airspeed and for different body inclination

As pointed out by Maybury, in his discussion paragraph, no frozen bird body can mimic exactly the aerodynamic conditions of a living bird.

The feathers are known to be subject to continuous active muscular control **(79)** to optimize the bird

flight performance (reduce drag). This feature is impossible to replicate on a frozen body. To get optimal results, one should study living birds in apposite wind tunnel (ex. Stanford **(80)** or Lund **(81)** bird wind tunnel).

Despite that, frozen trunks still give interesting results. In both specimens studied, when the airspeed increases C_{D_b} decreases.

To better understand this behaviour we will do an analogy with the well-known 'golf ball' effect (S.F. Hoerner **(82)**). Here I will quote Maybury. In this next passage, Re is the Reynolds number defined as $Re = \frac{\rho V_\infty l}{\mu}$ with l as the diameter of a body frontal area S_b:

"At a critical Reynolds Number Re_{crit}, the structure of the boundary layer changes from being undisturbed, laminar and smooth to turbulent oscillations. Re_{crit} occurs in the region of $10^{5.60}$ for spheres, but it is appreciably affected by shape and surface roughness."

Of course, the energy losses in the boundary layer of a turbulent flow are higher than in laminar flow. However, in turbulent flow, the separation of the boundary layer from the body surface is delayed. In fact, the airflow remains attached further toward the rear of the bird decreasing the pressure drag.

For each body shape there is a Re_{crit} for which drag coefficient is at its lowest value. Figure 8.3 depicts this behaviour for rough/smooth spheres and cylinders:

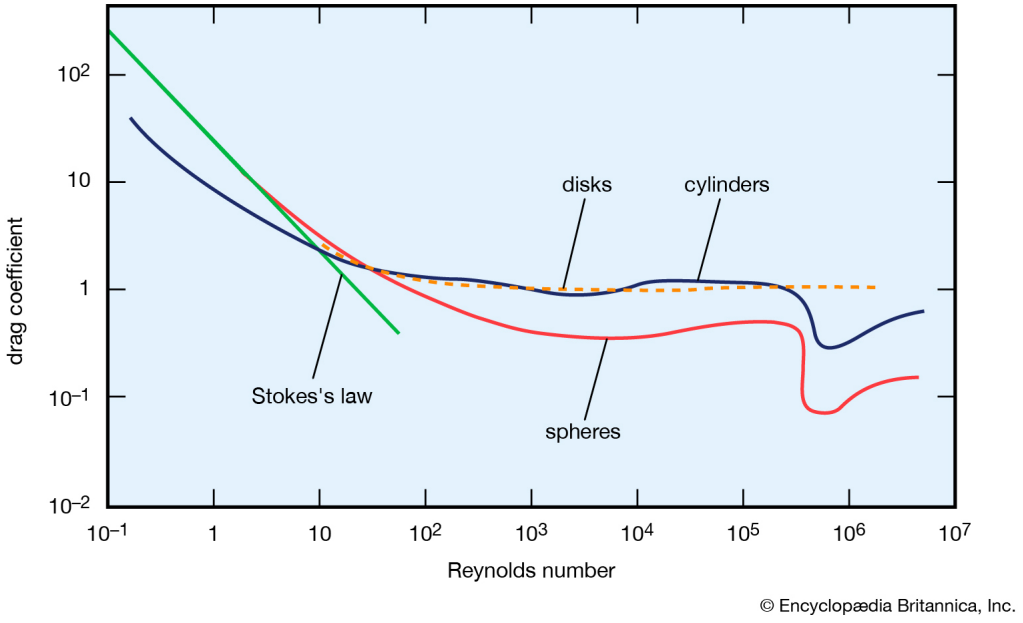

Figure 8.3: Drag coefficient evolution with respect to Re **(83)**

Pennycuick **(40)** after measuring the body drag of frozen bird torsos (waterfowl and raptors) found the following expression describing C_{D_b} as a function of Re and the trend obtained resembles the one shown in Figure 8.3:

$$C_{D_b} = \begin{cases} 0.4 & \text{for } Re \leq 10^{4.7} \\ 1.57 - 0.108 \ln(Re), & \text{for } 10^{4.7} < Re \leq 10^{5.3} \\ 0.25, & \text{for } Re \geq 10^{5.3} \end{cases} \tag{8.3}$$

An additional feature that can contribute to drag reduction could be a passive/active change of the body geometry in function of the airspeed V_∞ (due to feathers moving under dynamic pressure). This feature would affect Re_{crit} that would change according to the body morphology.

The mechanism behind this variation is explained in Maybury's article as follow:

"The drawing out of feathers due to the dynamic pressure, and the fluttering pattern observed, could enable aeroelastic damping in the boundary layer; this damping increases as feather height increases with speed, and could therefore reduce drag as a passive mechanism of boundary layer regulation."

Finally, also the fineness ratio FR seems to affect C_{D_b}; a larger FR means a slender bird body thus a smaller drag coefficient (Re_{crit} displaced to lower Reynolds number; see Figure 8.4).

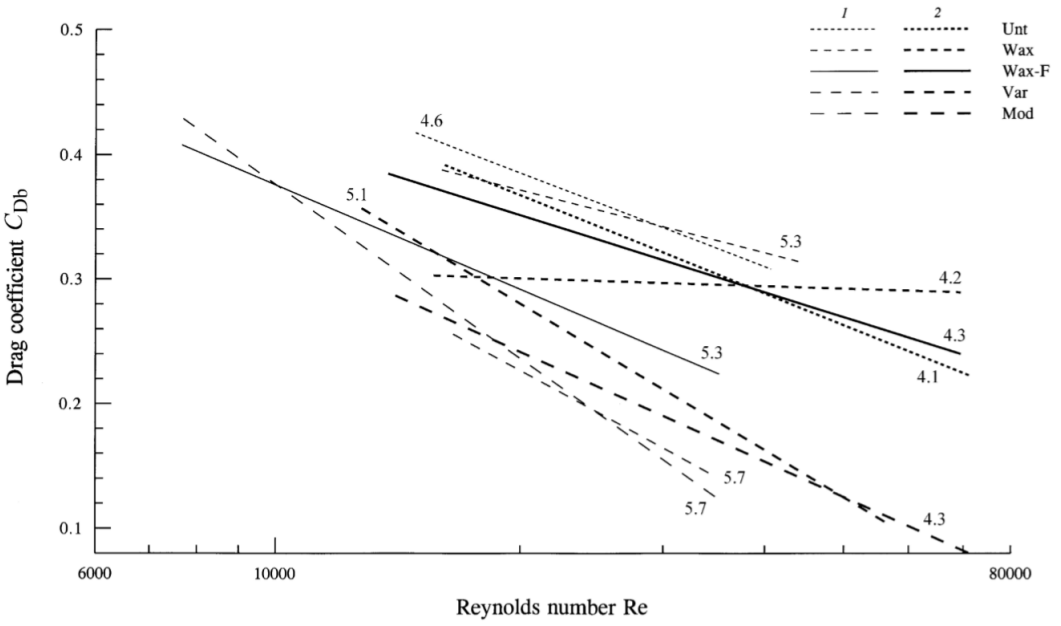

Figure 8.4: Drag coefficient with respect to Re for different trunk treatments and fineness ratios

In his thesis, Maybury conducts other type of analysis that are listed hereafter but they will not be discussed.

- Visualization of wake development over the body of a European Starling
- Body drag of a Perched Starling
- Investigating the Suitability of CFD to model bird body aerodynamics
- Wing interference effects on the drag and lift of starling bodies
- Avian respirometry mask aerodynamics
- Body drag reducing mechanisms of avian tails in steady flight
- Lift generation of avian tails

Even though, Maybury studied the avian tail in steady flight, a proper implication of the tail on power curves was not found in the literature. In my opinion, is still worth showing qualitatively, through Figure 8.5, how the avian tail contributes to drag reduction. Figure 8.5 groups the following images:

- (A) = reference bird (no tail changes)
- (B) = bird without rectrices feathers
- (C) = bird tailless

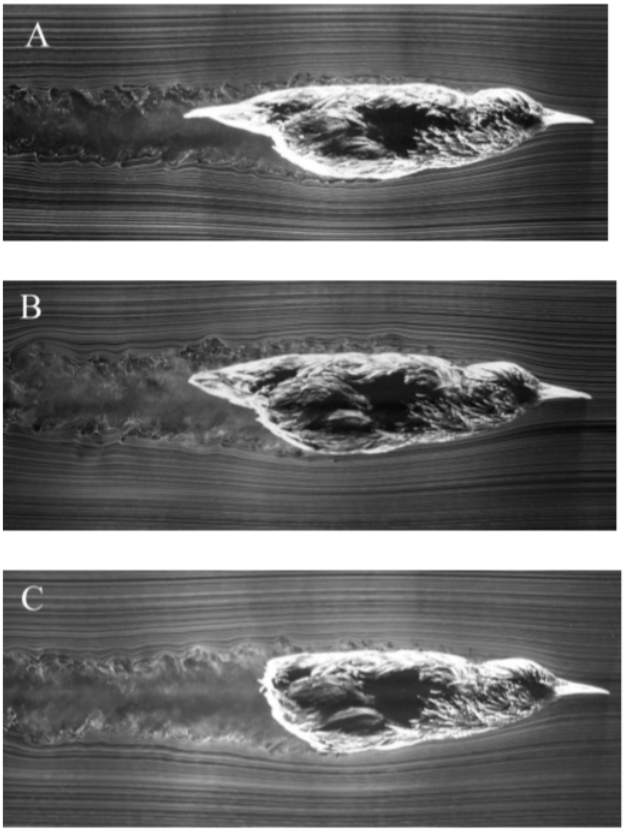

Figure 8.5: Flow visualization around a starling trunk for different tail treatments

In the last chapter of his thesis, Maybury reproduces the experiment done on the European starling, for 11 other bird species.

The specimens are 18 in total, 6 trunks are untreated (Unt) and 12 are waxed and footless (Wax-F). The species studied are:

Bengalese finch (Wax-F)	Blackbird (Unt/Wax-F)	Blue tit (Wax-F)	Chiffchaff (Wax-F)
Goldcrest (Unt/Wax-F)	Great tit (Unt/Wax-F)	Long-tailed tit(Wax-F)	Magpie (Wax-F)
Pigeon (Unt/Wax-F)	Sparrowhawk (Unt/Wax-F)	Starling (Unt/Wax-F)	Zebra finch (Wax-F)

Table 16: Bird Species

For each bird, the drag coefficient C_{D_b} is estimated respect to the airspeed V_∞; throughout all this analysis the Reynolds Re ranges from 10^4 to 10^5. The obtained data is fitted and a model is suggested to describe the drag coefficients C_{D_b} of the 12 waxed footless species and of the 6 untreated species:

$$C_{D_{b12}} = 66.6 m^{-0.511} FR_t^{0.915} S_b^{1.063} Re^{-0.197} \tag{8.4}$$

$$C_{D_{b6}} = 4.81{\cdot}10^7 m^{-2.167} FR_t^{2.491} S_b^{4.446} Re^{-0.221} \tag{8.5}$$

In the formulas, FR_t is defined as the ratio of the length L_t (trunk length measured from the beak tip to the base of the tail) and R (the radius of a circle equal to S_b).

An allometric equations for the trunk fineness ratio FR_t[26] can be retrieved using the 12 species studied. This correlation is represented in Figure 8.6 and is written as [27]:

$$FR_t = 6.08 m^{0.1523} \tag{8.6}$$

[26]This value ranges from 2.8 (owls) and 7.8 (swan)

[27]This correlation is extracted from the fitted graph of Figure 8.6; it might subjected to some errors

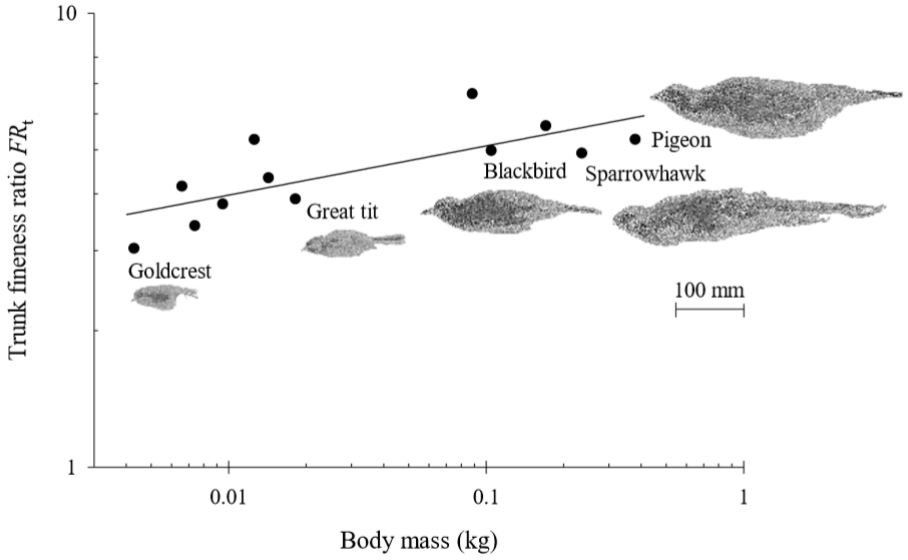

Figure 8.6: Fineness trunk ratio FR_t allometric relationship for 12 different birds

Equation 8.4 is more reliable than 8.5 because more flyers are employed for the fit.

8.2 Profile drag coefficient

The wings of a living bird can assume different positions in order to achieve perfect aerodynamic conditions. In flapping flight bird wings are supposed **(62)** to change their morphology over a flapping cycle for instance from downstroke to upstroke.
In addition, usually birds retract their wings during the upstroke phase to reduce drag.
Finally, some researchers suggest that bird might use this specific feature to fly; locally each wing segment is twisted to achieve a global uniform angle of attack along the wingspan.

This behaviour has still to be confirmed experimentally. Ideally, the profile drag coefficient $C_{D_{pro}}$ should be computed for each wing segment and wing pose.

All these variations are difficult to derive from an experimental analysis, thus must of researchers, have studied bird wings as fixed airfoils.

Of course, fixed wings will give just a rough estimate of the profile drag coefficient $C_{D_{pro}}$ of a bird. We remind that $C_{D_{pro}}$ is also called zero-lift drag coefficient C_{D_0} and it will be strictly related to the airfoil morphology.

The concept of zero-lift drag for an avian airfoil is misleading. In practice reciprocating wings during flight do not have such point. Therefore, this concept only makes sense when the wing is analysed as a fixed airfoil.

Phillip C. Withers **(84)** studied the lift and drag coefficient of 9 birds species and compared them to previous articles (Nachtigall & Kempf **(85)** and Redding **(86)**).

The species considered in this article and their respective profile drag coefficient $C_{D_{pro}}$ are listed here below:

Swift: 0.03	Petrel: 0.07	Woodcock: 0.082
Wood duck: 0.096	Quail: 0.055	Starling: 0.125
Nighthawk: 0.051	Hawk: 0.074	Vulture primary: 0.024

Table 17: Present study bird species: $C_{D_{pro}}$ **(84)**

Thrush: 0.05	Sparrow: 0.16
Duck: 0.11	Snipe: 0.11

Table 18: Previous study bird species: $C_{D_{pro}}$ **(85)**,**(86)**

Based on this experimental data, it is difficult to imagine an allometric correlation for the profile drag coefficient $C_{D_{pro}}$. Indeed, $C_{D_{pro}}$ strongly depends on the morphology of the bird wing, thus a generalisation for this coefficient is hard to extrapolate.

A possible correlation might be found by separating flyers in function of their flight style and wing morphology. In Figure 8.7 is possible to appreciate the wing shapes classification suggested by Paul Noll **(87)**.

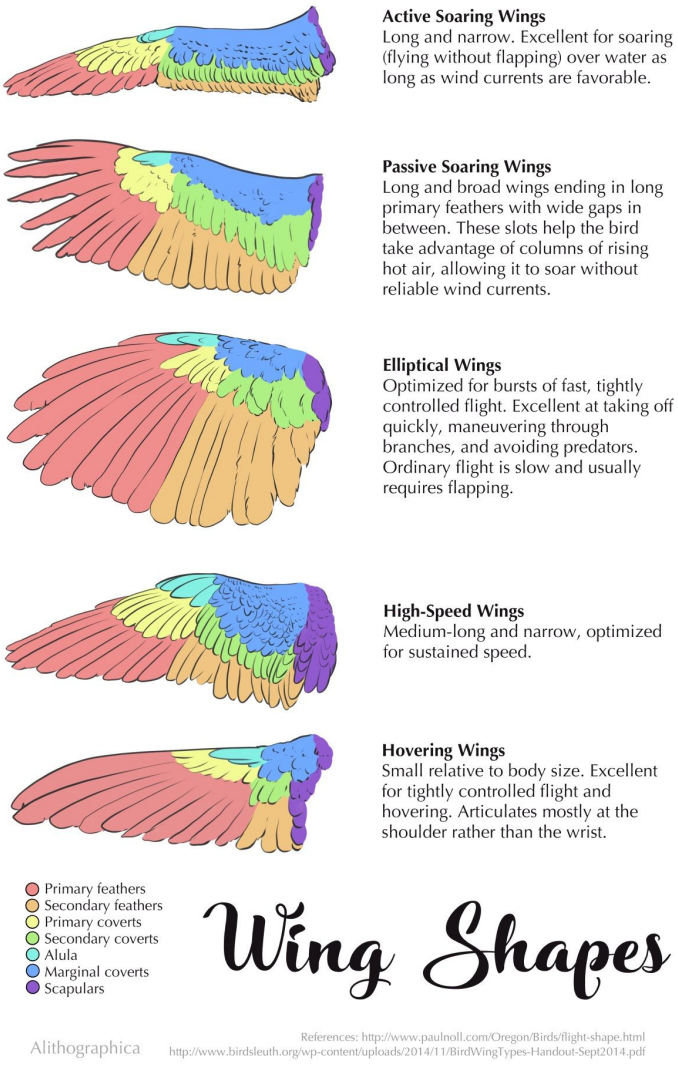

Figure 8.7: Type of flight style and wing morphology **(87)**

The article *"The influence of flight style on the aerodynamic properties of avian wings"***(88)** studies the avian wing with this philosophy.
This article is a result of a collaboration between the University of Manchester and the University of Liège. Authors, analyse the wing lift and drag coefficients of 10 different birds species.
The evaluation is conducted by separating the species in function of their flight style; the avian wings are still considered as fixed airfoil.

The species are separated in 3 categories[28]:

1. Forward and bounding flapping flight
2. High frequency flapping flight
3. Undulating flight

In Figure 8.8 the overall characteristics of each bird is represented; in red flight style **1**, in green flight style **2** and in purple flight style **3**.

[28]The flight style of the White Ibis cannot be associated to this flight styles. The White Ibis belongs to the category of long distance slow flapping flight birds.

Wing profile	Species	M_b (kg)	S (m^2)	b_{semi} (m)	AR	$C_{lift,\,max}$	$\tilde{x}$ ($C_{lift,\,max}$)	$C_{drag,\,min}$	$\tilde{x}$ ($C_{drag,\,min}$)	$\frac{C_{lift}{}^{3/2}}{C_{drag,\,max}}$	$\tilde{x}$ ($\frac{C_{lift}{}^{3/2}}{C_{drag,\,max}}$)
	Snipe	0.11	0.0021	0.19	6.88	0.77 ± 0.02		0.13 ± 0.002		3.45 ± 0.04	
	Plover	0.21	0.03	0.25	8.33	0.76 ± 0.03		0.12 ± 0.001		3.34 ± 0.2	
	Woodcock	0.31	0.048	0.27	6.08	0.97 ± 0.05	0.87 ± 0.04	0.13 ± 0.01	0.12 ± 0.005a	3.19 ± 0.08	3.47 ± 0.1a
	Woodpigeon	0.49	0.077	0.35	6.36	1.1 ± 0.1		0.09 ± 0.01		4.02 ± 0.2	
	Teal	0.31	0.026	0.2	6.15	0.79 ± 0.01		0.14 ± 0.002		2.76 ± 0.07	
	Wigeon	0.77	0.062	0.34	7.46	0.96 ± 0.04	0.84 ± 0.03	0.1 ± 0.02	0.11 ± 0.009b	0.11 ± 0.009	2.92 ± 0.18a,b
	Mallard	1.08	0.087	0.35	5.63	0.8 ± 0.02		0.08 ± 0.002		2.86 ± 0.67	
	Jay	0.17	0.045	0.22	4.35	0.7 ± 0.04		0.08 ± 0.003		3.05 ± 0.12	
	Magpie	0.21	0.05	0.25	4.97	0.69 ± 0.04	0.8 ± 0.068	0.08 ± 0.004	0.08 ± 0.004a,b	3.66 ± 0.07	3.5 ± 0.12b
	Jackdaw	0.25	0.055	0.29	6.07	1.09 ± 0.1		0.09 ± 0.01		4.01 ± 0.12	

Figure 8.8: Aerodynamic parameters of different flight style groups **(88)**

In this figure we can see that flyers of the third category have the lowest drag coefficient drag C_D.

Drag C_D and lift C_L coefficient are first estimated in function of the angle of attack α and then in term of the airflow speed U_∞. The fitted data for each bird is represented by the following equations:

$$C_x(\alpha, U_\infty = 0) = a_1 + b_1\alpha + c_1\alpha^2 + d_1\alpha^3$$
$$C_x(\alpha = cst, U_\infty) = b_2 U_\infty + a_2 \tag{8.7}$$

with x = (L or D), $\alpha = cst$ ranging from $-20°$ to $30°$ with steps of $10°$ and $a_1, b_1, c_1, d_1, b_2, a_2$ depending on the bird data regression. These equations are valid for $\alpha = [-20°, 30°]$ and $U_\infty = [8{-}16]$ m/s.

Extracting $C_{D_{pro}}$ from this data is not an easy task and would lead, eventually, to rough/incorrect estimations. Therefore, we did not follow this path in my thesis.

The final conclusions of the researchers are quite interesting though:

"The findings suggest that the differences in morphology associated with differing flight styles manifest only in differences in drag and not lift performance as $C_{drag,min}$ but not $C_{lift,max}$ differed between flight style groups. (...) Flapping flight involves complex conformational changes in the wing, in which pitch and span are continuously varying and the wing tip travels faster than the root. The different kinematic and aerodynamic demands of flapping and gliding mean that wings cannot be optimised for both. Wings may therefore be 'tuned' towards optimal performance in one flight style or the other."

It is worth mentioning, the novel approach proposed by the research team where, the lift C_L and drag C_D coefficients should be visualised as a three-dimensional curve obtained with the following formula:

$$C_x(\alpha, U_\infty) = C_{x_0} + C_{x_1}U_\infty + C_{x_2}\alpha + C_{x_3}\alpha U + C_{x_4}\alpha^2 + C_{x_5}\alpha^3 \tag{8.8}$$

This might be the best way to visualise the aerodynamic proprieties of an avian wing. Figure 8.9 depicts the 3-D curve fit of C_L for a jackdaw.

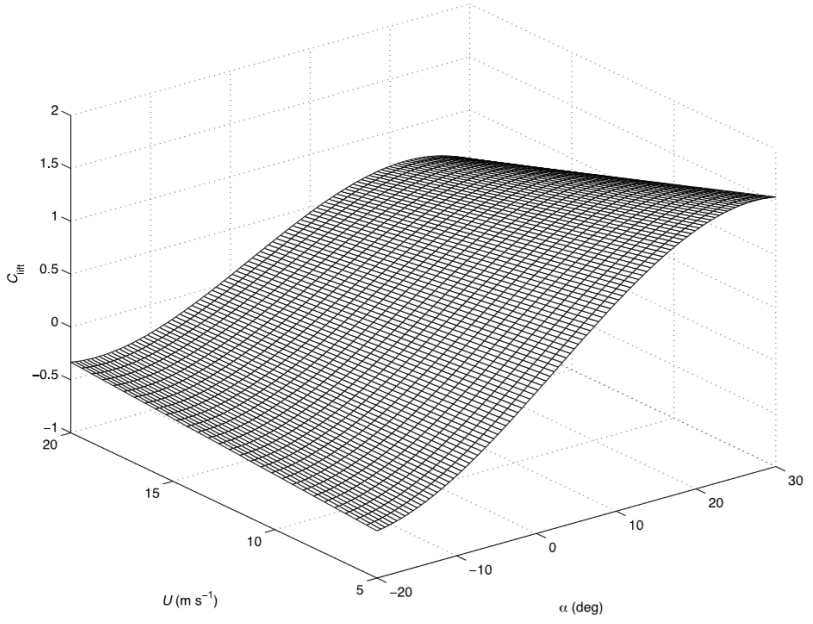

Figure 8.9: 3D curve fit: Jackdaw lift coefficient C_L

We conclude this section introducing the article *"Wake analysis of drag components in gliding flight of a jackdaw (Corvus monedula) during moult"* **(68)**.

Authors studied the aerodynamic consequences and the flight performance of a bird during moult. A living jackdaw was trained to glide in a wind tunnel; flights are recorded for 5 different stages of the moult.

Various kinematics and aerodynamics parameters are reported but for the sake of this discussion we will extract from the article only the features related to profile drag $C_{D_{pro}}$. For most avian airfoil,

$C_{D_{pro}}$ is a quadratic function of the lift coefficient:

$$C_{D_{pro}} = C_{D_{pro,min}} + k_p(C_L - C_{L_{D,pro,min}})^2 \tag{8.9}$$

The factors k_p, $C_{D_{pro,min}}$, $C_{L_{D,pro,min}}$ depend on the bird wing shape. The moult process will affect the wing shape and consequently those factors are modified.

The most interesting result of this article that could lead to an enhancement of power curve models is the pre-moult $C_{D_{pro}}$ airspeed dependency.

In fact, the behaviour of $C_{D_{pro}}$ is different compared to the previous articles. First the value of $C_{D_{pro}}$ is nearly 4 time lower than previous results, secondly the profile drag coefficient seems to follow a parabolic trend with a minimum roughly at the centre of the airspeed interval studied (approximately [6-12] m/s). It is surprising to see that the minimum of $C_{D_{pro}}$ is set around the minimum power speed V_{mp} of the bird ($\simeq$ 9.5 m/s **(33)**).

Figure 8.10 depicts the graph of $C_{D_{pro}}$ as extrapolated from article **(68)**.

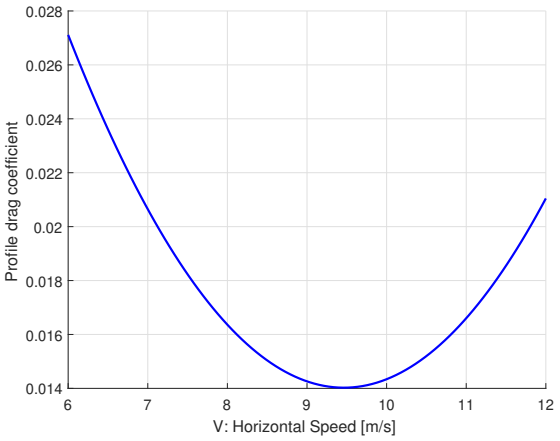

Figure 8.10: Profile drag coefficient of a jackdaw

This trend is not discussed by the authors and seems to be a known fact, unfortunately no other articles showing the same behaviour can be found in the literature.

An explanation for this trend could come from the span ratio (=wing retraction of the bird wing). In article **(68)** this parameter is analysed in function of the airspeed.

The span ratio can be defined as: $\sigma = \frac{b'}{b}$ where b' is the retracted wingspan. In Figure 8.11 is visible that σ reaches again a minimum near the minimal power speed V_{mp} of the bird and then slightly increases.

Of course, one can speculate that this trend could also be explained through the aerodynamical effects discussed in section 8.1.

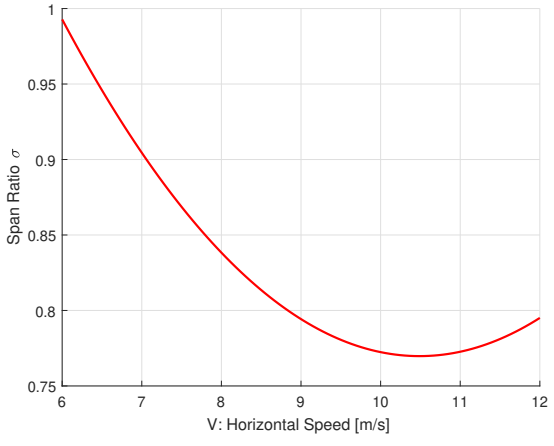

Figure 8.11: Wing retraction of a jackdaw

This discussion leaves us without a clear answer on how to quantify the profile drag coefficient $C_{D_{pro}}$.

8.3 Modified Actuator Disk

The actuator disk implemented by Pennycuick is independent from the bird flight kinematic.

In this section, 3 modified actuator disks will be presented and each of them will be expressed as functions of the flapping amplitude ϕ and of the stroke-plane angle γ.

The first model suggested by Ellington **(89)** is called partial actuator disk and is commonly used for insect flight study. The swept area S_d of Pennycuick's model is equivalent to the area of a circle of radius $\frac{b}{2}$. Implicitly this means that the flapping amplitude ϕ of the bird is equal to 90°. In normal flight condition, flapping amplitude never reach this order of magnitude. To emulate more accurately bird flight, Ellington proposes the following equation to describe the swept area S_d:

$$S_d = 2\phi\left(\frac{b}{2}\right)^2 \cos\left(\frac{\pi}{2} - \gamma\right) \tag{8.10}$$

This is the only divergence from the classical momentum jet theory, all the other calculations remain unchanged. Figure 8.12 clearly depicts the difference between the two models:

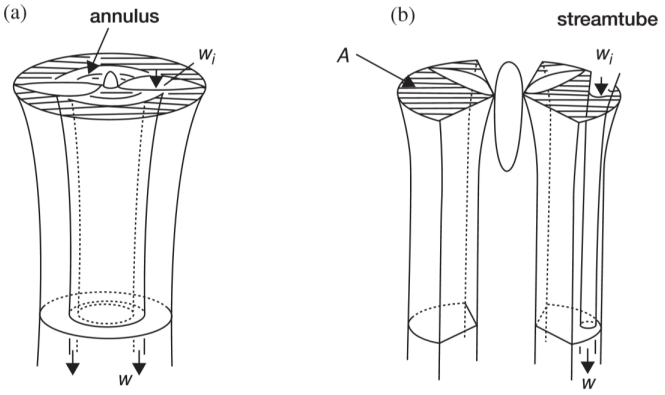

Figure 8.12: Actuator (a) and Partial actuator (b) disk **(63)**

The second actuator disk model is presented in the book *Principle of Helicopter Aerodynamics (chapter 2.14)* **(90)** but is already found in the work of Glauert (1928, 1935). B. Parlsew, in thesis **(61)**, extends Glauert's model.

An adaptation of Glauert's flow model is shown in Figure 8.13, here the swept area S_d is identical to to the definition of Pennycuick's model.

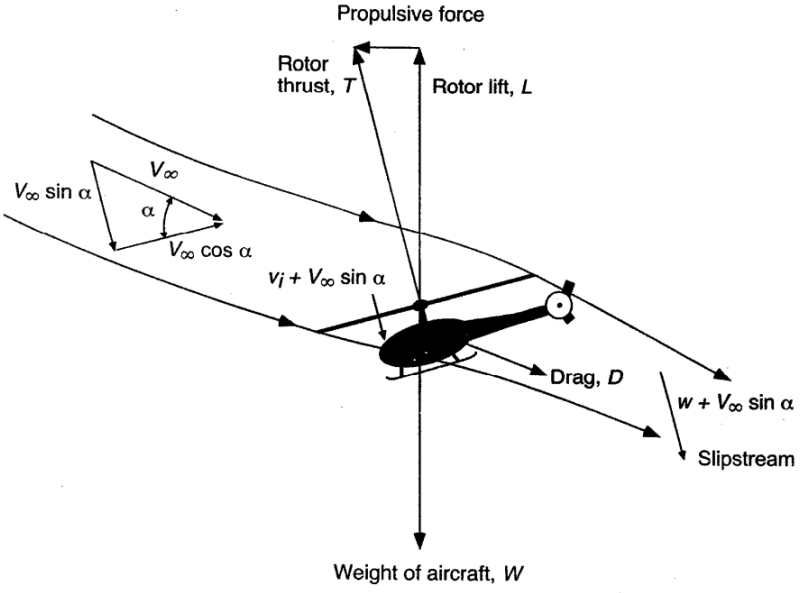

Figure 8.13: Helicopter forward flight stream tube **(90)**

Basing our calculations on the above figure, the resultant velocity U is given by:

$$U = \sqrt{(V_\infty \cos\alpha)^2 + (V_\infty \sin\alpha + v_i)^2} \tag{8.11}$$

where v_i is the induced velocity and α ($= \gamma$ stroke-plane angle) is the angle between the actuator disk and the free-stream flow.

The application of the conservation of momentum in the direction normal to the disk gives ($\dot{m} = \rho S_d U$):

$$T = \dot{m}(w + V_\infty \sin\alpha) - \dot{m} V_\infty \sin\alpha = \dot{m} w \tag{8.12}$$

After applying energy conservation law, we get:

$$P = T(v_i + V_\infty) = \frac{1}{2}\dot{m}(V_\infty \sin\alpha = \frac{1}{2}\dot{m}(V_\infty \sin\alpha + w)^2 - \frac{1}{2}\dot{m} V_\infty^2 \sin\alpha^2 = \frac{1}{2}\dot{m}(2 V_\infty w \sin\alpha + w^2) \tag{8.13}$$

When the conservation of momentum is introduced in the energy conservation, we obtain:

$$2 w v_i + 2 V_\infty w \sin\alpha = 2 V_\infty w \sin\alpha + w^2 \tag{8.14}$$

$$w = 2 v_i \tag{8.15}$$

The thrust T of the helicopter is then equal to:

$$T = 2 \rho S_d U v_i \tag{8.16}$$

In hovering flight condition ($V_\infty = 0$), thrust becomes:

$$T = 2 \rho S_d v_i^2 = 2 \rho S_d v_h^2 \tag{8.17}$$

By combining equations 8.16 and 8.17, we obtain the following implicit formula that is solved through an iterative computation; an initial value of v_i is chosen to start the computation.

$$v_i = \frac{v_h^2}{\sqrt{(V_\infty \cos\alpha)^2 + (V_\infty \sin\alpha + v_i)^2}} = \frac{T}{2 \rho S_d \sqrt{(V_\infty \cos\alpha)^2 + (V_\infty \sin\alpha + v_i)^2}} \tag{8.18}$$

The novel approach of B. Parslew is to evaluate the induced speed as a parallel v_{iz} and a perpendicular v_{ix} contribution with respect to the actuator disk. Figure 8.14 depicts this approach (ψ is equal to γ):

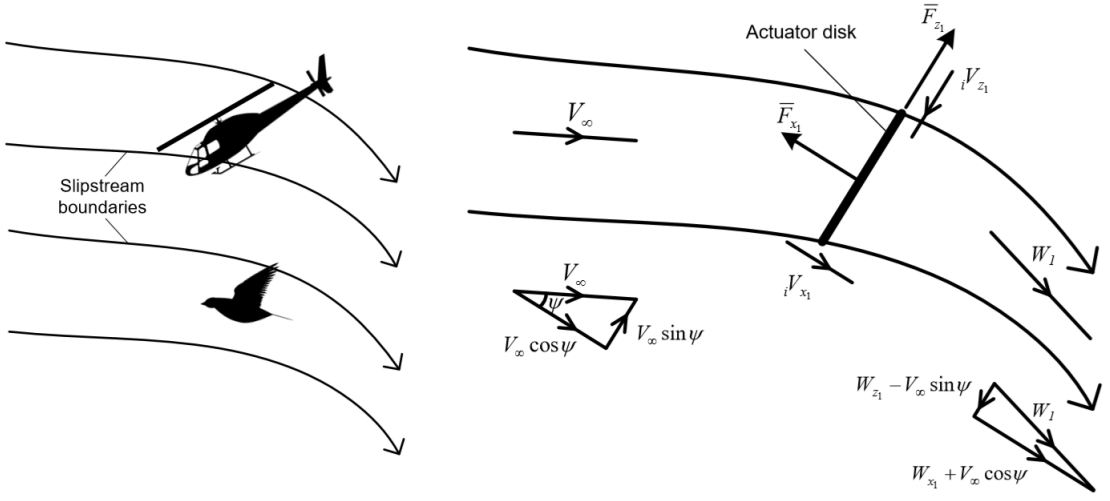

Figure 8.14: Parslew actuator disk approach **(61)**

The net velocity through the disk is given here by:

$$U = \sqrt{(V_\infty \cos\psi + v_{ix})^2 + (-V_\infty \sin\psi + v_{iz})^2} \tag{8.19}$$

After applying the conservation of both momentum and energy laws in the perpendicular and parallel direction, we obtain a conclusion similar to the previous analysis; for more information see chapter 4.2.7 of B. Parslew thesis **(61)**.

$$v_{ix} = \frac{\bar{F}_x}{2\rho S_d \sqrt{(V_\infty \cos\psi + v_{ix})^2 + (-V_\infty \sin\psi + v_{iz})^2}} \tag{8.20}$$

$$v_{iz} = \frac{\bar{F}_z}{2\rho S_d \sqrt{(V_\infty \cos\psi + v_{ix})^2 + (-V_\infty \sin\psi + v_{iz})^2}} \tag{8.21}$$

Both equations are implicit and are solved using an iterative computation. $\bar{F}_x$ and $\bar{F}_z$ are respectively the mean thrust and the mean lift generated by the bird over a flapping cycle. The power generated by the actuator disk here is given by the following equations:

$$P_x = \bar{F}_x(v_{ix} + V_\infty \cos\psi) \tag{8.22}$$

$$P_z = \bar{F}_z(v_{iz} - V_\infty \sin\psi) \tag{8.23}$$

$$P_{tot} = P_x + P_z \tag{8.24}$$

P_z is the induced power and P_x is the sum of profile and parasitic power.

Therefore, both contributions are calculated through the actuator disk. Indeed, this model is superior to the one of Pennycuick.

The third modified actuator disk, present in the thesis of H. G. Hernández **(91)**, applies momentum theory on a single wing. The swept area in this model is similar to the one described by Ellington **(89)**:

$$S_d = \phi\left(\frac{b}{2}\right)^2 \tag{8.25}$$

The stroke-plane angle γ is already present in the model thus it does not appear in Equation 8.25. Figure 8.15 schematize the swept area S_d and the consequent stream tube generated (**Attention!** In this figure b is the semi-wingspan).

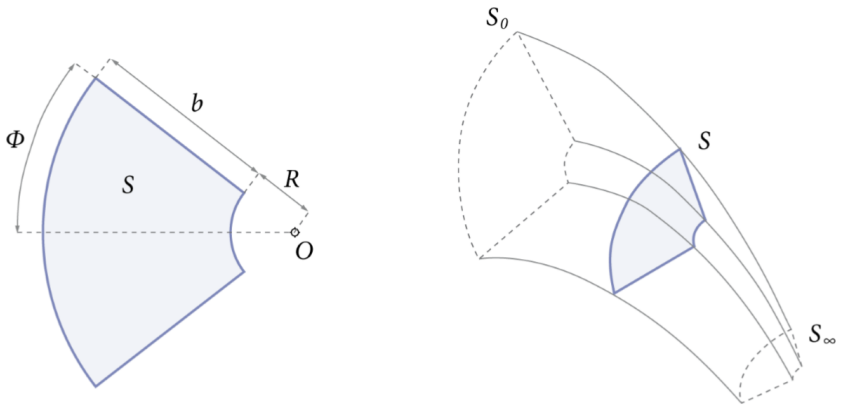

Figure 8.15: Swept area and stream tube associated **(91)**

In his work, Hernández computes the aerodynamic forces (lift and drag) generated by an insect using a simpler model[29] than a computational fluid dynamic model (i.e. CFD).
He then compares the results obtained with this model to the one calculated by his university using CFD model. His actuator disk construct will be briefly explained using images of his thesis as support.

In Figure 8.15, R defines a part of the wing that is aerodynamically inactive. Some insects have a small connecting segment of length R between the body and the wing that does not contributes to the flapping cycle. In birds this is absent.

Before, starting any calculation let us consider the most general case possible for this problem:

[29] Blade element method + modified actuator disk

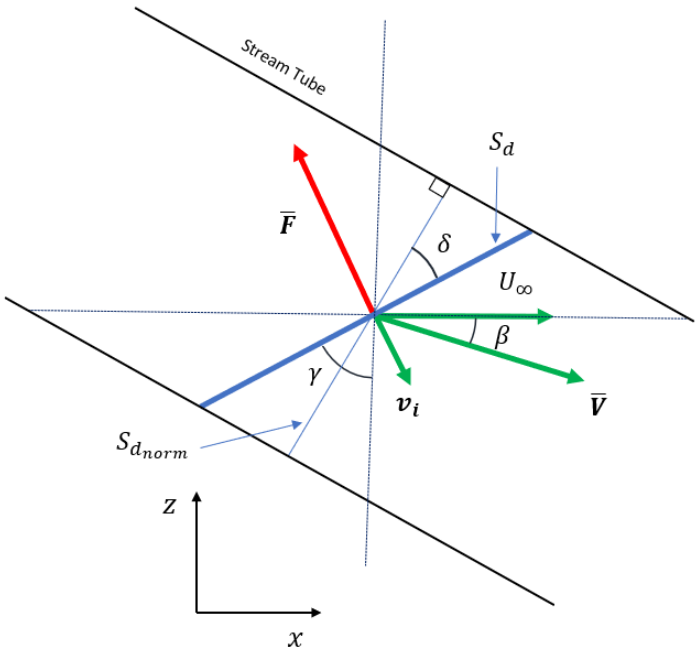

Figure 8.16: Image Reproduction: Modified actuator disk **(91)**

An horizontal velocity $\boldsymbol{V_\infty} = V_\infty \boldsymbol{e_x}$ passes through the actuator disk. The disk orientation respect to the vertical axis is γ (i.e. stroke plane angle).

A mean force $\bar{\boldsymbol{F}} = \bar{F}_x \boldsymbol{e_x} + \bar{F}_z \boldsymbol{e_z}$ and a mean induced speed $\bar{\boldsymbol{v}}_i = \bar{u}_x \boldsymbol{e_x} + \bar{w}_z \boldsymbol{e_z}$ are generated by the actuator disk.

The mean force $\bar{\boldsymbol{F}}$ can have a random direction but that has to be parallel and opposite to the mean induced speed $\bar{\boldsymbol{v}}_{\boldsymbol{i}}$.

The total mean velocity vector passing through the actuator disk is given by $\bar{\boldsymbol{V}} = (U_\infty + \bar{u}_x)\boldsymbol{e_x} + \bar{w}_z \boldsymbol{e_z}$ and forms an angle β.
In order to apply the equations of conservation (mass, momentum, energy) we need to work on an actuator disk perpendicular to the stream tube. For this reason, we will use S'_d the projection of S_d normal to the tube:

$$S'_d = S_d \cos\delta \tag{8.26}$$

Omitting all the calculations[30] and imposing the equations of conservation on a section of the stream tube, we obtain the following result describing the mean force produced by the actuator disk (for additional information see *Chapter 3.2* of Hernández thesis **(91)**):

$$\bar{\boldsymbol{F}} = 2\rho S'_d \bar{\boldsymbol{v}}_{\boldsymbol{i}} |\boldsymbol{U_\infty} + \bar{\boldsymbol{v}}_{\boldsymbol{i}}| \tag{8.27}$$

To conclude the model, $\cos\delta$, can be derived from Figure 8.16:

$$\cos\delta = \sin\gamma \cos\beta + \cos\gamma \sin\beta \tag{8.28}$$

The expressions of $\sin\gamma$ and $\cos\gamma$ are given by:

$$\sin\gamma = \frac{U_\infty + \bar{u}_i}{|\bar{\boldsymbol{U}}_{\boldsymbol{\infty}} + \bar{\boldsymbol{v}}_{\boldsymbol{i}}|} \tag{8.29}$$

$$\cos\gamma = \frac{\bar{w}_i}{|\bar{\boldsymbol{U}}_{\boldsymbol{\infty}} + \bar{\boldsymbol{v}}_{\boldsymbol{i}}|} \tag{8.30}$$

[30] Similar to the one done for the other actuator disks

Placing Equation 8.28 in Equation 8.27 and separating the resulting equation in the $\boldsymbol{x}$ and $\boldsymbol{z}$ coordinates, we obtain the following system of equations:

$$\begin{cases} \bar{F}_x = 2\rho S_d \bar{u}_i[\cos\gamma(U_\infty+\bar{u}_i)+\sin\gamma(\bar{w}_i)] \\ \bar{F}_z = 2\rho S_d \bar{w}_i[\cos\gamma(U_\infty+\bar{u}_i)+\sin\gamma(\bar{w}_i)] \end{cases}$$

This expression is valid in the first quadrant; by changing the sign of $\bar{F}_x$ and $\bar{F}_z$ is possible to use these equations for every quadrant.

To conclude, the power P generated by this modified actuator disk is given by:

$$P = \bar{\boldsymbol{F}}\cdot\bar{\boldsymbol{V}} = \bar{F}_x(U_\infty+\bar{u}_i)+\bar{F}_z\bar{w}_i$$

8.4 Flapping Flight Model

This section describes the flapping model that was supposed to support a part of the results of this thesis.

Unfortunately, the model neither returned correct results in term of flight kinematic nor in term of aerodynamic power.

Thus, it was discarded from the body of the thesis and inserted in this appendix section. I left the description of this flapping model in the hope that the future readers can solve its problematic.

My flapping model takes inspiration from the avian blade element model of B. Parslew **(32)**,**(36)**,**(61)**, and from other insect blade element model **(92)**,**(93)**,**(94)**,**(94)**,**(95)**,**(96)**.

Blade element methods are often used to estimate the forces generated by rotating elements such as helicopter blades. The blades are divided in infinitesimal segments. At each segment it is assigned a proper lift coefficient c_l and drag coefficient c_d. The forces are computed locally on each of these segments and then add up to obtain the overall lift L and drag D generated by the rotating blade.

Similarly, the wing of a bird can be considered as a rotating element. In the model the body of the bird is ignored. The wing reference frame is centered around the shoulder joint of the bird as shown in Figure 8.17.

Three type rotations are possible around this joint:

- **x**-axis: Plunging (Φ)
- **y**-axis: Pitching (Θ)
- **z**-axis: Sweeping (Ψ)

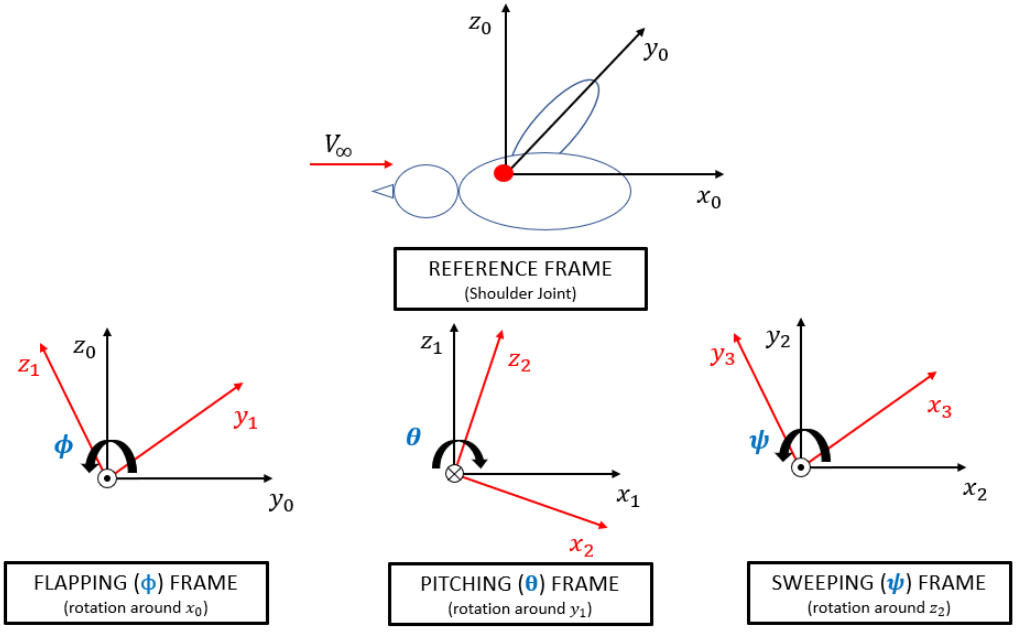

Figure 8.17: Reference frame

A single joint and single wing element are considered in the model. I decided to start the flapping cycle at the begging of downstroke, therefore the flight kinematic is written as follow:

$$\Phi(t) = \phi \cos(\omega t) \tag{8.31}$$

$$\Theta(t) = \theta_0 + \theta_1 \cos\left(\omega t + \frac{\pi}{2}\right) \tag{8.32}$$

$$\Psi(t) = -\psi_0 + \psi_1 \cos\left(\omega t - \frac{\pi}{2}\right) \tag{8.33}$$

These equations are based on all the considerations made throughout this thesis.

I suppose symmetry in forces generation, consequently only one wing is needed to evaluate the bird aerodynamic forces.

The wing is divided in the wingspan direction (**y**-axis) in n segments (from the shoulder joint 0 to the wingtip $\frac{b}{2}$) and the motion is decomposed temporally in m steps (from 0 to $T = \frac{1}{f}$).

In this discussion, the letters i and j identify respectively the temporal step and the spatial segment. Each spatial segment has a length $dy = \frac{b}{n}$ and each temporal step last $dt = \frac{T}{m}$.

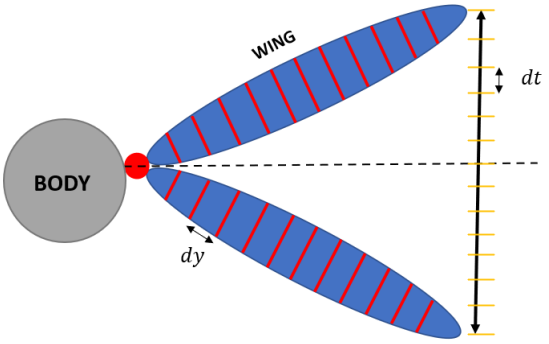

Figure 8.18: Spatial and Temporal discretization

The wing chord c selected for this flapping model is the one suggested by H. Oehme & Kitzler**(44)**. The wing retracts following the formula of M. KleinHeerenbrink et al.**(33)**. Both the chord and the wing retraction[31] b_{rt} are connected as follow:

$$b_{min} = b \cos \epsilon \tag{8.34}$$

$$b_{rt}(t) = \begin{cases} b & \text{for } t \leq T/2 \\ b_{min} + \frac{b - b_{min}}{2}\left[1 + \cos\left(\frac{4\pi(T-t)}{T}\right)\right] & \text{for } T/2 \leq t \leq T \end{cases} \tag{8.35}$$

$$c_0 = \frac{S}{b_{rt}(t)} \tag{8.36}$$

$$c(y,t) = \begin{cases} c_0 & \text{for } y \leq b_{rt}/4 \\ 4c_0\left(\frac{y(t)}{b_{rt}(t)}\right)\left(1 - \frac{y(t)}{b_{rt}(t)}\right) & \text{for } b_{rt}/4 \leq y \leq b_{rt}/2 \end{cases} \tag{8.37}$$

with ϵ as the retraction angle and $y(t)$ as the distance of a wing segment from the shoulder joint (see Figure 8.19).

[31] The spatial segments depend now on the temporal steps: $dy(t) = \frac{b_{rt}(t)}{n}$

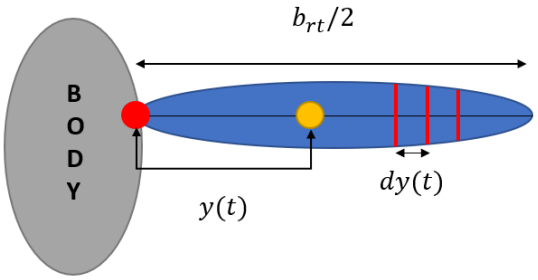

Figure 8.19: Spatial discretization with retraction

The blade element of this flapping model is enhanced and corrected by the modified actuator disk model of Hernández **(91)**. The actuator disk, presented in the previous section, considers only one wing and takes as inputs:

- Swept area: $S_d = \phi\frac{b^2}{4}$
- Stroke-plane angle: $\gamma = \theta_0$ (articulated lifting line analogy)
- Bird flight speed: V_∞
- Mean aerodynamic forces over a cycle for one wing: $\frac{D}{2} = \bar{F}_x$ and $\frac{L}{2} = \bar{F}_z$

The actuator disk is connected to the blade element by an iterative scheme. Initially, the mean aerodynamic force $\bar{F}_{x_{in}}$ and $\bar{F}_{z_{in}}$ are chosen as random value and are inserted into the actuator disk.

The actuator disk model, associated to the local frame **x2-y2-z2**, returns the horizontal v_{i_x} and vertical v_{i_z} induced velocities generated by the disk.

Afterward, these two induced velocities are introduced in the blade element that computes the new mean aerodynamic forces $\bar{F}_x$ and $\bar{F}_z$.

Finally these new mean aerodynamic forces are inserted in the actuator disk and the iterative scheme starts anew.

This iterative scheme stops when:

$$stop = max(|\bar{F}_x^p - \bar{F}_x^{p-1}|, |\bar{F}_z^p - \bar{F}_z^{p-1}|) \leq 0.01 \tag{8.38}$$

with p as the new iteration and $p-1$ as the previous iteration.

The overall iterative scheme is represented in the Figure 8.20:

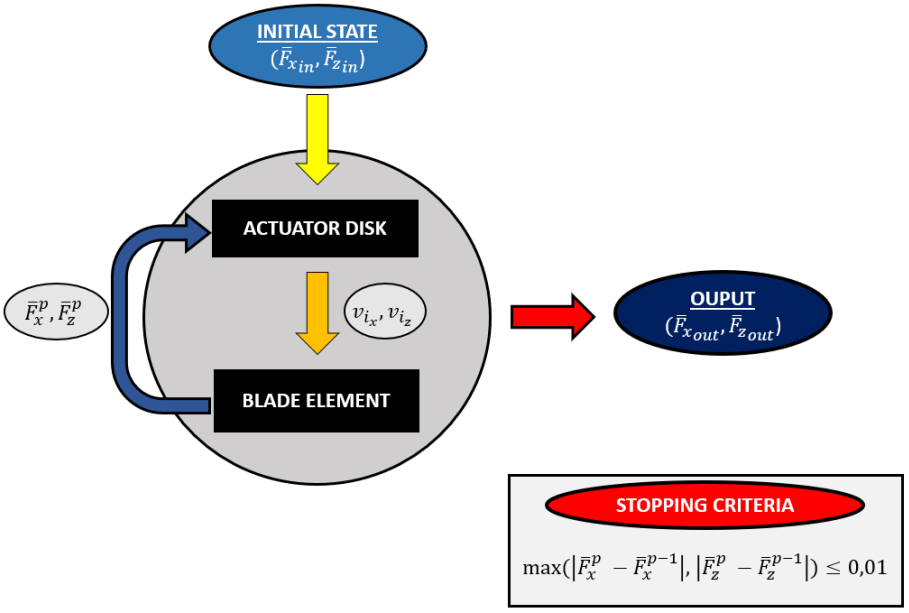

Figure 8.20: Model Iterative Scheme

We need now to define the blade element. We start by evaluating the position each wing segment. The position of a segment in the reference frame is written as:

$$\vec{r}_0^{\,i,j} = \begin{bmatrix} 0 \\ y^{i,j} \\ 0 \end{bmatrix} \tag{8.39}$$

Using the rotation matrix associated with each kinematic motion, we can compute the position of the wing segment in the local frame **x3-y3-z3**:

$$\vec{r}_3^{\,i,j} = \boldsymbol{R_3 R_2 R_1} \vec{r}_0^{\,i,j} = \boldsymbol{T_R} \begin{bmatrix} 0 \\ y^{i,j} \\ 0 \end{bmatrix} \tag{8.40}$$

with $\boldsymbol{R_1}$ as the plunging rotation matrix, $\boldsymbol{R_2}$ as the pitching rotation matrix, $\boldsymbol{R_3}$ as the sweeping rotation matrix and $\boldsymbol{T_R}$ as the frame transformation matrix.

Next, the speed perceived by a wing segment $\vec{V}_3^{\,i,j}$ should be computed. This speed is equal to the vector sum of the incoming flow V_∞ transposed in the local frame **x3-y3-z3**, the induced velocity $\vec{v}_{i_3}^{\,i,j}$ generated by the actuator disk and the kinematic velocity $\vec{v}_{kin_3}^{\,i,j}$ of the wing segment.

$$\vec{w}_3^{\,i,j} = \boldsymbol{R_3}^T \boldsymbol{R_2}^T \boldsymbol{R_1}^T \begin{bmatrix} \dot{\Phi}(t) \\ 0 \\ 0 \end{bmatrix} + \boldsymbol{R_3}^T \boldsymbol{R_2}^T \begin{bmatrix} 0 \\ \dot{\Theta}(t) \\ 0 \end{bmatrix} + \boldsymbol{R_3}^T \begin{bmatrix} 0 \\ 0 \\ \dot{\Psi}(t) \end{bmatrix} \tag{8.41}$$

$$\vec{V}_{\infty_3}^{\,i,j} = \boldsymbol{T_R} \begin{bmatrix} V_\infty \\ 0 \\ 0 \end{bmatrix} \tag{8.42}$$

$$\vec{v}_{i_3}^{\,i,j} = \boldsymbol{R_3} \begin{bmatrix} v_{i_x} \\ 0 \\ v_{i_z} \end{bmatrix} \tag{8.43}$$

$$\vec{v}_{kin_3}^{\,i,j} = \vec{w}_3^{\,i,j} \times \vec{r}_3^{\,i,j} \tag{8.44}$$

$$\vec{V}_3^{\,i,j} = \vec{V}_{\infty_3}^{\,i,j} + \vec{v}_{i_3}^{\,i,j} - \vec{v}_3^{\,i,j} \tag{8.45}$$

the minus sign in Equation 8.45 is related to the fact that the wing perceives a airflow opposite to its kinematic motion.

The blade element method assumes that each wing segment is a 2D airfoil (Figure 8.21).

B. Parslew **(61)** supposes that the lift c_l and drag c_d coefficients of each of these airfoils can be expressed as:

$$c_l = A \sin(2\alpha) \tag{8.46}$$

$$c_d = B - C \cos(2\alpha) \tag{8.47}$$

with α as the effective angle of attack seen by the airfoil and for our case $A = 1.8$, $B = 1.1$, $C = 1.07$.

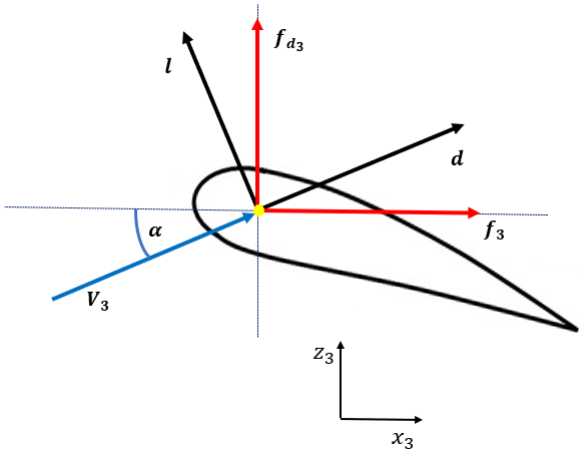

Figure 8.21: 2D airfoil

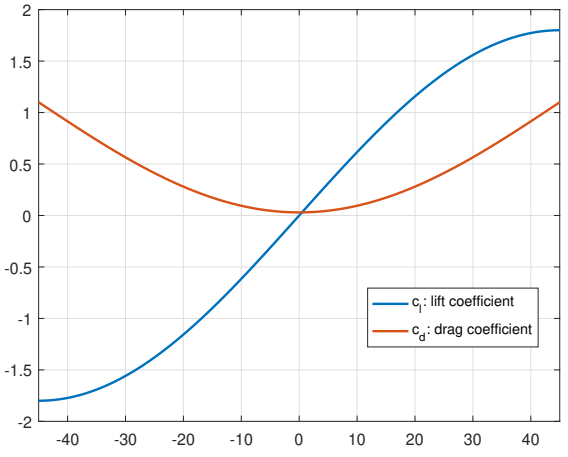

Figure 8.22: Lift and drag coefficients

With this information is now possible to compute the local forces f_{l_3} and f_{d_3} generated by a wing segment:

$$\alpha^{i,j} = \left(\frac{V_{z_3}^{i,j}}{V_{x_3}^{i,j}}\right) \tag{8.48}$$

$$l^{i,j} = \frac{1}{2}\rho c^{i,j}|\vec{V}_3^{\,i,j}|^2 c_l \tag{8.49}$$

$$d^{i,j} = \frac{1}{2}\rho c^{i,j}|\vec{V}_3^{\,i,j}|^2 c_d \tag{8.50}$$

$$f_{l_3}^{i,j} = d^{i,j}\sin(\alpha^{i,j}) + l^{i,j}\cos(\alpha^{i,j}) \tag{8.51}$$

$$f_{d_3}^{i,j} = d^{i,j}\cos(\alpha^{i,j}) - l^{i,j}\sin(\alpha^{i,j}) \tag{8.52}$$

From these equations we derive the mean aerodynamic forces, for one wing, over a flapping cycle in the reference frame coordinates:

$$\vec{f}_0^{\,i,j} = (\boldsymbol{T_R})^T \begin{bmatrix} f_{d_3}^{i,j} \\ 0 \\ f_{l_3}^{i,j} \end{bmatrix} \tag{8.53}$$

$$\bar{F}_x = \frac{1}{T}\sum_{i=1}^{m}\sum_{j=1}^{n} f_{x_0}^{i,j} = \frac{D}{2} \tag{8.54}$$

$$\bar{F}_y = \frac{1}{T}\sum_{i=1}^{m}\sum_{j=1}^{n} f_{y_0}^{i,j} \tag{8.55}$$

$$\bar{F}_z = \frac{1}{T}\sum_{i=1}^{m}\sum_{j=1}^{n} f_{z_0}^{i,j} = \frac{L}{2} \tag{8.56}$$

To finalise the blade element model, we retrieve the bird aerodynamic power P_{aero} using the following formula:

$$P_{aero} = \vec{\tau}\bullet\vec{w} \tag{8.57}$$

The torque $\vec{\tau}$ is calculated, in the local frame **x3-y3-z3**, through the following equation:

$$\vec{\tau}_3^{\,i,j} = \sum_{i=1}^{m}\sum_{j=1}^{n} \vec{r}_3^{\,i,j} \times \begin{bmatrix} f_{d_3}^{i,j} \\ 0 \\ f_{l_3}^{i,j} \end{bmatrix} \tag{8.58}$$

Therefore, the aerodynamic power is then the equal to:

$$P_{aero} = \vec{\tau}_3^{\,i,j}\bullet\vec{w}_3^{\,i,j} \tag{8.59}$$

The description of my flapping model ends here. Similarly to the ALL model, this model can be coupled with the PSO framework presented in chapter 4.

The flight kinematic parameters which may be studied in this context are displayed in Table 19:

$$\lambda_{kin} = [\phi, \theta_0, \theta_1, \psi_0, \psi_1, f, \epsilon] \tag{8.60}$$

Flapping Model/PSO	
Kinematic Parameter	Range
Flapping amplitude[32]: ϕ	$[1, 90°]$
Pitching offset: $\theta_0 = \gamma$	$[0, 90°]$
Pitching amplitude: θ_1	$[0, 90°]$
Sweeping offset: ψ_0	$[0, 90°]$
Sweeping amplitude: ψ_1	$[0, 90°]$
Flapping frequency: f	$[f_{ref}, 2f_{ref}]$
Wing retraction: ϵ	$[0, 90°]$

Table 19: Optimization Variables

This flapping model may be enhanced by inserting modifications such as wing folding σ or asymmetrical[33] flapping cycles (see chapter 3).

Bibliography

[1] Leonardo Da Vinci. *I Manoscritti di Leonardo Da Vinci: Codice Sul Volo Degli Uccelli e Varie Altre Materie*, (Italian), Internet Archive, 1893.

[2] Charles H. Gibbs-Smith. *Sir George Cayley Aeronautics*, Her Majesty's stationery Office, Museum of Science, London, 1795-1855.

[3] Arthur George Renstrom. *Wilbur & Orville Wright*, U.S. Centennial of Flight Commission and the National Aeronautics and Space Administration, September 2003.

[4] UCLouvain. Reveal Flight, *https://sites.uclouvain.be/RevealFlight/frontpage*, Research Project of MEED (EPL).

[5] U.S. Department of Transportation Federal aviation administration. *Pilot's Handbook of Aeronautical Knowledge*, Chapter 11, 2016.

[6] Anders Hedenström and Thomas Alerstam. *Optimal flight speed of birds*, The Royal Society, 29 June 1995.

[7] Professor Z. S. Spakovszky, Thermodynamics Lecture Notes, MIT, Chapter 13.2, Fall 2008.

[8] Andrew A. Biewener and Sheila N. Patek. *Animal Locomotion*, Oxford University Press, pp. 126-136, 2018.

[9] David V. Lee and Sarah L. Harris. *Linking Gait Dynamics to Mechanical Cost of Legged Locomotion*, Front. Robot. AI, 17 October 2018

[10] George H. Z. Liu, Michael Z. Q., Chen Yonghua Chen. *When joggers meet robots: the past, present, and future of research on humanoid robots*, Zhejiang University Press, 11 April 2019.

[11] G.R. Spedding, J.M.V. Rayner, & C. J. Pennycuick. *Momentum and energy in the wake of a pigeon (Columba livia) in slow flight.* Journal of Experimental Biology, 1984.

[12] G.R. Spedding. *The wake of a kestrel (Falco tinnunculus) in flapping flight*, Journal of Experimental Biology, 1987.

[13] Bret W. Tobalske and Kenneth P. Dial. *Flight kinematics of black-billed magpies and pigeons over a wide range of speeds*, The Journal of Experimental biology, The Company of Biologists Limited, 11 October 1995.

[14] Tyson L. Hedrick, Bret W. Tobalske and Andrew A. Biewener. *Estimates of circulation and gait change based on a three-dimensional kinematic analysis of flight in cockatiels (Nymphicus hollandicus) and ringed turtle-doves (Streptopelia risoria)*, The Journal of Experimental biology, The Company of Biologists Limited, 4 March 2002.

[15] G. R. Spedding, M. Rosén and A. Hedenström. *A family of vortex wakes generated by a thrush nightingale in free flight in a wind tunnel over its entire natural range of flight speeds*, The Journal of Experimental biology, The Company of Biologists Limited, 2 April 2003.

[16] A. Hedenström. *Vortex wakes of bird flight: old theory, new data and future prospects*, WIT Press, 2006.

[17] John L. Gittleman. *https://www.britannica.com/science/allometry*, Encyclopaedia Britannica, 2011.

[18] Crawford H. Greenewalt. *The Flight of Birds*, The American Philosophical Society, Philadelphia, July 1975.

[32] Lower bound must be higher than zero to avoid problem with the actuator disk model

[33] Inserting the downstroke ratio τ as a flight kinematic parameter

[19] Colin Pennycuick. *Modelling the Flying Bird*, Academic Press, 14th July 2008.

[20] Anders Hedenström, Geoffrey Spedding. *Colin James Pennycuick (1933–2019)*, Journal of Experimental Biology, 26 May 2020.

[21] William J. Maybury. *The aerodynamics of bird bodies*, University of Bristol, pp.(), January 2000.

[22] U.M. Lindhe Norber. *Flight and scaling of flyers in nature*, Department of Zoology,University of Göteborg, Sweden, WIT Press, 2006.

[23] Jeremy M. V. Rayner, *Form and function in avian flight*, Plenum Press, New York 1988.

[24] Thomas Alerstam, Mikazl Rosén, Johan Bäckman, Per G. P. Ericson, Olof Hellgren. *Flight Speeds among Bird Species: Allometric and Phylogenetic Effects*, Plos Biology, August 2007

[25] C. P. Elligton. *Limitations on animal flight performace*, University of Cambridge, The Journal of Experimetal biology, The Company of Biologists, 1991.

[26] Charles M. Bishop. *Circulatory variables and the flight performance of birds*, The Journal of Experimetal biology, The Company of Biologists, 8 March 2005.

[27] Coen Van Den Berg and Jeremy M. V. Rayner, *The moment of inertia of bird wings and the inertial power requirement for flapping flight*, The Journal of Experimetal biology, The Company of Biologists, 4 May 1995.

[28] C. J. Pennycuick. *Power requirements for horizontal flight in the pigeon columba livia*, The Journal of Experimetal biology, 24 April 1968.

[29] B. Bruderer, D. Peter, F. Liechti. *Wing-beat characteristics of birds recorded with tracking radar and cine camera*, IBIS: The International Journal of Avian Science, British Ornithologists'Uninon, 2010.

[30] C. J. Pennycuick, Marcel Klaassen, Anders Kvist and Ake Lindström. *Wingbeat frequency and the body drag anomaly: wind-tunnel observation on a thrush nightngale (Luscinia Luscinia) and a teal (Anas Crecca)*, The Journal of Experimental biology, The Company of Biologists Limited, 2 September 1996.

[31] B. W. Tobalske, T. L. Hedrick, K. P. Dial & A. A. Biewener. *Comparative power curves in bird flight*, Nature PublishingGroup, 23 January 2003.

[32] B. Parslew, William J. Crowther. *Simulating avian wingbeat kinematics*, Elsevier, Journal of Biomechanics, 24 July 2010.

[33] M. KleinHeerenbrink, L.C. Johansson, and A. Hedenström. *Power of the wingbeat: modelling the effects of flapping wings in vertebrate flight*, The Royal Society Publishing, 10 March 2015.

[34] R. Padfield. *Learning to Fly Helicopters*, Second Edition 2nd Edition, McGraw Hill Professional, 2013

[35] Online. *Bird Fly Animation*, https://www.youtube.com/watch?v=ILOdSC8Wu5k.

[36] B. Parslew. *Predicting power-optimal kinematics of avian wings*, The Royal Society, 17 October 2014.

[37] Rankine WJM. *On the mechanical principles of the action of propellers*, Trans Inst Naval Archit, 1865.

[38] Froude RE. *On the part played in propulsion by differences of fluid pressure*, Trans Inst Naval Archit, 1889.

[39] R. B. Richards. *Principles of Helicopter Performance*, Defense Technical Information Center, 8 March 1968.

[40] C. J. Pennycucik. *Empirical estimates of body drag of large waterfowl and raptors*, The Journal of Experimental biology, The Company of Biologists Limited, 7 October 1987.

[41] J. M. V. Rayner. *A vortex theory of animal flight. Part 1. The vortex wake of a hovering animal*, J. Fluid Mech., Cambridge University Press, 18 May 1978.

[42] J. M. V. Rayner. *A vortex theory of animal flight. Part 2. The forward flight of birds*, J. Fluid Mech., Cambridge University Press, 18 May 1978.

[43] V. A. Tucker. *Bird metabolism during flight: evaluation of a theory*, The Journal of Experimental biology, 1973.

[44] H. Oehme & Kitzler. *Untersuchungen zur Flugbiophysik und Flugphysiologie der Vögel. II. Zur Geometrie des Vogelflugels*, Zool. Jb. Physiol, 1975. (German)

[45] Webcomicms.net, clipart 10097033 flying birds.

[46] J. M. V. Rayner. *Mathematical modelling of the avian flight power curve*, Royal Society of London, 18 December 2000.

[47] Gnosspelius OF. *Notes to J. D. Fullerton 'The 2ight of birds'*, Journal of the Royal Aeronautical Society, 1925.

[48] Willmott AP & Ellington CP. *The mechanics of flight in the hawkmoth Manduca sexta. II. Aerodynamic consequences of kinematic and morphological variation*, Journal of Experimental Biology, 1997.

[49] Tucker VA. *Bird metabolism during flight: evaluation of a theory*, Journal of Experimental Biology, 1973.

[50] Greenewalt CH. *The flight of birds*, Transactions of the American Philosophical Society 65, part 4, 1975.

[51] Phlips PJ, East RA, Pratt NH. *An unsteady lifting line theory of flapping wings with application to the forward flight of birds*, Journal of Fluid Mechanics, 1981.

[52] KC. Hall & SR. Hall. *Minimum induced power requirements for apping flight*, J. Fluid Mech, 1996.

[53] Rayner JMV. *A new approach to animal flight mechanics*, Journal of Experimental Biology, 1979.

[54] Bret W. Tobalske. *Biomechanics of bird flight*, The Journal of Experimental Biology, The Company of Biologists, 2007.

[55] H. Blasius. *Grenzschichten in Flüssigkeiten mit kleiner Reibung*, Z. Math. Phys, 1908. (German)

[56] A. Hedenström and M. Rosén. *Body frontal area in passerine birds*, J. Avian Biol, 2003.

[57] L. Christoffer Johansson, Masateru Maeda, Per Henningsson and Anders Hedenstöm. *Mechanical power curve measured in the wake of flycatchers indicates modulation of parasite power across flight speeds*, The royal society, 9 January 2018.

[58] AFPT Website: https://cran.r-project.org/web/packages/afpt/index.html

[59] AFPT Code Documentation: https://cran.r-project.org/web/packages/afpt/afpt.pdf

[60] M. KleinHeerenbrink and A. Hedenström. *Wake analysis of drag components in gliding flight of a jackdaw (Corvus monedula) during moult*, The Royal Society, 2016.

[61] B. Parslew. *Simulating avian wingbeats and wakes*, Faculty of Engineering and Physical Sciences, Manchester, 2012.

[62] J. Guerrero. Joel Thesis Chapter 2, *Aerodynamics of flapping flight*, Department of Environmental Engineering, University of Genoa.

[63] Wei Shyy, Hikaru Aono, Chang-Know Kang and Hao Liu. *An introduction to flapping wing aerodynamics*, Cambridge University Press, 2013, Section 3.1.

[64] Website, https://birdsinslowmotion.com/, *Greylag Goose Slow Motion Flying Over Camera shot with Phantom HD Gold*, 29 March 2013.

[65] Horst Räbiger. *Lift during wing upstroke*, Onrithopter.de, Version 10.1, 2015.

[66] D. Mardulyn, J. Corbisier and M. Garcia. *Robird - SmartBird: How do they fly?*, LMECA2335: Biorobotics, 2019.

[67] G. A. Folkertsma, W. Straatman, N. Nijenhuis, C. H. Venner and S. Stramigioli, *Robird: A Robotic Bird of Prey*, IEEE Robotics Automation Magazine, Sept. 2017.

[68] M. KleinHeerenbrink and A. Hedenström. *Wake analysis of drag components in gliding flight of a jackdaw (Corvus monedula) during moult*, The Royal Society, 2016.

[69] Prandtl L., *Tragflügeltheorie*, Göttinger Nachrichten, Mathematisch- Physikalische Klasse, Germany, 1918.

[70] Xiang, Yujiang & Arora, Jasbir & Abdel-Malek, Karim. *Physics-based modeling and simulation of human walking: A review of optimization-based and other approaches*, Structural and Multidisciplinary Optimization, 2010.

[71] J. Kennedy and R. Eberhart, *Particle swarm optimization*, Proceedings of ICNN'95 - International Conference on Neural Networks, Perth, WA, Australia, 1995.

[72] Le, Lu & Ly, Hai-Bang & Pham, Binh & Le, Vuong & Phm, Tun & Nguyen, Duy-Hung Tran, Xuan-Tuan Le, Tien-Thinh. *Hybrid Artificial Intelligence Approaches for Predicting Buckling Damage of Steel Columns Under Axial Compression*, Materials, 2019.

[73] Tehrani, Kayvan & Zhang, Yiwen & Shen, Ping & Kner, Peter. *Adaptive optics stochastic optical reconstruction microscopy (AO-STORM) by particle swarm optimization*, Biomedical Optics Express, 8. 2017.

[74] Online website: *https://pythonhosted.org/pyswarm/*, 2013-2014.

[75] Online website: *https://en.wikipedia.org/wiki/Rastriginfunctionciteref-1*, last update 9 December 2019.

[76] E. Novitskaya, C.J. Ruestes, M.M. Porter, V.A. Lubarda, M.A. Meyers and J. McKittrick. *Reinforcements in avian wing bones: Experiments, analysis, and modeling*, Journal of the Mechanical Behavior of Biomedical Materials, Elsevier, 1 April 2017.

[77] T. N. Sullivan, M. A. Meyers and E. Arzt. *Scaling of bird wings and feathers for efficient flight*, Science Advances, 16 January 2019.

[78] C. J. Pennycuick. *Mechanics of flight*, Avian Biology, Academic Press: New York, San Francisco, London, 1975.

[79] D. G. Homberger. *The mechanics of feather movements: implications for the evolution of birds and avian flight*, Acta ornithol. 34, 135-140, 1999.

[80] Online website: *http://lentinklab.stanford.edu/welcome/biological$_q$uestions*.

[81] Online website: *https://www.biology.lu.se/research/research-groups/animal-flight-lab/facilities/lund-wind-tunnel*.

[82] S. F. Hoerner. *Fluid-dynamic drag: practical information on aerodynamic and hydrodynamic resistance*, 2nd edition By Author: New Jersey, 1958.

[83] G. Lotha. Website page: *Reynolds number*, https://www.britannica.com/science/Reynolds-number, Encyclopaedia Britannica, 2019.

[84] P. C. Withers. *An aerodynamic analysis of bird wings as fixed airfoils*, J. exp. Biol., 5 March 1980.

[85] W. Nachtigall, & B. Kempf. *Vergleichende untersuchungen zur flugbiologischen Funktion des Daumenfittichs (Alula tpuria) bei Vogeln.* I. Der Daumenfittich als Hochauftriebserzeuger, Z. Vergl. Physiol, 1971. (German)

[86] E. Reddig. *Der Ausdrucksflug der Bekassine (Capella gallinago gallinago).* J. Ornithol, 1978. (German)

[87] Paul Noll Website: http://www.paulnoll.com/Oregon/Birds/flight-shape.html

[88] John J. Lees, Grigorios Dimitriadis and Robert L.Nudds. *The influence of flight style on the aerodynamic properties of avian wings as fixed lifting surfaces*, PeerJ, 2016.

[89] C. P. Ellington. *The aerodynamics of hovering insect. V. A vortex theory*, Philosophical Transactions of the Royal Society of London, 1984.

[90] J. G. Leishman. *Principles of Helicopter Aerodynamics*, Second Edition, Cambridge university press, 2006.

[91] H. G. Hernández. *Aerodynamic models for finite flapping wings at low reynolds numbers*, Universidad Carlos III de Madrid, Aerospace Engineering, July 2017.

[92] Gordon J. Berman and Z. Jane Wang. *Energy-minimizing kinematics in hovering insect flight* , J. Fluid Mech. Cambridge University Press, 2007.

[93] Simon M. Walker and Graham K. Taylor. *A semi-empirical model of the aerodynamics of manoeuvring insect flight*, BioRxiv, 27 January 2020.

[94] Camli Badrya, Ananth Sridharan and James D. Baeder. *Multi-Fidelity Coupled Trim Analysis of a Flapping-Wing Micro Air Vehicle Flight*, Journal of Aircraft, ARC, 31 January 2017.

[95] Mostafa R. A. Nabawy and William J. Crowther. *On the quasi-steady aerodynamics of normal hovering flight part II: model implementation and evaluation*, Interface, February 2014.

[96] Q. Wang, J. F. L. Goosen and F. van Keulen. *A predictive quasi-steady model of aerodynamic loads on flapping wings*, J. Fluid Mech. Cambridge University Press, 2016.

UNIVERSITÉ CATHOLIQUE DE LOUVAIN
École polytechnique de Louvain
Rue Archimède, 1 bte L6.11.01, 1348 Louvain-la-Neuve, Belgique | **www.uclouvain.be/epl**